


Doctoral Dissertation
Doctoral Program in Electrical, Electronics and Communications Engineering
(33rd cycle)

On Some Strategies for Stabilizing Electromagnetic Integral Equations in Different Frequency Ranges

Tiffany L. Chhim
* * * * * *

Supervisors
Prof. Francesco P. Andriulli
Prof. Adrien Merlini (Co-supervisor)

Doctoral Examination Committee:
Prof. Paolo Rocca, Università di Trento (Referee)
Prof. Andrea F. Morabito, Università degli Studi di Reggio Calabria (Referee)
Prof. Francesca Vipiana, Politecnico di Torino
Prof. Guido Lombardi, Politecnico di Torino
Prof. Simon B. Adrian, University of Rostock
Prof. Adrien Merlini, IMT Atlantique
Prof. Francesco P. Andriulli, Politecnico di Torino

Politecnico di Torino
July 19, 2021

Summary

In computational electromagnetics, phenomena such as wave propagation, radiation and scattering can be modeled through a variety of integral equations. Using the Boundary Element Method (BEM), these equations can then be solved numerically with computers. Unfortunately, integral equations are usually prone to instabilities under certain simulating conditions. For instance, one of the most employed formulation is the Electric Field Integral Equation (EFIE), which is adapted to model metallic objects as Perfect Electric Conductors (PEC). This formulation is however affected by breakdowns at low and high frequencies that result in detrimental consequences on the performance of the solver. More precisely, the condition number of the EFIE matrix obtained in those cases increases, which in turn impacts the accuracy of the solution and the convergence speed of iterative solvers.

This thesis provides an in-depth investigation of scenarios at low and high frequencies and presents stable and accurate original BEM integral equations. One of the research axes involves low frequency simulations of lossy conductors for the modeling of eddy currents. A strategy employing quasi-Helmholtz projectors is devised based on an asymptotic study of the Poggio-Miller-Chang-Harrington-Wu-Tsai (PMCHWT) equation. The second part focuses on high frequency problems for PECs. A theoretical analysis of the eigenvalues of integral operators in two dimensions is presented using Fourier modes. A novel Combined Field Integral Equation (CFIE) is then proposed for reliable and resonance-free simulations at high frequency for the case of the canonical infinite cylinder.

Acknowledgments

First and foremost, I would like to thank my PhD advisor, Prof. Francesco Andriulli, for guiding me during the entire process with his research expertise and extensive knowledge.

I would also like to express gratitude toward my dear colleagues for providing valued help and advice throughout these years and with whom I made a great many precious memories. To my wise seniors, Simon, Lyes, John Erick, Andrea, Adrien and Alexandre, my fellow comrades Clément and Maxime, as well as my enthusiastic juniors, Davide, Damiano and Alessandro.

I would like as well to offer my thanks to my cherished family and friends for their continuous support and encouragement. Lastly, I will thank my partner Maxime once more, who has been constantly standing by my side through both good and bad times.

Contents

List of Tables

List of Figures

Chapter 1

Introduction and Outline

Computational science is a rapidly expanding concept combining mathematical models and high computing performance to solve complex problems. In particular, computational electromagnetics is a sub category of computational physics based on Maxwell's equations to describe all types of wave propagation scenarios. Typical problems include scattering from arbitrarily shaped objects and antenna radiation. A variety of methods are available to model time-harmonic phenomena, each with their own strengths and weaknesses. For instance, the most frequently employed approaches are the Finite Element Method (FEM), the Finite Difference Method (FDM) and the Boundary Element Method (BEM). The latter strategy is used throughout this thesis as the model of choice to solve integral equations.

The thesis is divided into chapters covering the majority of the research carried out during the program. Starting with the foundations of electromagnetic theory, Chapter 2 introduces Maxwell's equations and the mathematical derivations leading to a set of widespread and classic integral formulations. Each of these equations is suited to particular scenarios and possesses its own limitations. The second half of the chapter presents the BEM which translates integral equations into numerical problems that are solvable by a computer.

Chapter 3 then delves into the concept of preconditioning, which constitutes the focus of the thesis and represents a significant aspect of computational electromagnetics. The role of the condition number of the matrices obtained with the BEM is illustrated through the example of the classic low frequency breakdown of the Electric Field Integral Equation (EFIE). Some techniques employed to improve the computational complexity are presented.

The simulation of eddy currents at low frequencies is explored in Chapter 4. This type of scenario is highly relevant as it appears in a variety of industrial applications. This low frequency configuration for conductive objects is more difficult to navigate and analyze compared to Perfect Electric Conductors (PEC) due to the complex material characteristics. A novel method is presented, based on an asymptotic study of the Poggio-Miller-Chang-Harrington-Wu-Tsai (PMCHWT) equation and

the application of quasi-Helmholtz projectors.

In Chapter 5, we investigate the case of PECs at high frequency. The chapter highlights particular behavior occurring in that frequency range using a spectral analysis in two dimensions. The standard electric and magnetic field operators are examined to identify the ill-conditioning observed at large frequencies. A new high frequency stable formulation is introduced by appropriately combining the characteristics of each operator.

Lastly, closing remarks summarizing the objectives achieved throughout the thesis are given in Chapter 6, alongside future prospects and open leads on the topics that have been treated.

Chapter 2

Background and Notation

This chapter lays the groundwork for the rest of the thesis by introducing the core concepts and notions of computational electromagnetics. The well-known Maxwell's equations governing the laws of electromagnetism are first introduced, followed by the derivation of several classic integral formulations commonly used to model and simulate a majority of practical scenarios. The Boundary Element Method (BEM) is presented next, as the key technique employed throughout this work, which adapts those equations into a format suitable for numerical computer simulation. The theoretical development is partly based on [54].

2.1 Maxwell's Equations

As the starting point for the study of electromagnetism, we introduce the following set of Maxwell's equations, which can be written under various forms. Here they are given under their differential form and in the frequency domain, at a position $\boldsymbol{r}$ in a continuous medium,

$$\nabla \times \boldsymbol{E}(\boldsymbol{r}) = -\mathrm{j}\omega\mu\boldsymbol{H}(\boldsymbol{r})\,, \tag{2.1}$$

$$\nabla \times \boldsymbol{H}(\boldsymbol{r}) = \mathrm{j}\omega\epsilon\boldsymbol{E}(\boldsymbol{r}) + \boldsymbol{j}(\boldsymbol{r})\,, \tag{2.2}$$

$$\nabla \cdot \boldsymbol{D}(\boldsymbol{r}) = \rho_e(\boldsymbol{r})\,, \tag{2.3}$$

$$\nabla \cdot \boldsymbol{B}(\boldsymbol{r}) = 0\,. \tag{2.4}$$

For the vectorial quantities, we denote as $\boldsymbol{E}$ the electric field, $\boldsymbol{H}$ the magnetic field, $\boldsymbol{D}$ the electric flux density, $\boldsymbol{B}$ the magnetic flux density, and $\boldsymbol{j}$ the electric current density. As for the scalar quantities, j is used for the imaginary number, μ and ϵ are the magnetic permeability and electric permittivity of the medium, ρ_e represents the electric charge density, and lastly, ω is the angular frequency. Here and in the rest of the thesis, we assume and omit the time dependence $\mathrm{e}^{\mathrm{j}\,\omega t}$ for time-harmonic fields, where t is the time.

The flux densities $\boldsymbol{D}$ and $\boldsymbol{B}$ are related to the fields $\boldsymbol{E}$ and $\boldsymbol{H}$ through the constitutive relations

$$\boldsymbol{D} = \epsilon \boldsymbol{E}\,, \tag{2.5}$$
$$\boldsymbol{B} = \mu \boldsymbol{H}\,. \tag{2.6}$$

For some materials, the permittivity and permeability can vary depending on the fields (linearity), position (homogeneity), direction (isotropy), or frequency (dispersion). However, throughout this work, we will consider non-varying media unless specified otherwise. The quantities ϵ and μ are defined with respect to the corresponding values for the vacuum, ϵ_0 and μ_0, as

$$\epsilon = \epsilon_r \epsilon_0\,, \tag{2.7}$$
$$\mu = \mu_r \mu_0\,, \tag{2.8}$$

where ϵ_r and μ_r are called relative permittivity and permeability. The values for the vacuum are

$$\epsilon_0 = 8.854 \times 10^{-12}\ \mathrm{F\,m^{-1}}\,, \tag{2.9}$$
$$\mu_0 = 4\pi \times 10^{-7}\ \mathrm{H\,m^{-1}}\,. \tag{2.10}$$

For the forthcoming integral equation derivation, Maxwell's equations are symmetrized by introducing the equivalent magnetic charge density ρ_m and a magnetic current density $\boldsymbol{m}$ to obtain

$$\nabla \times \boldsymbol{E}(\boldsymbol{r}) = -\mathrm{j}\omega\mu \boldsymbol{H}(\boldsymbol{r}) - \boldsymbol{m}(\boldsymbol{r})\,, \tag{2.11}$$
$$\nabla \times \boldsymbol{H}(\boldsymbol{r}) = \mathrm{j}\omega\epsilon \boldsymbol{E}(\boldsymbol{r}) + \boldsymbol{j}(\boldsymbol{r})\,, \tag{2.12}$$
$$\nabla \cdot \boldsymbol{D}(\boldsymbol{r}) = \rho_e(\boldsymbol{r})\,, \tag{2.13}$$
$$\nabla \cdot \boldsymbol{B}(\boldsymbol{r}) = \rho_m(\boldsymbol{r})\,. \tag{2.14}$$

This manipulation creates analogies between electric and magnetic quantities and allows simplifications throughout the reasoning.

2.2 Electric and Magnetic Fields in Free Space

2.2.1 Electromagnetic Potentials

Solutions to Maxwell's equations can be derived in a homogeneous and infinitely large space, called free space, by defining electromagnetic potentials. Using the linearity of the equations and the principle of superposition, we divide the electric and magnetic fields into sums of contributions from electric and magnetic sources,

$$\boldsymbol{E} = \boldsymbol{E}_e + \boldsymbol{E}_m\,, \tag{2.15}$$
$$\boldsymbol{H} = \boldsymbol{H}_e + \boldsymbol{H}_m\,, \tag{2.16}$$

where the indices e and m stand for the electric and magnetic sources, respectively. Each of the fields satisfies Maxwell's equations. Therefore, we have, for the fields created by the electric sources,

$$\nabla \times \boldsymbol{E}_e = -\mathrm{j}\omega\mu\boldsymbol{H}_e\,, \tag{2.17}$$
$$\nabla \times \boldsymbol{H}_e = \mathrm{j}\omega\epsilon\boldsymbol{E}_e + \boldsymbol{j}\,, \tag{2.18}$$
$$\nabla \cdot \boldsymbol{D}_e = \rho_e\,, \tag{2.19}$$
$$\nabla \cdot \boldsymbol{B}_e = 0\,, \tag{2.20}$$

and for those created by the magnetic sources,

$$\nabla \times \boldsymbol{E}_m = -\mathrm{j}\omega\mu\boldsymbol{H}_m - \boldsymbol{m}\,, \tag{2.21}$$
$$\nabla \times \boldsymbol{H}_m = \mathrm{j}\omega\epsilon\boldsymbol{E}_m\,, \tag{2.22}$$
$$\nabla \cdot \boldsymbol{D}_m = 0\,, \tag{2.23}$$
$$\nabla \cdot \boldsymbol{B}_m = \rho_m\,, \tag{2.24}$$

where we omitted the position vector $\boldsymbol{r}$ for clarity. We start by considering the case where there are no magnetic sources, i.e. when $\boldsymbol{m} = \boldsymbol{0}$ and $\rho_m = 0$. From eq. (2.20), the properties of the divergence operator and the constitutive relation $\boldsymbol{B}_e = \mu\boldsymbol{H}_e$, we introduce the vector potential $\boldsymbol{A}_e$ such that

$$\mu\boldsymbol{H}_e = \nabla \times \boldsymbol{A}_e\,. \tag{2.25}$$

Then, by replacing eq. (2.25) into eq. (2.17), we obtain

$$\nabla \times (\boldsymbol{E}_e + \mathrm{j}\omega\boldsymbol{A}_e) = \boldsymbol{0}\,. \tag{2.26}$$

Considering the property of the curl operator, this cancellation leads to the introduction of the scalar potential Φ_e

$$\boldsymbol{E}_e + \mathrm{j}\omega\boldsymbol{A}_e = -\nabla\Phi_e\,. \tag{2.27}$$

Now we substitute eqs. (2.25) and (2.27) into eq. (2.18), resulting in

$$\begin{aligned}\nabla \times \left(\frac{1}{\mu}\nabla \times \boldsymbol{A}_e\right) &= \mathrm{j}\omega\epsilon\left(-\nabla\Phi_e - \mathrm{j}\omega\boldsymbol{A}_e\right) + \boldsymbol{j}\,,\\ &= -\mathrm{j}\omega\epsilon\nabla\Phi_e + \omega^2\epsilon\boldsymbol{A}_e + \boldsymbol{j}\,.\end{aligned} \tag{2.28}$$

For any vector field $\boldsymbol{F}$, using the vectorial identity

$$\nabla \times \nabla \times \boldsymbol{F} = \nabla(\nabla \cdot \boldsymbol{F}) - \nabla^2\boldsymbol{F}\,, \tag{2.29}$$

we obtain

$$\nabla(\nabla \cdot \boldsymbol{A}_e) - \nabla^2\boldsymbol{A}_e = -\mathrm{j}\omega\epsilon\mu\nabla\Phi_e + k^2\boldsymbol{A}_e + \mu\boldsymbol{j}\,, \tag{2.30}$$

where the wave number k is defined as

$$k = \omega\sqrt{\epsilon\mu}\,. \tag{2.31}$$

Until now, only the curl of $\boldsymbol{A}_e$ has been determined. Since the choice of its divergence is arbitrary, we opt for the Lorenz gauge by defining

$$\nabla \cdot \boldsymbol{A}_e = -\mathrm{j}\omega\epsilon\mu\Phi_e\,, \tag{2.32}$$

which simplifies eq. (2.30) into a Helmholtz equation to be solved for $\boldsymbol{A}_e$,

$$\nabla^2\boldsymbol{A}_e + k^2\boldsymbol{A}_e = -\mu\boldsymbol{j}\,, \tag{2.33}$$

where ∇^2 represents the vector Laplacian operator. Summarizing, the fields generated by the electric sources are written with respect to $\boldsymbol{A}_e$ as

$$\boldsymbol{E}_e = \frac{1}{\mathrm{j}\omega\epsilon\mu}\nabla(\nabla\cdot\boldsymbol{A}_e) - \mathrm{j}\omega\boldsymbol{A}_e\,, \tag{2.34}$$

$$\boldsymbol{H}_e = \frac{1}{\mu}\nabla\times\boldsymbol{A}_e\,. \tag{2.35}$$

Proceeding similarly for the magnetic sources by considering $\boldsymbol{j} = \boldsymbol{0}$ and $\rho_e = 0$, we have the Helmholtz equation for the vector potential $\boldsymbol{A}_m$,

$$\nabla^2\boldsymbol{A}_m + k^2\boldsymbol{A}_m = -\epsilon\,\boldsymbol{m}\,, \tag{2.36}$$

and the fields generated by the magnetic sources,

$$\boldsymbol{E}_m = -\frac{1}{\epsilon}\nabla\times\boldsymbol{A}_m\,, \tag{2.37}$$

$$\boldsymbol{H}_m = \frac{1}{\mathrm{j}\omega\epsilon\mu}\nabla(\nabla\cdot\boldsymbol{A}_m) - \mathrm{j}\omega\boldsymbol{A}_m\,. \tag{2.38}$$

Lastly, substituting the different contributions into eqs. (2.15) and (2.16), the total electric and magnetic fields become

$$\boldsymbol{E} = \frac{1}{\mathrm{j}\omega\epsilon\mu}\nabla(\nabla\cdot\boldsymbol{A}_e) - \mathrm{j}\omega\boldsymbol{A}_e - \frac{1}{\epsilon}\nabla\times\boldsymbol{A}_m\,, \tag{2.39}$$

$$\boldsymbol{H} = \frac{1}{\mu}\nabla\times\boldsymbol{A}_e + \frac{1}{\mathrm{j}\omega\epsilon\mu}\nabla(\nabla\cdot\boldsymbol{A}_m) - \mathrm{j}\omega\boldsymbol{A}_m\,. \tag{2.40}$$

The remaining step is to find expressions for $\boldsymbol{A}_e$ and $\boldsymbol{A}_m$ by solving the Helmholtz equations (2.33) and (2.36).

2.2.2 Green's Function

The fundamental solution to the Helmholtz equation in free space is called the Green's function, denoted G_k, obtained by considering a Dirac delta function δ on the right hand side as

$$\nabla^2 G_k(\boldsymbol{r}) + k^2\, G_k(\boldsymbol{r}) = -\delta(\boldsymbol{r})\,. \tag{2.41}$$

With the additional constraint imposing that the wave must travel outward and vanish at infinity, expressed through the Sommerfeld (or Silver-Müller) radiation condition

$$\lim_{\|\boldsymbol{r}\|\to\infty} \|\boldsymbol{r}\| \left(\frac{\partial G_k(\boldsymbol{r})}{\partial \|\boldsymbol{r}\|} + \mathrm{j}k\, G_k(\boldsymbol{r}) \right) = 0\,, \tag{2.42}$$

the expression for the Green's function in free space reads

$$G_k(\boldsymbol{r}) = \frac{\mathrm{e}^{-\mathrm{j}k\|\boldsymbol{r}\|}}{4\pi\|\boldsymbol{r}\|}\,, \tag{2.43}$$

where $\|\cdot\|$ represents the Euclidean norm. By convolving eq. (2.41) with, for example, $\mu\boldsymbol{j}(\boldsymbol{r})$ on both sides, we derive the following equation

$$\mu\nabla^2 \iiint_V G_k(\boldsymbol{r}-\boldsymbol{r}')\,\boldsymbol{j}(\boldsymbol{r}')\,\mathrm{d}\boldsymbol{r}' + \mu k^2 \iiint_V G_k(\boldsymbol{r}-\boldsymbol{r}')\,\boldsymbol{j}(\boldsymbol{r}')\,\mathrm{d}\boldsymbol{r}' = -\mu\boldsymbol{j}(\boldsymbol{r})\,, \tag{2.44}$$

where V is the volume containing the sources. From this equality, we can identify the expression for the vector potential $\boldsymbol{A}_e$ as

$$\boldsymbol{A}_e(\boldsymbol{r}) = \mu \iiint_V \frac{\mathrm{e}^{-\mathrm{j}k\|\boldsymbol{r}-\boldsymbol{r}'\|}}{4\pi\|\boldsymbol{r}-\boldsymbol{r}'\|}\,\boldsymbol{j}(\boldsymbol{r}')\,\mathrm{d}\boldsymbol{r}'\,. \tag{2.45}$$

Similarly, by convolution with $\epsilon\,\boldsymbol{m}(\boldsymbol{r})$, the vector potential $\boldsymbol{A}_m$ is written

$$\boldsymbol{A}_m(\boldsymbol{r}) = \epsilon \iiint_V \frac{\mathrm{e}^{-\mathrm{j}k\|\boldsymbol{r}-\boldsymbol{r}'\|}}{4\pi\|\boldsymbol{r}-\boldsymbol{r}'\|}\,\boldsymbol{m}(\boldsymbol{r}')\,\mathrm{d}\boldsymbol{r}'\,. \tag{2.46}$$

Replacing these expressions into eqs. (2.39) and (2.40), we obtain the fields generated by the current densities $\boldsymbol{j}$ and $\boldsymbol{m}$ in free space

$$\begin{aligned}\boldsymbol{E}(\boldsymbol{r}) = -\mathrm{j}\omega\mu \iiint_V G_k(\boldsymbol{r},\boldsymbol{r}')\,\boldsymbol{j}(\boldsymbol{r}')\,\mathrm{d}\boldsymbol{r}' + \frac{1}{\mathrm{j}\omega\epsilon}\,\nabla\Big(\nabla\cdot \iiint_V G_k(\boldsymbol{r},\boldsymbol{r}')\,\boldsymbol{j}(\boldsymbol{r}')\,\mathrm{d}\boldsymbol{r}'\Big) \\ - \nabla\times \iiint_V G_k(\boldsymbol{r},\boldsymbol{r}')\,\boldsymbol{m}(\boldsymbol{r}')\,\mathrm{d}\boldsymbol{r}'\,,\end{aligned} \tag{2.47}$$

$$\begin{aligned}\boldsymbol{H}(\boldsymbol{r}) = \nabla\times \iiint_V G_k(\boldsymbol{r},\boldsymbol{r}')\,\boldsymbol{j}(\boldsymbol{r}')\,\mathrm{d}\boldsymbol{r}' + \frac{1}{\mathrm{j}\omega\mu}\,\nabla\Big(\nabla\cdot \iiint_V G_k(\boldsymbol{r},\boldsymbol{r}')\,\boldsymbol{m}(\boldsymbol{r}')\,\mathrm{d}\boldsymbol{r}'\Big) \\ - \mathrm{j}\omega\epsilon \iiint_V G_k(\boldsymbol{r},\boldsymbol{r}')\,\boldsymbol{m}(\boldsymbol{r}')\,\mathrm{d}\boldsymbol{r}'\,,\end{aligned} \tag{2.48}$$

where the Green's function has been rewritten as $G_k(\boldsymbol{r},\boldsymbol{r}') = G_k(\boldsymbol{r}-\boldsymbol{r}')$.

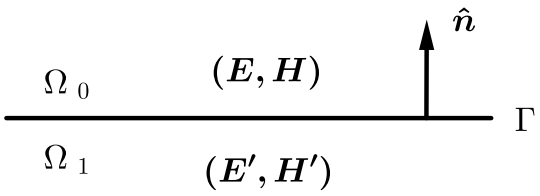

Figure 2.1: Interface between two media Ω_0 and Ω_1.

2.3 Formulation of Integral Equations

2.3.1 Boundary Conditions

The fields derivation from Maxwell's equations in the previous section is valid in free space. When an obstacle is present, a discontinuity is introduced along its surface. In this case, boundary conditions are defined to express this discontinuity. We consider the interface between an object Ω_1 with boundary Γ and the outside medium Ω_0. Electromagnetic fields $(\boldsymbol{E}, \boldsymbol{H})$ and $(\boldsymbol{E}', \boldsymbol{H}')$ are propagating inside Ω_0 and Ω_1, respectively. The unit normal $\hat{\boldsymbol{n}}$ to the surface points toward Ω_0, as illustrated in Figure 2.1. The discontinuities for the electric and magnetic fields are expressed through the following boundary conditions

$$\boldsymbol{j}_s = \hat{\boldsymbol{n}} \times (\boldsymbol{H} - \boldsymbol{H}')\,, \tag{2.49}$$
$$\boldsymbol{m}_s = -\hat{\boldsymbol{n}} \times (\boldsymbol{E} - \boldsymbol{E}')\,, \tag{2.50}$$

where $\boldsymbol{j}_s$ and $\boldsymbol{m}_s$ are electric and magnetic surface current densities tangential to the surface boundary.

2.3.2 Surface Equivalence Principle

We are interested in the problem of scattering by an object Ω_1 in the presence of an exciting electromagnetic field $(\boldsymbol{E}, \boldsymbol{H})$ in the outside medium Ω_0. The incident fields induce currents inside the object, which in turn generate scattered fields. Consider the original problem illustrated in Figure 2.2a. According to the surface equivalence principle, the fields $(\boldsymbol{E}, \boldsymbol{H})$ inside the object can be replaced by other virtual fields $(\boldsymbol{E}', \boldsymbol{H}')$ provided that suitable surface current densities are placed on Γ. According to the boundary conditions given previously, they are defined as

$$\boldsymbol{j}_s = \hat{\boldsymbol{n}} \times (\boldsymbol{H} - \boldsymbol{H}')\,, \tag{2.51}$$
$$\boldsymbol{m}_s = -\hat{\boldsymbol{n}} \times (\boldsymbol{E} - \boldsymbol{E}')\,. \tag{2.52}$$

Due to the uniqueness theorem [54], the fields generated by these current densities are the same as those of the original problem. This creates the equivalent problem shown in Figure 2.2b. In particular, the interior fields can be chosen so that

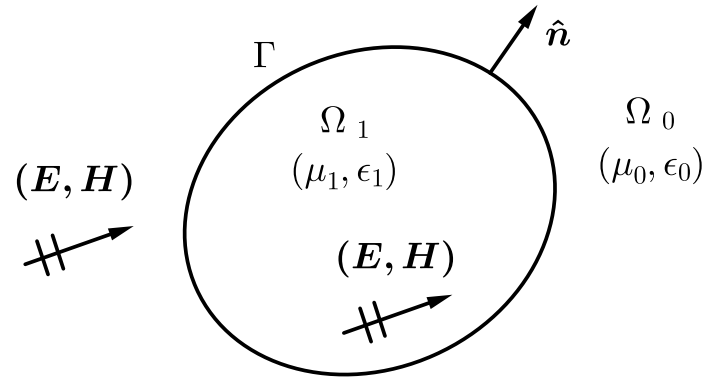

(a)

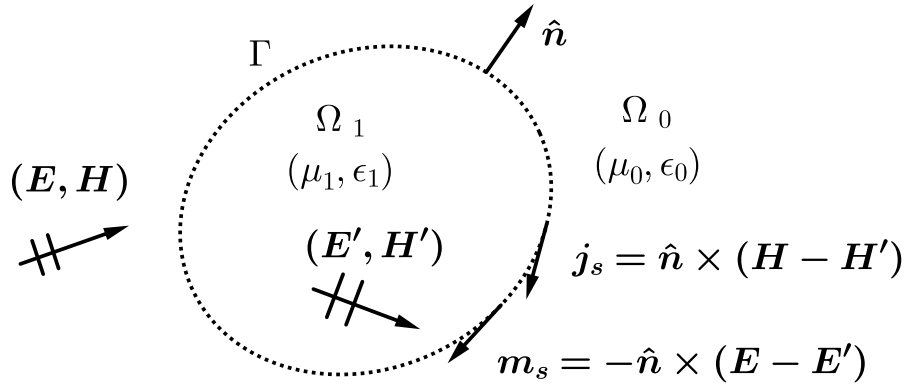

(b)

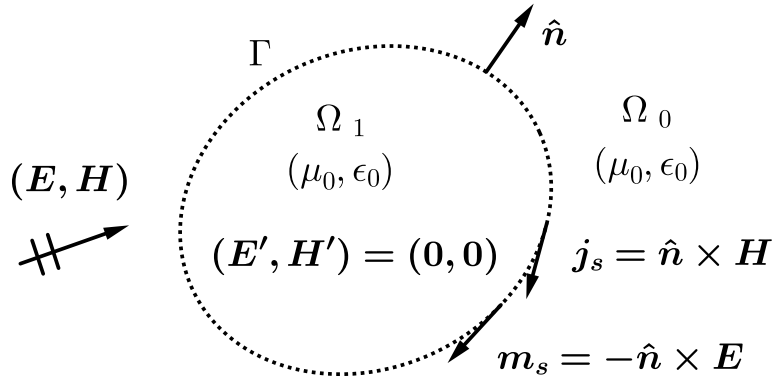

(c)

Figure 2.2: Surface equivalence principle: (a) Original problem, (b) equivalent problem, and (c) equivalent problem where the interior fields are equal to zero and the interior medium is identical to the exterior medium.

$(\boldsymbol{E}', \boldsymbol{H}') = (\mathbf{0}, \mathbf{0})$, which results in

$$\boldsymbol{j}_s = \hat{\boldsymbol{n}} \times \boldsymbol{H}\,, \tag{2.53}$$
$$\boldsymbol{m}_s = -\hat{\boldsymbol{n}} \times \boldsymbol{E}\,. \tag{2.54}$$

Since the fields are null, the interior medium can be substituted to be identical to the outside medium, creating a free space environment in which the expressions of the electric and magnetic fields (2.47) and (2.48) become valid, as illustrated in Figure 2.2c.

2.3.3 Electric and Magnetic Field Integral Equations

The scenarios studied in our work involve Perfect Electric Conductors (PEC) and dielectrics, for which the equivalence principle can be applied according to their properties. In both cases, the quantities to be calculated are the surface current densities $\boldsymbol{j}_s$ and $\boldsymbol{m}_s$ from which the scattered fields can be obtained. Therefore, the volume integrals involved in the determination of the electric and magnetic fields (2.39) and (2.40) are reduced to integrals on the surface Γ only. In this setting, a few remarks need to be considered regarding the expressions of the various integrals.

Due to a singularity that occurs on the boundary [66, 84], an additional term appears from the curl of the vector potentials (2.45) and (2.46). Considering a point $\boldsymbol{r}_0 \in \Gamma$ and $\boldsymbol{r}$ approaching the surface from outside, this is written as

$$\lim_{\boldsymbol{r}\to\boldsymbol{r}_0} \nabla \times \iint_\Gamma G_k(\boldsymbol{r}, \boldsymbol{r}')\, \boldsymbol{f}(\boldsymbol{r}')\, \mathrm{d}\boldsymbol{r}' = -\frac{1}{2}\, \hat{\boldsymbol{n}}(\boldsymbol{r}_0) \times \boldsymbol{f}(\boldsymbol{r}_0) + \nabla \times p.v. \iint_\Gamma G_k(\boldsymbol{r}_0, \boldsymbol{r}')\, \boldsymbol{f}(\boldsymbol{r}')\, \mathrm{d}\boldsymbol{r}'\,, \tag{2.55}$$

where $\boldsymbol{f}$ can be $\boldsymbol{j}_s$ or $\boldsymbol{m}_s$, and $p.v.$ denotes the principal value of the integral. From now on, we omit the notation for the principal value. Moreover, vector identities are used to move the curl operator inside the integral on Γ

$$\nabla \times \iint_\Gamma G_k(\boldsymbol{r}, \boldsymbol{r}')\, \boldsymbol{f}(\boldsymbol{r}')\, \mathrm{d}\boldsymbol{r}' = \iint_\Gamma \nabla G_k(\boldsymbol{r}, \boldsymbol{r}') \times \boldsymbol{f}(\boldsymbol{r}')\, \mathrm{d}\boldsymbol{r}'\,, \tag{2.56}$$

as well as the divergence operator for the double derivative term,

$$\nabla(\nabla \cdot \iint_\Gamma G_k(\boldsymbol{r}, \boldsymbol{r}')\, \boldsymbol{f}(\boldsymbol{r}')\, \mathrm{d}\boldsymbol{r}') = \nabla \iint_\Gamma G_k(\boldsymbol{r}, \boldsymbol{r}')\, \nabla' \cdot \boldsymbol{f}(\boldsymbol{r}')\, \mathrm{d}\boldsymbol{r}'\,. \tag{2.57}$$

The primed divergence indicates that the derivative is taken with respect to the primed variable $\boldsymbol{r}'$.

Next, we define integral operators on Γ to rewrite the fields conveniently. We first introduce the electric operator $\boldsymbol{\mathcal{T}}_k$, which is the sum of the vector and scalar

potential operators $\boldsymbol{\mathcal{T}}_{A,k}$ and $\boldsymbol{\mathcal{T}}_{\Phi,k}$, respectively,

$$\boldsymbol{\mathcal{T}}_k = -\mathrm{j}k\boldsymbol{\mathcal{T}}_{A,k} + \frac{1}{\mathrm{j}k}\boldsymbol{\mathcal{T}}_{\Phi,k}\,, \tag{2.58}$$

$$(\boldsymbol{\mathcal{T}}_{A,k}\boldsymbol{f})(\boldsymbol{r}) = \hat{\boldsymbol{n}} \times \iint_\Gamma G_k(\boldsymbol{r},\boldsymbol{r}')\,\boldsymbol{f}(\boldsymbol{r}')\,\mathrm{d}\boldsymbol{r}'\,, \tag{2.59}$$

$$(\boldsymbol{\mathcal{T}}_{\Phi,k}\boldsymbol{f})(\boldsymbol{r}) = \hat{\boldsymbol{n}} \times \nabla \iint_\Gamma G_k(\boldsymbol{r},\boldsymbol{r}')\,\nabla' \cdot \boldsymbol{f}(\boldsymbol{r}')\,\mathrm{d}\boldsymbol{r}'\,. \tag{2.60}$$

Then, we have the magnetic operator $\boldsymbol{\mathcal{K}}_k$, defined as

$$(\boldsymbol{\mathcal{K}}_k\boldsymbol{f})(\boldsymbol{r}) = \hat{\boldsymbol{n}} \times \iint_\Gamma \nabla G_k(\boldsymbol{r},\boldsymbol{r}') \times \boldsymbol{f}(\boldsymbol{r}')\,\mathrm{d}\boldsymbol{r}'\,. \tag{2.61}$$

Now, omitting the position vector for clarity, we take the cross product of the scattered fields (2.47) and (2.48) with the normal vector on Γ to obtain

$$\hat{\boldsymbol{n}} \times \boldsymbol{E}^s = \eta\,\boldsymbol{\mathcal{T}}_k(\boldsymbol{j}_s) - \frac{1}{2}\,\boldsymbol{m}_s - \boldsymbol{\mathcal{K}}_k(\boldsymbol{m}_s)\,, \tag{2.62}$$

$$\hat{\boldsymbol{n}} \times \boldsymbol{H}^s = \frac{1}{2}\,\boldsymbol{j}_s + \boldsymbol{\mathcal{K}}_k\,(\boldsymbol{j}_s) + \frac{1}{\eta}\,\boldsymbol{\mathcal{T}}_k(\boldsymbol{m}_s)\,, \tag{2.63}$$

where we have used the property that, for any vector $\boldsymbol{v}$ tangent to Γ,

$$\hat{\boldsymbol{n}} \times (\hat{\boldsymbol{n}} \times \boldsymbol{v}) = -\boldsymbol{v}\,, \tag{2.64}$$

and $\eta = \sqrt{\mu/\epsilon}$ is the impedance of the medium. We then need to include the incident fields $\boldsymbol{E}^i$ and $\boldsymbol{H}^i$ to the equations, given that

$$\boldsymbol{j}_s = \hat{\boldsymbol{n}} \times \boldsymbol{H}^i + \hat{\boldsymbol{n}} \times \boldsymbol{H}^s\,, \tag{2.65}$$

$$\boldsymbol{m}_s = -\hat{\boldsymbol{n}} \times \boldsymbol{E}^i - \hat{\boldsymbol{n}} \times \boldsymbol{E}^s\,, \tag{2.66}$$

from which the surface equations become

$$-\hat{\boldsymbol{n}} \times \boldsymbol{E}^i = \eta\,\boldsymbol{\mathcal{T}}_k(\boldsymbol{j}_s) + \frac{1}{2}\,\boldsymbol{m}_s - \boldsymbol{\mathcal{K}}_k(\boldsymbol{m}_s)\,, \tag{2.67}$$

$$-\hat{\boldsymbol{n}} \times \boldsymbol{H}^i = -\frac{1}{2}\,\boldsymbol{j}_s + \boldsymbol{\mathcal{K}}_k(\boldsymbol{j}_s) + \frac{1}{\eta}\,\boldsymbol{\mathcal{T}}_k(\boldsymbol{m}_s)\,. \tag{2.68}$$

These two equations are respectively called the Electric and Magnetic Field Integral Equations, commonly abbreviated as EFIE and MFIE.

In particular, PECs are widely employed as an ideal model for good conductors, allowing for several simplifications. For instance, there is no electric field inside such objects, and the surface magnetic current density is null. In other words, $\boldsymbol{m}_s = \boldsymbol{0}$, and the EFIE for PECs reads

$$\eta\,\boldsymbol{\mathcal{T}}_k(\boldsymbol{j}_s) = -\hat{\boldsymbol{n}} \times \boldsymbol{E}^i\,. \tag{2.69}$$

Similarly, the MFIE for PECs is

$$-\frac{1}{2}\,\boldsymbol{j}_s + \boldsymbol{\mathcal{K}}_k(\boldsymbol{j}_s) = -\hat{\boldsymbol{n}} \times \boldsymbol{H}^i\,. \tag{2.70}$$

2.3.4 Poggio-Miller-Chang-Harrington-Wu-Tsai Equation

In the case of dielectrics, the fields are derived from both the electric and magnetic currents. Additionally, to include the properties of the interior medium, the equivalence principle is applied by exchanging the roles of the exterior and interior media to cancel the exterior fields, thus creating another set of equations. Through this manipulation, the material parameters of the object are properly taken into account.

Consider a dielectric Ω_1 of electric permittivity ϵ_1 and magnetic permeability μ_1, as illustrated in Figure 2.3. The object is illuminated from the exterior by an electromagnetic wave $(\boldsymbol{E}^i, \boldsymbol{H}^i)$. First, the EFIE (2.67) is defined on the surface, outside and inside, to obtain

$$\eta_0 \boldsymbol{\mathcal{T}}_{k_0}(\boldsymbol{j}_s) - \frac{1}{2}\boldsymbol{m}_s - \boldsymbol{\mathcal{K}}_{k_0}(\boldsymbol{m}_s) = -\hat{\boldsymbol{n}} \times \boldsymbol{E}^i \qquad \text{in } \Omega_0\,, \tag{2.71}$$

$$\eta_1 \boldsymbol{\mathcal{T}}_{k_1}(\boldsymbol{j}_s) + \frac{1}{2}\boldsymbol{m}_s - \boldsymbol{\mathcal{K}}_{k_1}(\boldsymbol{m}_s) = \boldsymbol{0} \qquad \text{in } \Omega_1\,. \tag{2.72}$$

Both equations are then summed, canceling the identity terms and resulting in the first equation on the surface Γ

$$\eta_0 \boldsymbol{\mathcal{T}}_{k_0}(\boldsymbol{j}_s) + \eta_1 \boldsymbol{\mathcal{T}}_{k_1}(\boldsymbol{j}_s) - \boldsymbol{\mathcal{K}}_{k_0}(\boldsymbol{m}_s) - \boldsymbol{\mathcal{K}}_{k_1}(\boldsymbol{m}_s) = -\hat{\boldsymbol{n}} \times \boldsymbol{E}^i\,. \tag{2.73}$$

The same procedure is then followed for the MFIE (2.68), which gives

$$-\frac{1}{2}\boldsymbol{j}_s + \boldsymbol{\mathcal{K}}_{k_0}(\boldsymbol{j}_s) + \frac{1}{\eta_0}\boldsymbol{\mathcal{T}}_{k_0}(\boldsymbol{m}_s) = -\hat{\boldsymbol{n}} \times \boldsymbol{H}^i \qquad \text{in } \Omega_0\,, \tag{2.74}$$

$$\frac{1}{2}\boldsymbol{j}_s + \boldsymbol{\mathcal{K}}_{k_1}(\boldsymbol{j}_s) + \frac{1}{\eta_1}\boldsymbol{\mathcal{T}}_{k_1}(\boldsymbol{m}_s) = \boldsymbol{0} \qquad \text{in } \Omega_1\,. \tag{2.75}$$

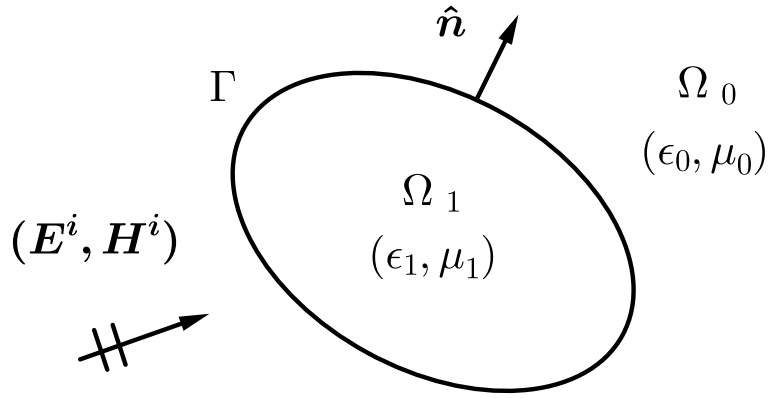

Figure 2.3: Dielectric object Ω_1 immersed in the air in the presence of an incident electromagnetic field $(\boldsymbol{E}^i, \boldsymbol{H}^i)$.

After summation, the second integral equation reads

$$\boldsymbol{\mathcal{K}}_{k_0}(\boldsymbol{j}_s) + \boldsymbol{\mathcal{K}}_{k_1}(\boldsymbol{j}_s) + \frac{1}{\eta_0}\boldsymbol{\mathcal{T}}_{k_0}(\boldsymbol{m}_s) + \frac{1}{\eta_1}\boldsymbol{\mathcal{T}}_{k_1}(\boldsymbol{m}_s) = -\hat{\boldsymbol{n}} \times \boldsymbol{H}^i \,. \tag{2.76}$$

Together, eqs. (2.73) and (2.76) form a system of two equations with two unknowns, written compactly under block matrix form as

$$\begin{pmatrix} \eta_0\boldsymbol{\mathcal{T}}_{k_0} + \eta_1\boldsymbol{\mathcal{T}}_{k_1} & -(\boldsymbol{\mathcal{K}}_{k_0} + \boldsymbol{\mathcal{K}}_{k_1}) \\ \boldsymbol{\mathcal{K}}_{k_0} + \boldsymbol{\mathcal{K}}_{k_1} & \frac{1}{\eta_0}\boldsymbol{\mathcal{T}}_{k_0} + \frac{1}{\eta_1}\boldsymbol{\mathcal{T}}_{k_1} \end{pmatrix} \begin{pmatrix} \boldsymbol{j}_s \\ \boldsymbol{m}_s \end{pmatrix} = \begin{pmatrix} -\hat{\boldsymbol{n}} \times \boldsymbol{E}^i \\ -\hat{\boldsymbol{n}} \times \boldsymbol{H}^i \end{pmatrix} . \tag{2.77}$$

This formulation is broadly used to solve problems involving dielectrics and is called the Poggio-Miller-Chang-Harrington-Wu-Tsai (PMCHWT) equation [71, 22, 94].

2.4 Boundary Element Method

Several prevalent approaches to model and study scattering and radiation problems in electromagnetism transform Maxwell's equations into matrix systems that can be solved numerically. Among them is the BEM, also called the Method of Moments (MoM) in electromagnetism, which only requires to model the boundaries between different linear and homogeneous media. This leads to relatively small, but dense matrices. In contrast, the Finite Element Method (FEM) requires the discretization of the entire volume, increasing the dimension of the problem by one although the resulting matrices are sparse. Furthermore, often approximate boundary conditions need to be defined in the case of the FEM whereas this is intrinsically enforced in the BEM.

2.4.1 Geometry Discretization

The BEM is used to solve linear boundary value equations of the form

$$\boldsymbol{\mathcal{Z}}\boldsymbol{x} = \boldsymbol{b} \,, \tag{2.78}$$

where $\boldsymbol{x}$ is an unknown quantity defined on the surface of an object. The first step to build the matrix equation is the discretization of the surfaces of interest. In three dimensions, surfaces are typically divided into flat triangular or quadrilateral elements, with the former being preferred for its better flexibility in modeling both smooth and sharp shapes.

The main parameter for the meshing procedure is the size of the elements, characterized by the average edge length, usually denoted as h. Ideally, the elements should be as regular and homogeneous as possible and small enough to capture geometrical details. A simple example is illustrated in Figure 2.4 with the discretization of a sphere, in which the first two meshes are unsatisfactory. Additionally, the

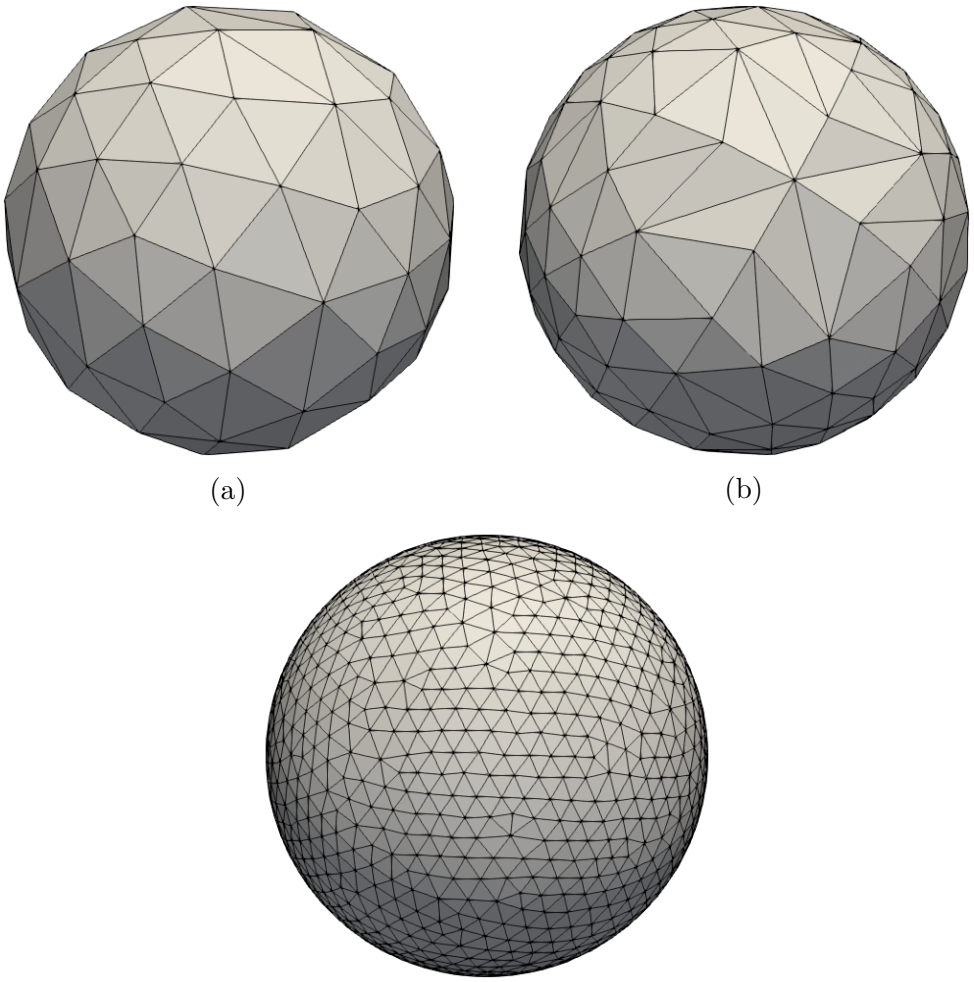

(a) (b)

(c)

Figure 2.4: Discretization of a sphere with radius 1 m: (a) Coarse mesh ($h = 0.4\,\mathrm{m}$), (b) Irregular mesh ($h = 0.3\,\mathrm{m}$) and (c) Fine mesh ($h = 0.1\,\mathrm{m}$).

Nyquist-Shannon sampling theorem imposes that $h < \lambda/2$, where λ is the wavelength. In this work, for instance, we construct meshes with the requirement that $h < \lambda/10$ to increase reliability and precision, which is especially relevant for higher frequencies. On the other hand, the more elements, the larger the discretized problem becomes, slowing down the entire solving process. A balance must therefore be carefully established between accuracy and speed when considering the geometry and simulating conditions.

2.4.2 Basis Functions

The constructed mesh serves as the support for the basis functions used to discretize the unknown of the equation. These functions can be either scalar or vectorial, depending on the nature of the unknown quantity. In practice, basis functions are chosen to exhibit the same properties as the unknown to be represented. Specifically, they must have sufficient derivability as imposed by the operators in which they appear.

In the case of vectorial quantities such as surface vector fields or current densities, we introduce the widely used divergence-conforming Rao-Wilton-Glisson (RWG) basis functions [75] defined on pairs of triangular elements as

$$\boldsymbol{f}_i(\boldsymbol{r}) = \begin{cases} \dfrac{l_i}{2A_i^+}\,(\boldsymbol{r} - \boldsymbol{r}_i^+) & \text{if } \boldsymbol{r} \in c_i^+ \\ \dfrac{l_i}{2A_i^-}\,(\boldsymbol{r}_i^- - \boldsymbol{r}) & \text{if } \boldsymbol{r} \in c_i^- \end{cases} , \tag{2.79}$$

where $c_i^\pm$ form a pair of adjacent triangles with respective areas $A_i^\pm$ and common edge e_i of length l_i, and $\boldsymbol{r}_i^\pm$ are the position vectors of the vertices opposite to the common edge. An example of RWG function is illustrated in Figure 2.5.

For scalar quantities, such as potentials or normal components of vectorial values, we define the pulse basis functions, which are essentially the indicator functions for each cell element c_i

$$p_i(\boldsymbol{r}) = \begin{cases} 1 & \text{if } \boldsymbol{r} \in c_i \\ 0 & \text{if } \boldsymbol{r} \notin c_i \end{cases} . \tag{2.80}$$

Once the functions have been selected, a vectorial unknown $\boldsymbol{y}$ can be decomposed with RWG functions as

$$\boldsymbol{y}(\boldsymbol{r}) \approx \sum_{i=1}^{N_e} a_i \boldsymbol{f}_i(\boldsymbol{r}) , \tag{2.81}$$

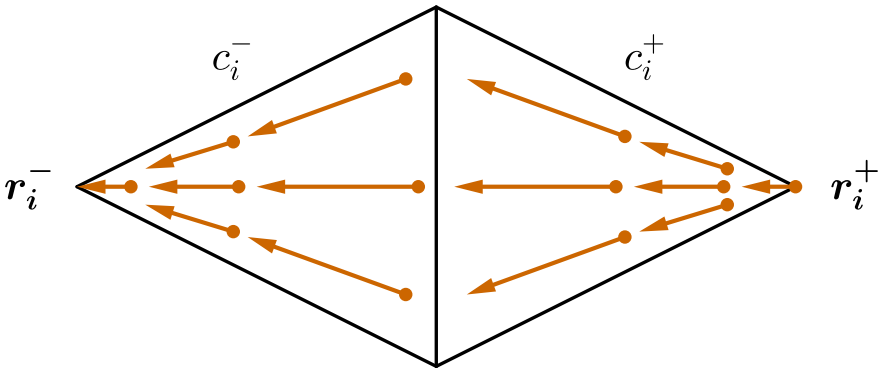

Figure 2.5: RWG function on a pair of triangular elements.

where N_e is the number of mesh internal edges. For a scalar unknown x, the decomposition with pulse functions is

$$x(\boldsymbol{r}) \approx \sum_{i=1}^{N_c} b_i p_i(\boldsymbol{r}) \ , \tag{2.82}$$

where N_c is the number of mesh elements. Following this strategy, the coefficients $\{a_i,\ i = 1 \dots N_e\}$ and $\{b_i,\ i = 1 \dots N_c\}$ then become the unknowns of the discretized equation.

2.4.3 Matrix Building

The decomposition of the unknown(s) constitutes half of the discretization process. Given that there are now N unknowns, we need N independent equations to uniquely solve the system. This is achieved with N testing or weighting functions by integrating the original equation over their respective supports. The operator appearing in the integral equation under study maps the set of unknowns to the range and the testing functions must be chosen in the dual of the range of the operator.

We consider the vector potential operator (2.59) as an example to illustrate the procedure. For a testing function $\boldsymbol{g}_m$ and a source function $\boldsymbol{f}_n$, the corresponding operator integral reads

$$\langle \boldsymbol{g}_m, \boldsymbol{\mathcal{T}}_{A,k}(\boldsymbol{f}_n) \rangle = \iint_\Gamma \boldsymbol{g}_m(\boldsymbol{r}) \cdot \hat{\boldsymbol{n}} \times \iint_\Gamma G_k(\boldsymbol{r}, \boldsymbol{r}') \boldsymbol{f}_n(\boldsymbol{r}') \, \mathrm{d}\boldsymbol{r}' \mathrm{d}\boldsymbol{r} \, . \tag{2.83}$$

In practice, the difficulty of the implementation of such integrals depends on the operator and the selected basis functions, requiring careful treatment when dealing with singularities arising due to the Green's function. When the distance between the respective supports of the testing and source functions is sufficiently large, the integral does not present singularities. In this case, simple approaches such as the Gaussian quadrature are amply satisfying. However, if the testing and source function domains are very close or overlap, specific schemes such as singularity extraction [44, 40, 53, 86, 93] or singularity cancellation [38, 45, 89] need to be used to ensure that the integrals are computed accurately.

To build the entire matrix equation, the right hand side needs to be tested as well with each function. For a given function $\boldsymbol{g}_m$, the corresponding right hand side element is

$$\langle \boldsymbol{g}_m, \boldsymbol{b} \rangle = \iint_\Gamma \boldsymbol{g}_m(\boldsymbol{r}) \cdot \boldsymbol{b}(\boldsymbol{r}) \, \mathrm{d}\boldsymbol{r} \, . \tag{2.84}$$

We also write the unknown decomposition as described before

$$\boldsymbol{x}(\boldsymbol{r}) \approx \sum_{i=1}^{N} x_i \boldsymbol{f}_i(\boldsymbol{r}) \ . \tag{2.85}$$

Therefore, the matrix equation obtained with the BEM becomes

$$\mathbf{Zx} = \mathbf{b} \Leftrightarrow \begin{pmatrix} Z_{11} & Z_{12} & \dots & Z_{1N} \\ Z_{21} & Z_{22} & & Z_{2N} \\ \vdots & & \ddots & \vdots \\ Z_{N1} & Z_{N2} & \dots & Z_{NN} \end{pmatrix} \begin{pmatrix} x_1 \\ x_2 \\ \vdots \\ x_N \end{pmatrix} = \begin{pmatrix} b_1 \\ b_2 \\ \vdots \\ b_N \end{pmatrix} . \tag{2.86}$$

From here, a naive approach to solve this equation is simply to invert the matrix $\mathbf{Z}$ and calculate

$$\mathbf{x} = \mathbf{Z}^{-1}\mathbf{b} . \tag{2.87}$$

Although this is a valid method in most cases, it is extremely expensive in terms of computation time and memory, especially with a high number of unknowns. Moreover, if the matrix does not exhibit adequate properties, this approach can fail entirely, as will be discussed in the following chapter.

Chapter 3

Introduction on Preconditioning for Integral Equations

Computational electromagnetics is a scientific field in which Maxwell's equations are transformed and manipulated to be solved numerically. The previous chapter presented the Boundary Element Method (BEM) that discretizes integral equations for a variety of propagation scenarios. One of the major challenges is to develop computationally efficient and stable solvers, in terms of time and memory consumption. In particular, the aim is to have the solving process be as fast and accurate as possible regardless of the selected parameters and simulating conditions. We start with an overview of the computational complexity of the BEM and a brief presentation of fast solver techniques, then introduce the essential role of the matrix condition number and its influence on the performance of integral equation solvers. We also describe the classic example of the low frequency breakdown for the Electric Field Integral Equation (EFIE) and detail preconditioning methods based on the quasi-Helmholtz decomposition.

3.1 Computational Complexity

For relatively simple problems, discretized via the BEM with a small number of unknowns N, the solution can be obtained with acceptable time and memory consumption by following a naive approach. The matrices of the discretized operators are computed explicitly element by element, which results in a time complexity of $\mathcal{O}(N^2)$ and a memory storage of $\mathcal{O}(N^2)$. Here the Laudau symbol $\mathcal{O}$ implies $N \to \infty$. The computation of the right hand side vector, instead, has time and memory complexities of $\mathcal{O}(N)$. From there, the simplest way to solve the equation is to directly invert the system matrix, which is an operation with a higher time cost of $\mathcal{O}(N^3)$. Therefore the overall complexity of a naive boundary element solver is $\mathcal{O}(N^3)$ in time and $\mathcal{O}(N^2)$ in memory.

When the discretization of the problem requires a higher number of elements, for instance to model large objects, small geometric details, or for high frequency simulations, the computation becomes unaffordably expensive. Clearly, acceleration strategies are necessary to generalize the use of the BEM and to allow for more sophisticated scenarios. For this reason, different techniques are available in literature that have been developed to offer a better performance, achieving overall time and memory complexities down to quasi-linear with $\mathcal{O}(N \log N)$ [25]. Among the most widespread algorithms are the Adaptive Cross Approximation (ACA) [12, 100], the Multi Level Matrix Decomposition Algorithm (MLMDA) [63, 77], the Fast Multipole Method (FMM) [46, 30], and its enhanced version, the Multi Level Fast Multipole Method (MLFMM) [60, 82, 81]. These strategies typically generate a compressed form of the system matrix to bypass its full explicit construction. Moreover, they are designed to allow fast matrix-vector products, with which integral equations can be solved using Krylov subspace iterative solvers [47] such as the Conjugate Gradient Squared (CGS) [50, 83, 80] or the Generalized Minimal Residual Method (GMRES) [79, 11]. In general, the convergence of these solvers is not guaranteed for every problem and their choice is motivated by the properties of the system matrix, for instance, symmetry or positive definiteness. Assuming that there exists an iterative solver that converges for the scenario under consideration, we denote as N_{iter} the number of iterations required until convergence to a solution. The overall time complexity is thus $\mathcal{O}(N_{\text{iter}} N \log N)$.

Ideally, the number of iterations should be kept constant so as to reach and maintain a cost of $\mathcal{O}(N \log N)$. The notion of preconditioning is closely related to the convergence speed of these iterative solvers. As will become clear in the next section, the condition number of the equation matrix influences the number of iterations, and thus the optimization of the solver complexity.

3.2 Matrix Condition Number

For any linear and invertible matrix $\mathbf{A} \in \mathbb{C}^{N \times N}$, its condition number is defined as

$$\begin{aligned} \kappa(\mathbf{A}) &= \|\mathbf{A}\|.\|\mathbf{A}^{-1}\| \\ &= \frac{\sigma_{\max}(\mathbf{A})}{\sigma_{\min}(\mathbf{A})}, \end{aligned} \tag{3.1}$$

where $\|\cdot\|$ represents the matrix 2-norm or spectral norm, and σ denotes singular values, with $\sigma_{\max}(\mathbf{A})$ being the maximum and $\sigma_{\min}(\mathbf{A})$ the minimum singular value of $\mathbf{A}$. The condition number of a matrix, also called conditioning, acts as an indicator of its stability. For a linear equation of the form $\mathbf{Ax} = \mathbf{b}$, a small variation of the input will result in a larger variation in the output the higher the condition number of the matrix $\mathbf{A}$. Therefore, a small condition number is desirable as it

reflects a good stability and the matrix is said to be well-conditioned, with the smallest achievable condition number being $\kappa(\mathbf{A}) = 1$, attained for any unitary matrix. On the contrary, for a large unbounded condition number, which can be infinite, the problem is ill-conditioned. In this case, iterative solvers are unlikely to produce a solution in a reasonable amount of time or may converge to an incorrect result. Instead, a low condition number is usually a good indicator of fast and stable convergence [24]. This property is crucial to reach an optimal time complexity of $\mathcal{O}(N \log N)$.

For a given equation system, the condition number may vary depending on different parameters, such as the frequency of simulation, the level of mesh discretization or the material properties. This can lead to strong ill-conditioning in some cases (e.g. low frequency, fine discretization), thus severely limiting the applicability of those integral equations. The concept of preconditioning focuses on the improvement and stabilization of the matrix conditioning, with the best results obtained via strategies tailored to the desired formulations and target scenarios.

3.3 Low Frequency Breakdown of the EFIE

In this section, we will present the ill-conditioning of the EFIE for Perfect Electric Conductors (PEC) (2.69) at low frequencies. This issue has been widely treated in literature [92, 8, 21, 98, 72, 96] and thus constitutes a good reference example to develop a better understanding of the importance of preconditioning. In the low frequency regime, we consider $k \to 0$ while the mesh discretization remains fixed. The line delimiting low and high frequency can be roughly determined by the electrical size of the object under study. For instance, if the largest dimension of the object is larger or smaller than the wavelength, the frequency is considered to be high or low, respectively. For an object of diameter $a = 1\,\mathrm{m}$, the low frequency regime can be considered when

$$ka = \frac{2\pi f}{c} \ll 1\,, \tag{3.2}$$

where f is the frequency, and c is the speed of light in vacuum. Expressed with the frequency on the left hand side, we have

$$f \ll \frac{c}{2\pi} \approx 4.8 \times 10^7 \mathrm{Hz}\,, \tag{3.3}$$

corresponding to frequencies below the order of the MHz, which involves many practical applications. For this reason, the ill-conditioning of the EFIE holds a lot of interest in computational electromagnetics.

We recall the electric operator composed of the vector and scalar potential operators

$$\boldsymbol{\mathcal{T}}_k = -\mathrm{j}k\boldsymbol{\mathcal{T}}_{A,k} + \frac{1}{\mathrm{j}k}\boldsymbol{\mathcal{T}}_{\Phi,k}\,. \tag{3.4}$$

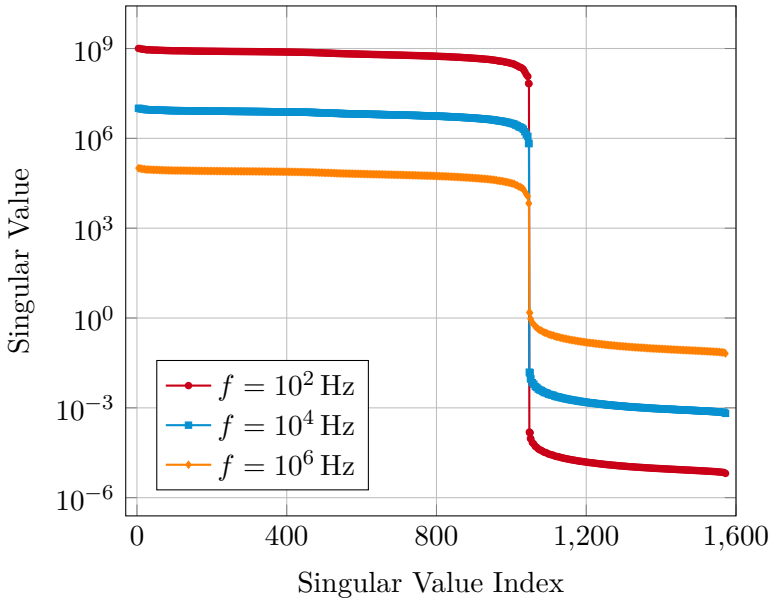

Figure 3.1: Singular value decomposition of the EFIO at different frequencies for a sphere of radius 1 m.

When the frequency decreases, the first term behaves as $\mathcal{O}(k)$, whereas the second term follows $\mathcal{O}(1/k)$. In the rest of the chapter, the $\mathcal{O}$ notation implies $k \to 0$. Due to these reciprocal scalings, one term vanishes while the other grows unbounded as the frequency tends to zero. To evaluate the impact on the condition number, we examine the variation of the singular value spectrum for the Electric Field Integral Operator (EFIO) at different frequencies. The spectrum of the electric operator is plotted in Figure 3.1 for a sphere of radius 1 m, discretized with 1048 elements and 1572 unknowns. The condition numbers obtained at these frequencies are given in Table 3.1 and indicate a growth following $\mathcal{O}(1/k^2)$. This is the low frequency ill-conditioning of the EFIO, which is the most treated BEM breakdown due to the popularity of the EFIE. One of the available strategies is based on the decomposition of the equation into solenoidal and non-solenoidal components, which is presented next.

Table 3.1: Condition number of the EFIO at varying frequencies for a sphere of radius 1 m.

Frequency	Condition number
10^{2} Hz	1.55×10^{14}
10^{4} Hz	1.54×10^{10}
10^{6} Hz	1.54×10^{6}

3.4 Quasi-Helmholtz Decomposition

In vector calculus, the Helmholtz decomposition theorem states that any vector field $\boldsymbol{F}$ that is sufficiently smooth and rapidly decays at infinity can be decomposed into a solenoidal part $\boldsymbol{F}_s$ and an irrotational part $\boldsymbol{F}_i$. In other words,

$$\boldsymbol{F} = \boldsymbol{F}_s + \boldsymbol{F}_i \,, \tag{3.5}$$

with

$$\nabla \cdot \boldsymbol{F} = \nabla \cdot \boldsymbol{F}_i \,, \quad \nabla \times \boldsymbol{F} = \nabla \times \boldsymbol{F}_s \,. \tag{3.6}$$

Instead, a quasi-Helmholtz decomposition is a separation into a solenoidal component $\boldsymbol{F}_s$ and a non-solenoidal one $\boldsymbol{F}_{ns}$, rather than irrotational, i.e.

$$\boldsymbol{F} = \boldsymbol{F}_s + \boldsymbol{F}_{ns} \,, \tag{3.7}$$

with

$$\nabla \cdot \boldsymbol{F} = \nabla \cdot \boldsymbol{F}_{ns} \,, \quad \nabla \times \boldsymbol{F} = \nabla \times \boldsymbol{F}_s + \nabla \times \boldsymbol{F}_{ns} \,. \tag{3.8}$$

This concept has been used as a remedy to the low frequency breakdown of the EFIE. It can be implemented in practice with the Loop-Star or Loop-Tree decompositions [87, 98, 58, 39], which are made of functions defined as linear combinations of Rao-Wilton-Glisson (RWG) basis functions. In the following, we will consider the Loop-Star decomposition, but the reasoning is still valid for the Loop-Tree version. The Loop and Star basis functions span the entire RWG space, the first set being solenoidal and the second set being non-solenoidal.

We first redefine the RWG functions (2.79) without the edge length normalization, which gives

$$\boldsymbol{f}_i(\boldsymbol{r}) = \begin{cases} \dfrac{\boldsymbol{r} - \boldsymbol{r}_i^+}{2A_i^+} & \text{if } \boldsymbol{r} \in c_i^+ \\ \dfrac{\boldsymbol{r}_i^- - \boldsymbol{r}}{2A_i^-} & \text{if } \boldsymbol{r} \in c_i^- \end{cases} , \tag{3.9}$$

where $A_i^\pm$ is the area of the triangle $c_i^\pm$ and $\boldsymbol{r}_i^\pm$ is the position vector of the vertex that does not belong to the common edge, as illustrated in Figure 3.2. The edge length factor has been removed from the RWG functions so that the flux integral through their defining edge equals one [5]. As a consequence, the expressions for the Loop to RWG and Star to RWG transformation matrices, respectively denoted as $\boldsymbol{\Lambda}$ and $\boldsymbol{\Sigma}$, are also simplified.

Given the configuration displayed in Figure 3.2, the transformation matrices

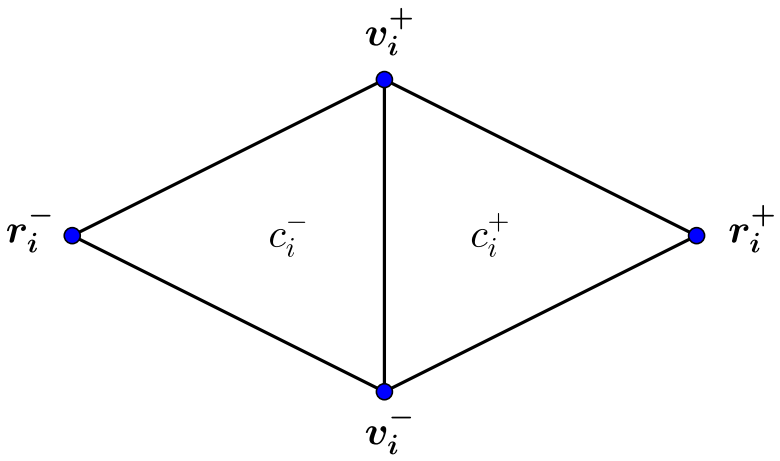

Figure 3.2: Notation used for the definition of RWG functions and Loop-Star transformation matrices.

can be constructed from mesh connectivity information with the following rules

$$(\boldsymbol{\Lambda})_{ij} = \begin{cases} 1 & \text{if node } j \text{ equals } \boldsymbol{v}_i^+ \\ -1 & \text{if node } j \text{ equals } \boldsymbol{v}_i^- \\ 0 & \text{otherwise}\,, \end{cases} \tag{3.10}$$

$$(\boldsymbol{\Sigma})_{ij} = \begin{cases} 1 & \text{if cell } j \text{ equals } c_i^+ \\ -1 & \text{if cell } j \text{ equals } c_i^- \\ 0 & \text{otherwise}\,. \end{cases} \tag{3.11}$$

The columns of these matrices are however not linearly independent. This can be seen with Euler's polyhedron formula that states, for a simply connected closed geometry,

$$N_{\text{vertices}} + N_{\text{cells}} = N_{\text{edges}} + 2\,. \tag{3.12}$$

In other words, since each vertex, cell or edge supports a Loop, Star or RWG function, respectively, there is an excess of two functions to form linearly independent bases. For this reason, the Loop-Star procedure requires that one arbitrary column must be eliminated from each matrix. In the following, we always assume linear independence of the columns for the matrices $\boldsymbol{\Lambda}$ and $\boldsymbol{\Sigma}$.

Loop functions $\boldsymbol{\lambda}_i$ are defined on mesh vertices and form a counterclockwise flow along the surrounding cells that share the base vertex, as illustrated in Figure 3.3a, while Star functions $\boldsymbol{\sigma}_i$, defined on mesh cells, flow outward from the center of the cell to the adjacent cells, which can be seen in Figure 3.3b. Any matrix $\boldsymbol{\mathsf{Z}}$ discretized with RWG basis functions can then be decomposed by applying these

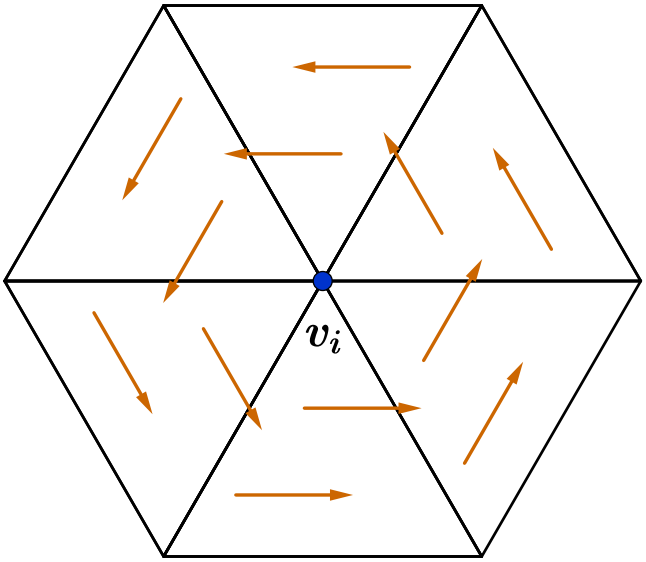

(a)

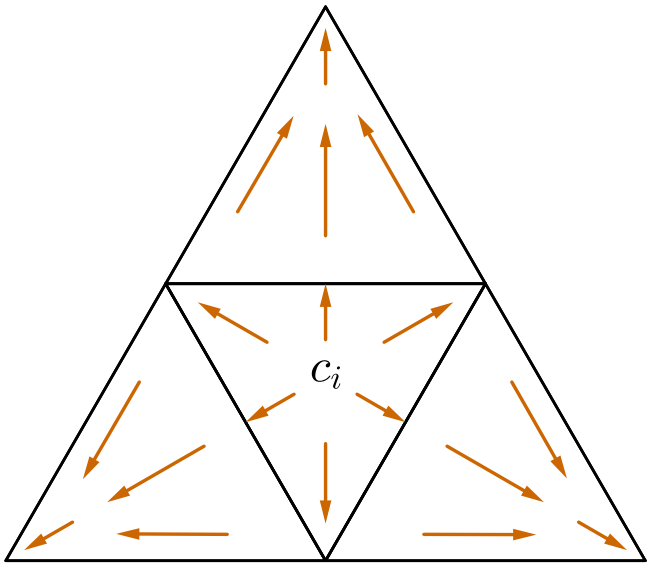

(b)

Figure 3.3: (a) Loop and (b) Star functions defined on triangular elements.

transformation matrices following

$$\begin{aligned} \mathbf{Z_{LS}} &= \begin{pmatrix} \mathbf{\Lambda} & \mathbf{\Sigma} \end{pmatrix}^{\mathrm{T}} \mathbf{Z} \begin{pmatrix} \mathbf{\Lambda} & \mathbf{\Sigma} \end{pmatrix} \\ &= \mathbf{A}^{\mathrm{T}} \mathbf{Z} \mathbf{A} \,, \end{aligned} \tag{3.13}$$

where $\mathbf{A}$ is the Loop-Star decomposition matrix. The decomposed matrix can then

be written in block form as

$$\mathsf{Z}_{\mathsf{LS}} = \begin{pmatrix} \mathsf{Z}_{\mathsf{\Lambda\Lambda}} & \mathsf{Z}_{\mathsf{\Lambda\Sigma}} \\ \mathsf{Z}_{\mathsf{\Sigma\Lambda}} & \mathsf{Z}_{\mathsf{\Sigma\Sigma}} \end{pmatrix} , \tag{3.14}$$

where, for each block, the first index indicates the testing space and the second index indicates the source space for the basis functions. This decomposition method can be used to study and scale the blocks according to the problem at hand. To achieve this, the Loop and Star transformation matrices are multiplied with adequately selected scalar coefficients to remove any conditioning breakdown.

In the case of the EFIO, the vector and scalar potentials operators can be rescaled separately through this decomposition. Consider first the classic discretization of the operator $\boldsymbol{\mathcal{T}}_{\Phi,k}$ with RWG basis functions for the source and rotated RWG functions for the testing part. The element (m, n) of the operator matrix is written explicitly as

$$(\mathsf{T}_{\Phi,k})_{mn} = \iint_\Gamma \hat{\boldsymbol{n}} \times \boldsymbol{f}_m(\boldsymbol{r}) \cdot \hat{\boldsymbol{n}} \times \nabla \iint_\Gamma G_k(\boldsymbol{r}, \boldsymbol{r}')\, \nabla' \cdot \boldsymbol{f}_n(\boldsymbol{r}')\, \mathrm{d}\boldsymbol{r}'\mathrm{d}\boldsymbol{r} \tag{3.15}$$

$$= \iint_\Gamma \boldsymbol{f}_m(\boldsymbol{r}) \cdot \nabla \iint_\Gamma G_k(\boldsymbol{r}, \boldsymbol{r}')\, \nabla' \cdot \boldsymbol{f}_n(\boldsymbol{r}')\, \mathrm{d}\boldsymbol{r}'\mathrm{d}\boldsymbol{r} \tag{3.16}$$

$$= -\iint_\Gamma \nabla \cdot \boldsymbol{f}_m(\boldsymbol{r}) \iint_\Gamma G_k(\boldsymbol{r}, \boldsymbol{r}')\, \nabla' \cdot \boldsymbol{f}_n(\boldsymbol{r}')\, \mathrm{d}\boldsymbol{r}'\mathrm{d}\boldsymbol{r}\,. \tag{3.17}$$

The passage from (3.15) to (3.16) is done by considering

$$\boldsymbol{a} = \boldsymbol{f}_m(\boldsymbol{r})\,, \tag{3.18}$$

$$\boldsymbol{b} = \nabla \iint_\Gamma G_k(\boldsymbol{r}, \boldsymbol{r}')\, \nabla' \cdot \boldsymbol{f}_n(\boldsymbol{r}')\, \mathrm{d}\boldsymbol{r}'\,, \tag{3.19}$$

and applying the vector relation

$$\begin{aligned} (\hat{\boldsymbol{n}} \times \boldsymbol{a}) \cdot (\hat{\boldsymbol{n}} \times \boldsymbol{b}) &= \boldsymbol{b} \cdot ((\hat{\boldsymbol{n}} \times \boldsymbol{a}) \times \hat{\boldsymbol{n}}) \\ &= \boldsymbol{b} \cdot (-(\hat{\boldsymbol{n}} \cdot \boldsymbol{a})\, \hat{\boldsymbol{n}} + (\hat{\boldsymbol{n}} \cdot \hat{\boldsymbol{n}})\, \boldsymbol{a}) \\ &= -(\hat{\boldsymbol{n}} \cdot \boldsymbol{a})(\hat{\boldsymbol{n}} \cdot \boldsymbol{b}) + \boldsymbol{b} \cdot \boldsymbol{a} \\ &= \boldsymbol{a} \cdot \boldsymbol{b}\,, \end{aligned} \tag{3.20}$$

obtained by using scalar and vector triple products rules, as well as the fact that $\boldsymbol{a}$ is tangential, i.e. has no normal component. Equation (3.17) then follows from (3.16) by applying an integration by parts to move the gradient operator to the testing function. This relation highlights the property that whenever solenoidal Loop functions appear as testing or source functions, the corresponding matrix element for the scalar potential operator cancels out, since for any i, $\nabla \cdot \boldsymbol{\lambda}_i = \boldsymbol{0}$ by definition. This property can also be interpreted more simply in matrix form as

$$\mathsf{\Lambda}^{\mathrm{T}} \mathsf{T}_{\Phi,k} = \mathsf{T}_{\Phi,k} \mathsf{\Lambda} = \mathsf{0}\,. \tag{3.21}$$

As a result, the Loop-Star decomposed EFIE matrix becomes

$$\begin{aligned}\mathbf{Z}_{\mathbf{LS}} &= \begin{pmatrix} \mathbf{\Lambda}^{\mathrm{T}}\mathbf{T}_{A,k}\mathbf{\Lambda} & \mathbf{\Lambda}^{\mathrm{T}}\mathbf{T}_{A,k}\mathbf{\Sigma} \\ \mathbf{\Sigma}^{\mathrm{T}}\mathbf{T}_{A,k}\mathbf{\Lambda} & \mathbf{\Sigma}^{\mathrm{T}}(\mathbf{T}_{\Phi,k}+\mathbf{T}_{A,k})\mathbf{\Sigma} \end{pmatrix} \\ &= \begin{pmatrix} \mathcal{O}(k) & \mathcal{O}(k) \\ \mathcal{O}(k) & \mathcal{O}(1/k) \end{pmatrix} . \end{aligned} \tag{3.22}$$

From this decomposition, a bound on the condition number at low frequency can be obtained with the Gershgorin circle theorem [42], given below.

Theorem 1 (Gershgorin circle theorem)**.** *Let $\mathbf{A} \in \mathbb{C}^{N\times N}$ be a matrix with elements $(\mathbf{A})_{mn} = a_{mn}$. For any $i = 1, \ldots, N$, we define $R_i = \sum_{j\neq i} |a_{ij}|$, and $\overline{D}(a_{ii}, R_i)$ the closed disk of center a_{ii} and radius R_i. Then, for any λ eigenvalue of $\mathbf{A}$, there exists an index i such that $\lambda \in \overline{D}(a_{ii}, R_i)$.*

Applying this theorem leads to the identification of two eigenvalue clusters: one disk $\overline{D}(\mathcal{O}(k), \mathcal{O}(k))$ whose center and radius approach zero following $\mathcal{O}(k)$, and another disk $\overline{D}(\mathcal{O}(1/k), \mathcal{O}(k))$ with a center going to infinity and a vanishing radius. Although the condition number is calculated from the singular values of the matrix, when the latter is Hermitian and positive definite, they coincide with the eigenvalues. This is notably the case in the low frequency limit. Additionally, the obtained bounds corroborate the $\mathcal{O}(1/k^2)$ behavior of the condition number observed from the spectrum.

Based on this matrix study of the EFIO, the default asymptotic behavior of the vector and scalar potentials can be adjusted in the diagonal blocks by scaling them respectively with factors equal to $1/k$ and k. This can be achieved with the scaled decomposition matrix

$$\mathbf{A}_s = \begin{pmatrix} \frac{1}{\sqrt{k}}\mathbf{\Lambda} & \sqrt{k}\,\mathbf{\Sigma} \end{pmatrix} , \tag{3.23}$$

which is applied left and right of the system matrix as in (3.13), hence the square roots $1/\sqrt{k}$ and $\sqrt{k}$. Thus the matrix equation $\mathbf{Z}\mathbf{x} = \mathbf{b}$ after preconditioning is

$$\mathbf{A}_s^{\mathrm{T}}\mathbf{Z}\mathbf{A}_s\mathbf{y} = \mathbf{A}_s^{\mathrm{T}}\mathbf{b} , \tag{3.24}$$

where $\mathbf{y}$ is the auxiliary solution with

$$\mathbf{x} = \mathbf{A}_s\mathbf{y} . \tag{3.25}$$

The ensuing asymptotic scalings for the preconditioned matrix are

$$\mathbf{A}_s^{\mathrm{T}}\mathbf{Z}\mathbf{A}_s = \begin{pmatrix} \mathcal{O}(1) & \mathcal{O}(k) \\ \mathcal{O}(k) & \mathcal{O}(1) \end{pmatrix} , \tag{3.26}$$

for which the Gershgorin circle theorem now shows that the eigenvalues are clustered around constant values with vanishing radii. The singular value spectrum for

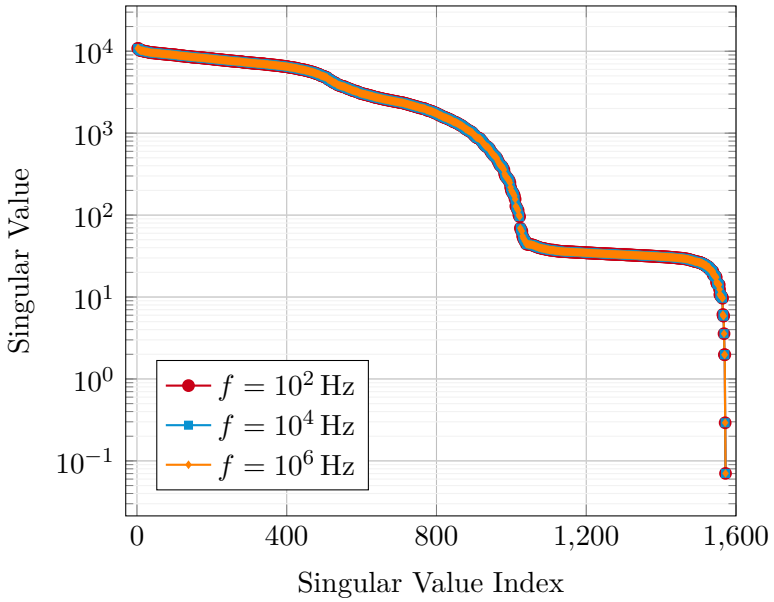

Figure 3.4: Singular value decomposition of the EFIO preconditioned using a Loop-Star scheme at different frequencies for a sphere of radius 1 m.

the preconditioned matrix is displayed at different frequencies in Figure 3.4, for the same sphere of radius 1 m simulated in the previous section. The conditioning of the matrix now remains constant for any low frequency, with a value of 1.54×10^5. The spectrum branches that were previously diverging with decreasing frequencies are still visible but perfectly stable.

Although this strategy is effective in stabilizing the condition number, a couple of limitations are present. The Loop and Star functions effectively span the RWG space in the case of closed simply connected structures. However, geometries that contain holes or handles, such as rings, cannot be supported with only these two sets of functions and their treatment is detailed later in this chapter. Additionally, the transformation matrices $\mathbf{\Lambda}$ and $\mathbf{\Sigma}$ are applied at the cost of introducing an increase of the condition number linked to the level of discretization of the geometry [3, 1], which becomes particularly disadvantageous when fine meshes must be used.

3.5 Loss of Accuracy at Very Low Frequency

The introduction of the Loop-Star decomposition enables the analysis of a separate issue appearing at very low frequencies. Given that the solenoidal and non-solenoidal components of the solution may have different asymptotic behaviors as the frequency decreases (e.g. $\mathcal{O}(1)$ for one and $\mathcal{O}(k)$ for the other), one component would eventually dominate the other (e.g. $\mathcal{O}(1) \gg \mathcal{O}(k)$). Due to the limitations

of machine precision, this can result in a partial loss of the solution, which is an additional aspect to consider when providing a cure to the low frequency problem, as solely addressing the matrix breakdown is not necessarily sufficient to obtain an accurate solution. Moreover, this may also result in strong inaccuracies when computing derived quantities such as the electric far field [97, 24].

To provide a clearer understanding, we will examine the asymptotic scalings of the solution for the EFIE with a plane wave as the excitation. First, we need to determine the behavior of the right hand side, defined as

$$-\hat{\boldsymbol{n}} \times \boldsymbol{E}^i(\boldsymbol{r}) = -\hat{\boldsymbol{n}} \times \boldsymbol{E}_0 \, \mathrm{e}^{-\mathrm{j}k\hat{\boldsymbol{k}}\cdot\boldsymbol{r}} \,, \tag{3.27}$$

where $\hat{\boldsymbol{k}}$ is a unit vector indicating the direction of propagation and $\boldsymbol{E}_0 = E_0 \, \hat{\boldsymbol{p}}$, with E_0 representing the peak amplitude and $\hat{\boldsymbol{p}}$ the polarization of the electric field. The m^{th} element of the discretized right hand side is then written as

$$\begin{aligned}(\mathbf{b})_m &= -\iint_\Gamma \hat{\boldsymbol{n}} \times \boldsymbol{f}_m(\boldsymbol{r}) \cdot \hat{\boldsymbol{n}} \times \boldsymbol{E}_0 \, \mathrm{e}^{-\mathrm{j}k\hat{\boldsymbol{k}}\cdot\boldsymbol{r}} \, \mathrm{d}\boldsymbol{r} \\ &= -\iint_\Gamma \boldsymbol{f}_m(\boldsymbol{r}) \cdot \boldsymbol{E}_0 \, \mathrm{e}^{-\mathrm{j}k\hat{\boldsymbol{k}}\cdot\boldsymbol{r}} \, \mathrm{d}\boldsymbol{r} \,. \end{aligned} \tag{3.28}$$

To ascertain the low frequency scalings, we expand the exponential using the Maclaurin series with k as the variable

$$\begin{aligned}(\mathbf{b})_m &= -\iint_\Gamma \boldsymbol{f}_m(\boldsymbol{r}) \cdot \boldsymbol{E}_0 \sum_{n=0}^{\infty} \frac{(-\mathrm{j}k\hat{\boldsymbol{k}} \cdot \boldsymbol{r})^n}{n!} \, \mathrm{d}\boldsymbol{r} \\ &\approx -\iint_\Gamma \boldsymbol{f}_m(\boldsymbol{r}) \cdot \boldsymbol{E}_0 \left(1 - \mathrm{j}k\hat{\boldsymbol{k}} \cdot \boldsymbol{r} + \mathcal{O}(k^2)\right) \mathrm{d}\boldsymbol{r} \,. \end{aligned} \tag{3.29}$$

When $k \to 0$, the first term of the expansion is dominant as $\mathcal{O}(1)$. However, a particular case occurs when a Loop function is used for testing. For any Loop function $\boldsymbol{\lambda}_i$, there exists a scalar function P_i on Γ such that [87]

$$\boldsymbol{\lambda}_i(\boldsymbol{r}) = \hat{\boldsymbol{n}}(\boldsymbol{r}) \times \nabla P_i(\boldsymbol{r}) \,. \tag{3.30}$$

Then, applying Stokes' theorem, we have

$$\iint_\Gamma \boldsymbol{\lambda}_i(\boldsymbol{r}) \, \mathrm{d}\boldsymbol{r} = \iint_\Gamma \hat{\boldsymbol{n}}(\boldsymbol{r}) \times \nabla P_i(\boldsymbol{r}) \, \mathrm{d}\boldsymbol{r} = \oint_{\boldsymbol{r}\in\partial\Gamma} P_i(\boldsymbol{r}) \, \mathrm{d}\boldsymbol{l} = \boldsymbol{0} \,. \tag{3.31}$$

Therefore, the second term in $\mathcal{O}(k)$ dominates and the Loop-Star decomposed right hand side reads

$$\mathbf{A}^{\mathrm{T}}\mathbf{b} = \begin{pmatrix} \mathcal{O}(k) \\ \mathcal{O}(1) \end{pmatrix} \,. \tag{3.32}$$

Next, the inverse of the decomposed EFIE matrix (3.22) can be derived with a block matrix inversion using the Schur complement [49], which results in

$$(\mathbf{A}^{\mathrm{T}}\mathbf{Z}\mathbf{A})^{-1} = \begin{pmatrix} \mathcal{O}(1/k) & \mathcal{O}(k) \\ \mathcal{O}(k) & \mathcal{O}(k) \end{pmatrix} \,. \tag{3.33}$$

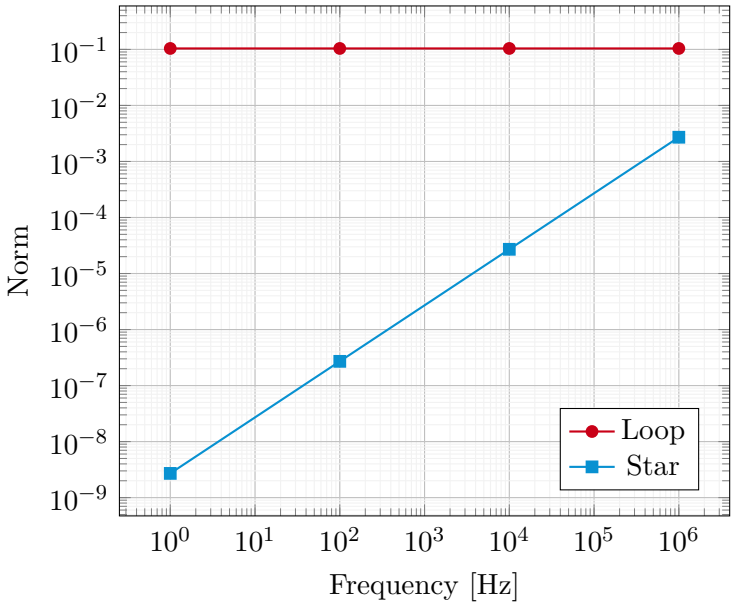

Figure 3.5: Norms of the Loop and Star components of the auxiliary solution of the EFIO at different frequencies for a sphere of radius 1 m.

Finally, recalling the Loop-Star decomposed equation $\mathbf{A}^{\mathrm{T}}\mathbf{Z}\mathbf{A}\mathbf{y} = \mathbf{A}^{\mathrm{T}}\mathbf{b}$, the auxiliary solution is thus obtained as

$$\mathbf{y} = (\mathbf{A}^{\mathrm{T}}\mathbf{Z}\mathbf{A})^{-1}\mathbf{A}^{\mathrm{T}}\mathbf{b} = \begin{pmatrix} \mathcal{O}(1) \\ \mathcal{O}(k) \end{pmatrix} . \tag{3.34}$$

The Loop component of the solution scales as $\mathcal{O}(1)$, dominating the Star component which follows $\mathcal{O}(k)$, as illustrated in Figure 3.5. As a result, the Star part of the solution is lost when the frequency becomes very small, illustrating the issue delineated above.

By selecting appropriate rescaling coefficients, the balance can be restored between the components. For instance, the factors chosen previously for the Loop-Star preconditioned EFIE result in the auxiliary solution

$$\begin{aligned} \mathbf{y}_s &= (\mathbf{A}_s^{\mathrm{T}}\mathbf{Z}\mathbf{A}_s)^{-1}\mathbf{A}_s^{\mathrm{T}}\mathbf{b} \\ &= \begin{pmatrix} \mathcal{O}(1) & \mathcal{O}(k) \\ \mathcal{O}(k) & \mathcal{O}(1) \end{pmatrix} \begin{pmatrix} \mathcal{O}(k^{1/2}) \\ \mathcal{O}(k^{1/2}) \end{pmatrix} \\ &= \begin{pmatrix} \mathcal{O}(k^{1/2}) \\ \mathcal{O}(k^{1/2}) \end{pmatrix} , \end{aligned} \tag{3.35}$$

where both components scale as $\mathcal{O}(k^{1/2})$. Therefore, the selection of rescaling factors for the Loop-Star scheme must take into account the behavior of the desired quantities of interest on top of the matrix preconditioning to guarantee a good accuracy.

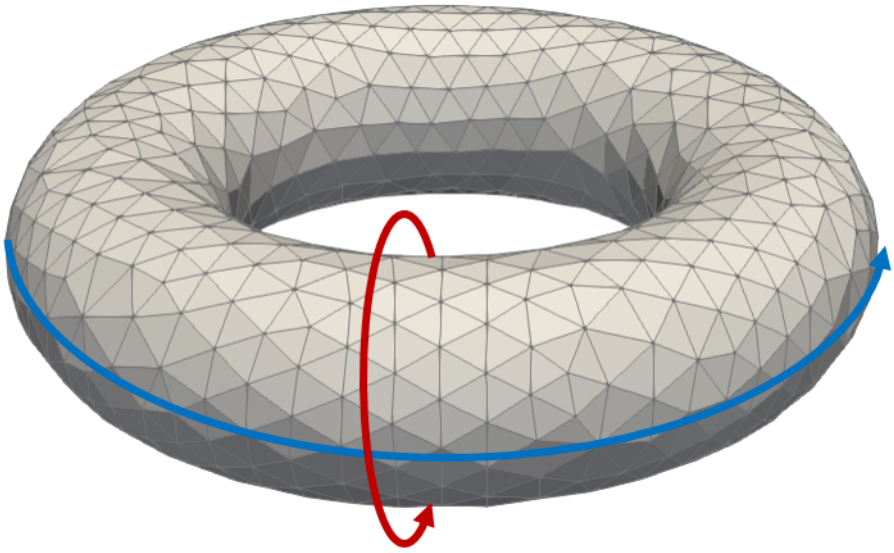

Figure 3.6: Discretized torus containing one handle and two global loops: poloidal (red) and toroidal (blue).

3.6 Global Loops and Harmonic Subspace

Geometries including handles are part of the family of multiply connected structures. These handles form global loops corresponding to the harmonic subspace which is not covered by the original Loop-Star decomposition. When taking handles into consideration, Euler's formula becomes

$$2N_{\text{handles}} + N_{\text{vertices}} + N_{\text{cells}} = N_{\text{edges}} + 2\,, \tag{3.36}$$

meaning that each handle generates two global loops, as illustrated in Figure 3.6 through the example of a torus with circular cross section. For these, the associated transformation matrix, denoted as $\mathbf{H}$ and of size $N_{\text{edges}} \times 2N_{\text{handles}}$, needs to be constructed independently. The complete quasi-Helmholtz decomposition matrix then reads

$$\mathbf{A} = \begin{pmatrix} \mathbf{\Lambda} & \mathbf{H} & \mathbf{\Sigma} \end{pmatrix}\,. \tag{3.37}$$

Any global loop function $\boldsymbol{h}$, like local loops, is solenoidal, that is,

$$\nabla \cdot \boldsymbol{h}(\boldsymbol{r}) = 0\,. \tag{3.38}$$

Manually building the harmonic subspace is however a computationally expensive operation and is inadequate for inclusion into fast solvers [5]. Consequently, the explicit construction will not be discussed here, and details on the construction of this subspace can be found in [5, 32, 57, 92]. Alternative methods must preferably be used to account for the global loops without compromising the overall computational cost.

3.7 Quasi-Helmholtz Projectors

To bypass the expensive building of the global loops, as well as to avoid the ill-conditioning linked to the matrices $\mathbf{\Lambda}$ and $\mathbf{\Sigma}$, projectors based on the quasi-Helmholtz decomposition have been introduced first for the EFIE [5]. They have later been adapted to other formulations such as the Magnetic and Combined Field Integral Equations (MFIE and CFIE) [62] as well as the Poggio-Miller-Chang-Harrington-Wu-Tsai (PMCHWT) equation for dielectrics [13]. The quasi-Helmholtz projectors are built from the matrix $\mathbf{\Sigma}$ following

$$\mathbf{P}^{\mathbf{\Sigma}} = \mathbf{\Sigma}\left(\mathbf{\Sigma}^{\mathrm{T}}\mathbf{\Sigma}\right)^{+}\mathbf{\Sigma}^{\mathrm{T}}, \tag{3.39}$$

$$\mathbf{P}^{\mathbf{\Lambda H}} = \mathbf{I} - \mathbf{P}^{\mathbf{\Sigma}}, \tag{3.40}$$

where $^{+}$ represents the Moore-Penrose pseudo inverse and $\mathbf{I}$ the identity matrix. With this definition, the projector $\mathbf{P}^{\mathbf{\Sigma}}$ covers the entire non-solenoidal subspace. Because of the full column rank property of the Loop to RWG and Star to RWG matrices, together with the orthogonality between the Loop, harmonic and Star subspaces [5], the second projector $\mathbf{P}^{\mathbf{\Lambda H}}$ is obtained by subtracting $\mathbf{P}^{\mathbf{\Sigma}}$ from the identity matrix, thus generating a projector which accounts for all solenoidal functions, implicitly including the global loop functions. Any additional operation related to the global loops can be entirely avoided through this strategy. Moreover, it remains valid regardless of whether the geometry contains handles or not.

In practice, similarly to the Loop-Star method, each projector is scaled with an adequate coefficient. Afterward, a complete rescaling projector is built by adding them as

$$\mathbf{M} = \alpha\,\mathbf{P}^{\mathbf{\Lambda H}} + \beta\,\mathbf{P}^{\mathbf{\Sigma}}, \tag{3.41}$$

where $\alpha, \beta \in \mathbb{C}$ are the scaling factors. Given that the projector $\mathbf{P}^{\mathbf{\Lambda H}}$ applies to both local and global loops, the associated coefficient takes effect on both the Loop and harmonic subspaces. The matrix $\mathbf{M}$ is then multiplied left and right of the system matrix as for the Loop-Star case. The projector used to precondition the EFIO is thus

$$\mathbf{M} = \frac{1}{\sqrt{k}}\,\mathbf{P}^{\mathbf{\Lambda H}} + \mathrm{j}\sqrt{k}\,\mathbf{P}^{\mathbf{\Sigma}}, \tag{3.42}$$

where the imaginary number is added to prevent a loss of accuracy at low frequency as detailed in [5]. Lastly, the complete preconditioned equation reads

$$\mathbf{MZMy} = \mathbf{Mb}, \tag{3.43}$$

where $\mathbf{y}$ is the auxiliary solution with

$$\mathbf{x} = \mathbf{My}. \tag{3.44}$$

The corresponding singular value spectrum at the previously simulated frequencies and for the sphere of radius 1 m is displayed in Figure 3.7. The condition number

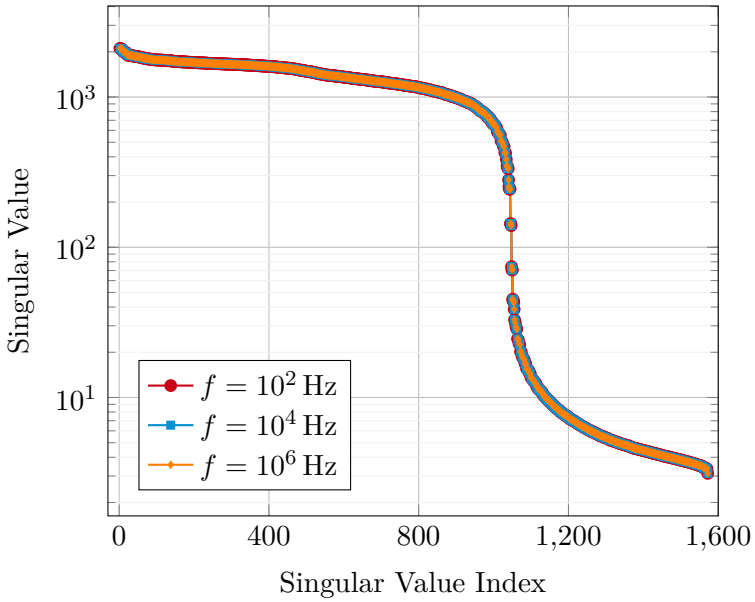

Figure 3.7: Singular value decomposition of the EFIO preconditioned using quasi-Helmholtz projectors at different frequencies for a sphere of radius 1 m.

obtained with the projector approach remains stable, with a value of 674, which is much lower than the one achieved with the Loop-Star method. For comparison, Figure 3.8 illustrates the spectra for the unpreconditioned EFIE, the Loop-Star preconditioned EFIE and the projector preconditioned EFIE at frequency $f = 10^2$ Hz on the sphere.

The illustrative case presented in this chapter demonstrates the significance of preconditioning methods to create stable equations which can then be accelerated with fast solvers. The subsequent chapters deal with intricate scenarios by going through detailed analyses and devising strategies to obtain well-conditioned formulations according to the specifics of the regimes of interest.

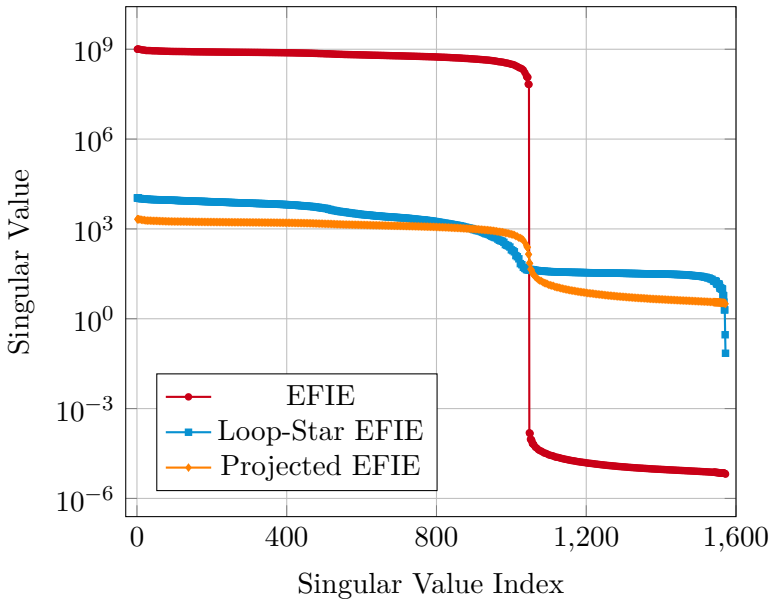

Figure 3.8: Singular value decomposition of different versions of the EFIO for $f = 10^2\,\mathrm{Hz}$ on a sphere of radius 1 m.

Chapter 4

Low Frequency Preconditioning Strategy For Eddy Current Modeling

This chapter introduces a well-conditioned full-wave method for the efficient simulation of eddy currents, which are electric currents induced inside conductors by time-varying magnetic fields. This particular type of electric current is a major aspect of many real-life applications, which is why a reliable modeling strategy is highly relevant. The majority of available methods to simulate eddy currents are based on a quasi-static approximation of Maxwell's equations. Consequently, these models are limited to small frequencies. Full-wave equations such as the Poggio-Miller-Chang-Harrington-Wu-Tsai (PMCHWT) formulation, however, are unstable and inaccurate under eddy current conditions. The novel strategy presented in this chapter extends the validity of the PMCHWT equation to support lossy conductors at lower frequencies and incorporate eddy currents. This method therefore remains valid at higher frequencies as well. This is achieved through the application of quasi-Helmholtz projectors, which offer several additional benefits. Among these are the implicit handling of multiply connected geometries with handles and the compatibility with a quasi-linear computational complexity. Simulation results are also presented to illustrate the effectiveness of the new formulation in different scenarios. The majority of the work introduced in this chapter has been published in the journal contribution [28], as well as initial findings in the conference publication [27].

4.1 Introduction

Eddy currents are electric currents induced inside conductors in the vicinity of a time-varying magnetic field. Efficient modeling of this phenomenon is highly

pertinent in the context of industrial applications which are involved in various ways [56]. From household purposes to manufacturing processes, eddy currents are used for instance in induction heating or metal detection. Most non destructive testing methods also rely on induced eddy currents to discern the presence of cracks and air bubbles inside conductive parts [18, 41]. The simulation of such scenarios is usually done with tailored solvers based on the quasi-static approximation of Maxwell's equations [78, 101]. Under this assumption, the displacement currents are neglected and removed from the equations. However, this simplification restricts the scope of these solvers to low frequencies [19, 36]. Moreover, existing methods often require additional preprocessing for multiply connected geometries in order to ensure the uniqueness of the solution. Such procedures include filling the holes with a fictitious conductivity [37] as well as introducing cutting surfaces to artificially remove them [76].

In contrast, the PMCHWT equation [71, 22, 94], which is often employed to model lossy conductors at high and medium frequencies, is a full-wave formulation, i.e. is based on the full Maxwell's equations. Nonetheless, a serious breakdown appears at low frequencies, thus affecting the simulation of eddy currents. This failure is a separate issue from the low frequency breakdown described for Perfect Electric Conductors (PEC) in Chapter 3, or for purely dielectric objects, for which several strategies have been presented in literature [92, 72, 68]. In the case of lossy conductors, the finite and non-negligible electrical conductivity of the material simulated at low frequencies results in a strong ill-conditioning of the equation. As explained in Chapter 3, the performance of iterative solvers typically used in fast methods is therefore heavily impacted. Furthermore, at very low frequencies, a loss of accuracy in the solution occurs similarly to the Electric Field Integral Equation (EFIE). As a consequence, this potentially prevents the correct computation of derived quantities of interest.

Remedies to the low frequency breakdown in lossy conductors have been presented in literature [102], frequently relying on Loop-Star or Loop-Tree decompositions [87, 88]. These techniques unfortunately exhibit a significant computation overhead due to their conditioning and the necessary detection of global loops. Additionally, the augmented EFIE [73] has also been applied to lossy conductors [95], but this extension is done at the cost of additional matrices to be computed and stored, thus increasing the overall computational cost. Amidst the various approaches, the quasi-Helmholtz projectors [5, 13, 62] present many attractive features compared with other techniques, including an implicit treatment of multiply connected structures and a compatibility with fast solvers running in quasi-linear computational complexity [30, 100]. Nonetheless, the projector-based approaches introduced in [5, 62] are only applicable for PECs. Likewise, the formulation based on the PMCHWT equation proposed in [13] has been obtained for purely dielectric materials. Therefore that low frequency preconditioner is not valid for lossy conductors since the presence of the finite conductivity significantly changes the

behavior of the lower diagonal block of the PMCHWT matrix.

This chapter provides an extension of the PMCHWT equation to eddy current applications through the use of quasi-Helmholtz projectors. The specific low frequency behavior created by the complex permittivity of the material is investigated via an ad hoc analysis to identify the source of the breakdown. A tailored strategy is then designed to deal with the different asymptotic scalings of the upper and lower diagonal blocks of the PMCHWT matrix. Standard and dual projectors are defined to ensure that: (i) divergent elements are removed, (ii) the rest of the matrix is not corrupted by a new source of breakdown, (iii) no null space is introduced, and (iv) sufficient accuracy is achieved at very low frequencies. The new full-wave approach can handle eddy current modeling by taking advantage of a new regularization scheme using quasi-Helmholtz projectors. The obtained formulation successfully fulfills conditions (i) to (iv). Precisely, the new method is well-conditioned, remains accurate at very low frequencies, smoothly shifts between low and high frequencies, and can be used with both simply and multiply connected geometries, while offering a low computational complexity. Note that the dense discretization breakdown, occurring when the mesh element size decreases, is not treated in this work.

The rest of the chapter is organized in the following manner. The specific background and notation are defined in Section 4.2. An eddy current model built with the Boundary Element Method (BEM) is then presented in Section 4.3. An extensive analysis of the PMCHWT equation behavior at low frequencies for conductors is detailed in Section 4.4, and is followed in Section 4.5 by the description of the procedure to build the new full-wave formulation. Supplementary details are contained in Section 4.6 regarding the numerical implementation. Finally, several numerical experiments are presented in Section 4.7 to support the development, after which Section 4.8 concludes the chapter.

4.2 Background and Notation

Let $\Omega_1 \subset \mathbb{R}^3$ be a closed lossy conductor with smooth boundary $\Gamma = \partial\Omega_1$ and outward pointing normal $\hat{\boldsymbol{n}}$, residing in the outside medium $\Omega_0 = \mathbb{R}^3 \backslash \overline{\Omega_1}$. Compared with the case of dielectrics, the conductor is also defined with a finite conductivity σ_1. The exterior vacuum medium is considered non conductive, with $\sigma_0 = 0\,\mathrm{S\,m^{-1}}$. Throughout this chapter, the indices $\{0,1\}$ represent the exterior and interior media, respectively. The complete configuration is illustrated in Figure 4.1 with an electromagnetic field $(\boldsymbol{E}^i, \boldsymbol{H}^i)$ illuminating the object.

The geometry can be either simply connected or include handles. The conductor is characterized by its constant permeability $\mu_1 = \mu_0\mu_r$, constant conductivity σ_1, and complex permittivity

$$\epsilon_1 = \epsilon_0\epsilon_r' - \mathrm{j}\,\frac{\sigma_1}{\omega}\,, \tag{4.1}$$

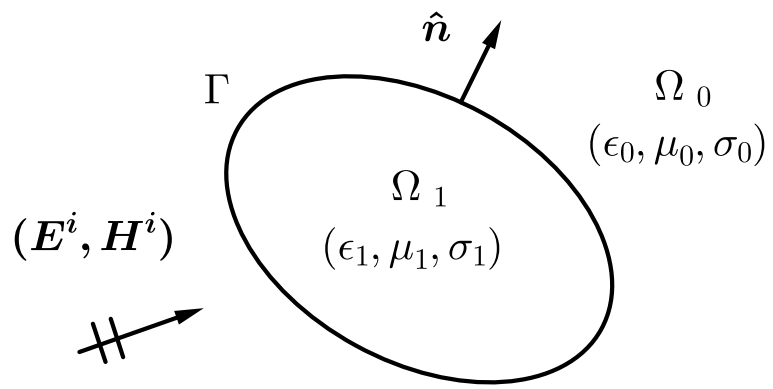

Figure 4.1: Conductive object Ω_1 immersed in the air in the presence of an incident electromagnetic field $(\boldsymbol{E}^i, \boldsymbol{H}^i)$.

where ϵ_r' is the real-valued relative permittivity and ω is the angular frequency. The eddy current conditions are characterized by the following relations [51, 36]

$$\begin{cases} \omega\epsilon_0 \ll \sigma_1 \\ L\omega\sqrt{\mu_0\epsilon_0} \ll 1\,, \end{cases} \tag{4.2}$$

where L is the characteristic size of the conductor. In these conditions, the interior wave number is

$$\begin{aligned} k_1 &= \omega\sqrt{\mu_1\epsilon_1} \\ &\approx \sqrt{-\mathrm{j}\omega\sigma_1\mu_1} \\ &\approx \frac{1-\mathrm{j}}{\delta}\,, \end{aligned} \tag{4.3}$$

where $\delta = \sqrt{2/(\omega\sigma_1\mu_1)}$ represents the skin depth and determines the concentration of current densities near the surface of the conductor (known as the skin effect) [36].

The electric and magnetic integral operators $\boldsymbol{\mathcal{T}}_k$ and $\boldsymbol{\mathcal{K}}_k$ are defined on Γ as in Chapter 2 (eqs. (2.58) and (2.61), respectively). We recall the PMCHWT integral equation (2.77) under matrix form [71, 22, 94],

$$\begin{pmatrix} \eta_0\boldsymbol{\mathcal{T}}_{k_0} + \eta_1\boldsymbol{\mathcal{T}}_{k_1} & -(\boldsymbol{\mathcal{K}}_{k_0} + \boldsymbol{\mathcal{K}}_{k_1}) \\ \boldsymbol{\mathcal{K}}_{k_0} + \boldsymbol{\mathcal{K}}_{k_1} & \frac{1}{\eta_0}\boldsymbol{\mathcal{T}}_{k_0} + \frac{1}{\eta_1}\boldsymbol{\mathcal{T}}_{k_1} \end{pmatrix} \begin{pmatrix} \boldsymbol{j}_s \\ \boldsymbol{m}_s \end{pmatrix} = \begin{pmatrix} -\hat{\boldsymbol{n}} \times \boldsymbol{E}^i \\ -\hat{\boldsymbol{n}} \times \boldsymbol{H}^i \end{pmatrix}, \tag{4.4}$$

where the unknowns are the surface electric and magnetic current densities

$$\boldsymbol{j}_s = \hat{\boldsymbol{n}} \times \boldsymbol{H}\,, \tag{4.5}$$

$$\boldsymbol{m}_s = -\hat{\boldsymbol{n}} \times \boldsymbol{E}\,, \tag{4.6}$$

and where $\eta_{\{0,1\}} = \sqrt{\mu_{\{0,1\}}/\epsilon_{\{0,1\}}}$ is the characteristic impedance of the exterior or interior medium.

Following the BEM, the surface Γ is discretized with a mesh of planar triangular elements. The unknown surface current densities are then discretized with the divergence-conforming Rao-Wilton-Glisson (RWG) basis functions [75] $\{\boldsymbol{f}_n,\, n = 1 \dots N_e\}$ as

$$\boldsymbol{j}_s \approx \sum_{n=1}^{N_e} j_n \boldsymbol{f}_n \,, \tag{4.7}$$

$$\boldsymbol{m}_s \approx \sum_{n=1}^{N_e} m_n \boldsymbol{f}_n \,, \tag{4.8}$$

where N_e is the number of edges in the mesh. Lastly, the system is tested with curl-conforming rotated RWG functions $\{\hat{\boldsymbol{n}} \times \boldsymbol{f}_n,\, n = 1 \dots N_e\}$ to produce the linear matrix system

$$\mathsf{Z}\mathsf{x} = \mathsf{b} \iff \begin{pmatrix} \mathsf{T}_{\text{upper}} & -\mathsf{K} \\ \mathsf{K} & \mathsf{T}_{\text{lower}} \end{pmatrix} \begin{pmatrix} \mathsf{j} \\ \mathsf{m} \end{pmatrix} = \begin{pmatrix} \mathsf{e} \\ \mathsf{h} \end{pmatrix} \,, \tag{4.9}$$

where the magnetic operator matrix appearing in the off-diagonal blocks is

$$\mathsf{K} = \mathsf{K}_{k_0} + \mathsf{K}_{k_1} \,, \tag{4.10}$$

and the diagonal electric operator blocks, which differ from each other due to the impedance factor, are

$$\begin{aligned} \mathsf{T}_{\text{upper}} &= \eta_0 \mathsf{T}_{k_0} + \eta_1 \mathsf{T}_{k_1} \\ &= -\mathrm{j}k_0\eta_0 \mathsf{T}_{A,k_0} + \frac{\eta_0}{\mathrm{j}k_0} \mathsf{T}_{\Phi,k_0} \\ &\quad - \mathrm{j}k_1\eta_1 \mathsf{T}_{A,k_1} + \frac{\eta_1}{\mathrm{j}k_1} \mathsf{T}_{\Phi,k_1} \,, \end{aligned} \tag{4.11}$$

$$\begin{aligned} \mathsf{T}_{\text{lower}} &= \frac{1}{\eta_0} \mathsf{T}_{k_0} + \frac{1}{\eta_1} \mathsf{T}_{k_1} \\ &= -\mathrm{j}\frac{k_0}{\eta_0} \mathsf{T}_{A,k_0} + \frac{1}{\mathrm{j}k_0\eta_0} \mathsf{T}_{\Phi,k_0} \\ &\quad - \mathrm{j}\frac{k_1}{\eta_1} \mathsf{T}_{A,k_1} + \frac{1}{\mathrm{j}k_1\eta_1} \mathsf{T}_{\Phi,k_1} \,. \end{aligned} \tag{4.12}$$

The matrices and vectors elements are obtained by calculating, for $m, n = 1 \dots N_e$,

$$(\mathbf{K}_k)_{mn} = \langle \hat{\boldsymbol{n}} \times \boldsymbol{f}_m, \boldsymbol{\mathcal{K}}_k(\boldsymbol{f}_n) \rangle \,, \tag{4.13}$$
$$(\mathbf{T}_k)_{mn} = \langle \hat{\boldsymbol{n}} \times \boldsymbol{f}_m, \boldsymbol{\mathcal{T}}_k(\boldsymbol{f}_n) \rangle \,, \tag{4.14}$$
$$(\mathbf{T}_{A,k})_{mn} = \langle \hat{\boldsymbol{n}} \times \boldsymbol{f}_m, \boldsymbol{\mathcal{T}}_{A,k}(\boldsymbol{f}_n) \rangle \,, \tag{4.15}$$
$$(\mathbf{T}_{\Phi,k})_{mn} = \langle \hat{\boldsymbol{n}} \times \boldsymbol{f}_m, \boldsymbol{\mathcal{T}}_{\Phi,k}(\boldsymbol{f}_n) \rangle \,, \tag{4.16}$$
$$(\mathbf{e})_m = \langle \hat{\boldsymbol{n}} \times \boldsymbol{f}_m, -\hat{\boldsymbol{n}} \times \boldsymbol{E}^i \rangle \,, \tag{4.17}$$
$$(\mathbf{h})_m = \langle \hat{\boldsymbol{n}} \times \boldsymbol{f}_m, -\hat{\boldsymbol{n}} \times \boldsymbol{H}^i \rangle \,, \tag{4.18}$$

where $\langle \boldsymbol{u}, \boldsymbol{v} \rangle = \iint_\Gamma \boldsymbol{u} \cdot \boldsymbol{v} \, \mathrm{d}\Gamma$, and the unknown solution vector elements are

$$(\mathbf{j})_n = j_n \,, \tag{4.19}$$
$$(\mathbf{m})_n = m_n \,. \tag{4.20}$$

For the sake of analysis, we will also use the Loop-Star transformation matrices that were introduced in Chapter 3. We recall the complete matrix for the change of basis, including the global loops,

$$\mathbf{A} = \begin{pmatrix} \mathbf{\Lambda} & \mathbf{H} & \mathbf{\Sigma} \end{pmatrix} \,, \tag{4.21}$$

where $\mathbf{\Lambda}$, $\mathbf{H}$, and $\mathbf{\Sigma}$ are the transformation matrices from the Loop, harmonic, and Star subspaces to the RWG space, respectively. Once linear independence of the columns is guaranteed for the Loop and Star matrices, the quasi-Helmholtz projectors are defined following eqs. (3.39) and (3.40). Additionally, we introduce the following dual quasi-Helmholtz projectors, defined as [5]

$$\mathbb{P}^{\mathbf{\Lambda}} = \mathbf{\Lambda} \left(\mathbf{\Lambda}^{\mathrm{T}} \mathbf{\Lambda} \right)^{+} \mathbf{\Lambda}^{\mathrm{T}} \,, \tag{4.22}$$
$$\mathbb{P}^{\mathbf{\Sigma H}} = \mathbf{I} - \mathbb{P}^{\mathbf{\Lambda}} \,. \tag{4.23}$$

These projectors are the equivalents of the primal ones for the dual barycentric mesh on which are defined the Buffa-Christiansen (BC) basis functions [20] $\{\boldsymbol{g}_n, \, n = 1 \dots N_e\}$. On the dual mesh, the properties of the Loop and Star functions are exchanged. Compared with the standard case, $\mathbb{P}^{\mathbf{\Lambda}}$ projects on the non-solenoidal subspace of the dual mesh, so that by complementarity, the harmonic subspace is implicitly included in $\mathbb{P}^{\mathbf{\Sigma H}}$, which projects on the entire solenoidal subspace. In order to apply these dual projectors, which are designed for the dual mesh, a mixed Gram matrix built from rotated RWG and BC functions is required. The Gram matrix elements are thus defined as

$$(\mathbf{G})_{mn} = \langle \hat{\boldsymbol{n}} \times \boldsymbol{f}_m, \, \boldsymbol{g}_n \rangle \,. \tag{4.24}$$

Multiplying the inverse of this Gram matrix before applying the dual projector is necessary to link the operators discretized with primal RWG functions to the

projectors acting on the dual BC functions. The construction of the BC functions is normally more expensive than the RWG functions. Fortunately, the entire solving process only requires the barycentric mesh refinement for this sole Gram matrix. Additionally, this matrix is sparse and can be computed analytically [5], and thus does not incur any excessive computational overhead.

4.3 Quasi-Static Eddy Current Model

The majority of existing BEM formulations for the simulation of eddy currents rely on the quasi-static approximation of Maxwell's equations [36, 78, 101]. Specifically, the displacement currents are neglected due to the relation

$$\omega\epsilon_0 \ll \sigma_1 \,, \tag{4.25}$$

which leads to low frequency-only models that are valid under eddy current conditions. In this section, we briefly present the so-called JKHE formulation found in [78], which we use as a reference in the numerical experiments. The problem setting is the same as described in the previous section, and we define the surface vectorial operators

$$(\boldsymbol{\mathcal{S}}_k \boldsymbol{f})(\boldsymbol{r}) = \iint_\Gamma G_k(\boldsymbol{r},\boldsymbol{r}')\, \boldsymbol{f}(\boldsymbol{r}')\, \mathrm{d}\boldsymbol{r}' \,, \tag{4.26}$$

$$(\boldsymbol{\mathcal{D}}_{v,k} \boldsymbol{f})(\boldsymbol{r}) = \iint_\Gamma \nabla G_k(\boldsymbol{r},\boldsymbol{r}') \times \boldsymbol{f}(\boldsymbol{r}')\, \mathrm{d}\boldsymbol{r}' \,, \tag{4.27}$$

$$(\boldsymbol{\mathcal{D}}_k\, g)(\boldsymbol{r}) = \iint_\Gamma \nabla' G_k(\boldsymbol{r},\boldsymbol{r}')\, g(\boldsymbol{r}')\, \mathrm{d}\boldsymbol{r}' \,. \tag{4.28}$$

The operator $\boldsymbol{\mathcal{D}}_k$ acts on scalar functions and the primed gradient indicates that the derivative applies to the primed variable $\boldsymbol{r}'$. Additionally, we define the following notations for any operator $\boldsymbol{\mathcal{A}}$,

$$\overset{\times}{\boldsymbol{\mathcal{A}}} = \hat{\boldsymbol{n}} \times \boldsymbol{\mathcal{A}} \,, \tag{4.29}$$

$$\dot{\boldsymbol{\mathcal{A}}} = \hat{\boldsymbol{n}} \cdot \boldsymbol{\mathcal{A}} \,. \tag{4.30}$$

Given the quasi-static approximation, the electric and magnetic equations on the surface Γ are written [78]

$$\begin{aligned} \frac{1}{2}\boldsymbol{E}(\boldsymbol{r}) = \mathrm{j}\omega\mu \iint_\Gamma \hat{\boldsymbol{n}}' \times \boldsymbol{H}(\boldsymbol{r}')\, G_k(\boldsymbol{r},\boldsymbol{r}')\, \mathrm{d}\boldsymbol{r}' \\ - \iint_\Gamma \hat{\boldsymbol{n}}' \times \boldsymbol{E}(\boldsymbol{r}') \times \nabla' G_k(\boldsymbol{r},\boldsymbol{r}')\, \mathrm{d}\boldsymbol{r}' - \iint_\Gamma \hat{\boldsymbol{n}}' \cdot \boldsymbol{E}(\boldsymbol{r}')\, \nabla' G_k(\boldsymbol{r},\boldsymbol{r}')\, \mathrm{d}\boldsymbol{r}' \,, \end{aligned} \tag{4.31}$$

$$\begin{aligned} \frac{1}{2}\boldsymbol{H}(\boldsymbol{r}) = -\sigma \iint_\Gamma \hat{\boldsymbol{n}}' \times \boldsymbol{E}(\boldsymbol{r}')\, G_k(\boldsymbol{r},\boldsymbol{r}')\, \mathrm{d}\boldsymbol{r}' \\ - \iint_\Gamma \hat{\boldsymbol{n}}' \times \boldsymbol{H}(\boldsymbol{r}') \times \nabla' G_k(\boldsymbol{r},\boldsymbol{r}')\, \mathrm{d}\boldsymbol{r}' - \iint_\Gamma \hat{\boldsymbol{n}}' \cdot \boldsymbol{H}(\boldsymbol{r}')\, \nabla' G_k(\boldsymbol{r},\boldsymbol{r}')\, \mathrm{d}\boldsymbol{r}' \,, \end{aligned} \tag{4.32}$$

where $\hat{\boldsymbol{n}}'$ is the unit normal at position $\boldsymbol{r}'$. From these two equations, several variations can be obtained by considering them in the exterior or interior media, but also by rotating or projecting the equations with the $\hat{\boldsymbol{n}}\times$ or $\hat{\boldsymbol{n}}\cdot$ operations. In the exterior medium, the incident fields $\boldsymbol{E}^i$ and $\boldsymbol{H}^i$ must also be taken into account on the right hand sides of (4.31) and (4.32), respectively.

As its name indicates, the JKHE formulation includes four unknown surface quantities, two of which are vectorial (current densities) and the other two scalar (normal component of fields), defined on Γ as

$$\boldsymbol{j}_s = \hat{\boldsymbol{n}} \times \boldsymbol{H}\,, \tag{4.33}$$
$$\boldsymbol{m}_s = -\hat{\boldsymbol{n}} \times \boldsymbol{E}\,, \tag{4.34}$$
$$E_n = \hat{\boldsymbol{n}} \cdot \boldsymbol{E}\,, \tag{4.35}$$
$$H_n = \mu_r\, \hat{\boldsymbol{n}} \cdot \boldsymbol{H}\,. \tag{4.36}$$

Therefore, we choose to discretize $\boldsymbol{j}_s$ and $\boldsymbol{m}_s$ with RWG basis functions $\boldsymbol{f}_n$, while E_n and H_n are decomposed with pulse basis functions g_n, which results in

$$\boldsymbol{j}_s \approx \sum_{n=1}^{N_e} j_n \boldsymbol{f}_n\,, \qquad \boldsymbol{m}_s \approx \sum_{n=1}^{N_e} m_n \boldsymbol{f}_n\,, \tag{4.37}$$
$$E_n \approx \sum_{n=1}^{N_c} e_n g_n\,, \qquad H_n \approx \sum_{n=1}^{N_c} h_n g_n\,, \tag{4.38}$$

where N_c indicates the number of triangle cells on the mesh. Equations (4.31) and (4.32) can then be rewritten as

$$\frac{1}{2}\boldsymbol{E}(\boldsymbol{r}) = \mathrm{j}\omega\mu\,(\boldsymbol{\mathcal{S}}_k\,\boldsymbol{j}_s)(\boldsymbol{r}) + (\boldsymbol{\mathcal{D}}_{v,k}\,\boldsymbol{m}_s)(\boldsymbol{r}) - (\boldsymbol{\mathcal{D}}_k\,E_n)(\boldsymbol{r})\,, \tag{4.39}$$
$$\frac{1}{2}\boldsymbol{H}(\boldsymbol{r}) = \sigma\,(\boldsymbol{\mathcal{S}}_k\,\boldsymbol{m}_s)(\boldsymbol{r}) - (\boldsymbol{\mathcal{D}}_{v,k}\,\boldsymbol{j}_s)(\boldsymbol{r}) - \frac{1}{\mu_r}\,(\boldsymbol{\mathcal{D}}_k\,H_n)(\boldsymbol{r})\,. \tag{4.40}$$

Furthermore, a few details need to be considered to properly derive the complete formulation:

- no incident fields are present inside the object;
- the conductivity of the vacuum is null;
- outside of the conductor, the normal $\hat{\boldsymbol{n}}$, pointing toward the exterior, must be inverted ($-\hat{\boldsymbol{n}}$).

The full set of equations is then obtained by selecting $\hat{\boldsymbol{n}}\times$ (4.40) in the interior medium, as well as $\hat{\boldsymbol{n}}\times$ (4.39), $\hat{\boldsymbol{n}}\cdot$ (4.39) and $\hat{\boldsymbol{n}}\cdot$ (4.40) in the air medium, resulting

in the JKHE matrix equation

$$\begin{pmatrix} \frac{\mathcal{I}}{2} + \overset{\times}{\boldsymbol{\mathcal{D}}}_{v,k_1} & -\sigma_1 \overset{\times}{\boldsymbol{\mathcal{S}}}_{k_1} & \mathbf{0} & \frac{1}{\mu_r}\overset{\times}{\boldsymbol{\mathcal{D}}}_{k_1} \\ -\mathrm{j}\omega\mu_0 \overset{\times}{\boldsymbol{\mathcal{S}}}_{k_0} & \frac{\mathcal{I}}{2} - \overset{\times}{\boldsymbol{\mathcal{D}}}_{v,k_0} & \overset{\times}{\boldsymbol{\mathcal{D}}}_{k_0} & \mathbf{0} \\ \mathrm{j}\omega\mu_0 \dot{\boldsymbol{\mathcal{S}}}_{k_0} & \dot{\boldsymbol{\mathcal{D}}}_{v,k_0} & \frac{\mathcal{I}}{2} - \dot{\boldsymbol{\mathcal{D}}}_{k_0} & 0 \\ -\dot{\boldsymbol{\mathcal{D}}}_{v,k_0} & 0 & 0 & \frac{\mathcal{I}}{2} - \dot{\boldsymbol{\mathcal{D}}}_{k_0} \end{pmatrix} \begin{pmatrix} \boldsymbol{j}_s \\ \boldsymbol{m}_s \\ E_n \\ H_n \end{pmatrix} = \begin{pmatrix} \mathbf{0} \\ -\hat{\boldsymbol{n}} \times \boldsymbol{E}^i \\ \hat{\boldsymbol{n}} \cdot \boldsymbol{E}^i \\ \hat{\boldsymbol{n}} \cdot \boldsymbol{H}^i \end{pmatrix} . \tag{4.41}$$

The system is then tested according to the nature of the operators. The first two equations are tested with RWG functions, while the last two equations are tested using pulse functions [10].

Since this model stems from a quasi-static approximation, it cannot be used at higher frequencies, although eddy currents still manifest inside conductors. This creates a limitation of the method as it becomes more and more inaccurate as the frequency increases, as demonstrated in [19].

4.4 Asymptotic Study of the PMCHWT Equation in the Eddy Current Regime

In this section, a comprehensive analysis of the asymptotic behavior of the PMCHWT equation in the context of eddy current modeling is carried out at low frequencies, as characterized by the conditions in (4.2). In particular, we consider the regime where the conductivity of the object σ_1 is fixed and $\omega \to 0$ (which is equivalent to $k \to 0$). A study for the case of constant skin depth and decreasing frequency, i.e. when the product $\sigma\omega$ is fixed and $\omega \to 0$, has been proposed in [16], albeit with a different method and objective. The third configuration, where the frequency is constant and $\sigma \to \infty$, is currently under study. The target regime of our study was also selected due to its relevancy for practical applications in which the material properties are unchanging. For instance, during manufacturing processes, parts of a given conductivity are scanned via non destructive testing by manipulating the skin depth through varying exciting frequencies.

For the purpose of analysis, we first apply a simple quasi-Helmholtz decomposition to the PMCHWT matrix equation using the Loop-Star transformation matrix A, which is written as

$$\mathsf{Z}_{\mathsf{LS}} = \begin{pmatrix} \mathsf{A}^{\mathrm{T}} & \mathbf{0} \\ \mathbf{0} & \mathsf{A}^{\mathrm{T}} \end{pmatrix} \begin{pmatrix} \mathsf{T}_{\mathrm{upper}} & -\mathsf{K} \\ \mathsf{K} & \mathsf{T}_{\mathrm{lower}} \end{pmatrix} \begin{pmatrix} \mathsf{A} & \mathbf{0} \\ \mathbf{0} & \mathsf{A} \end{pmatrix} . \tag{4.42}$$

Note that this approach only serves to facilitate the asymptotic study and must not be used in practice due to the ill-conditioning related to the mesh discretization introduced by the Loop and Star matrices [1]. With this technique, similarly to the

case of the low frequency EFIE presented in Chapter 3, the Loop, harmonic and Star components of each operator block of the PMCHWT system can be investigated one by one to better understand the source of the instabilities in eddy current conditions and to design an effective rescaling scheme. In the following, the Landau symbol $\mathcal{O}$ for the asymptotic scalings implies $\omega \to 0$.

4.4.1 Magnetic Operator

We start by inspecting the magnetic operator matrix $\mathbf{K}$ (4.10) which is shared by both off-diagonal blocks. In the discretization process, when solenoidal functions simultaneously appear as testing and source functions, the static part of the operator actually cancels out, with an exception if both are global loop functions, in which case only partial cancellations occur [23, 15]. Using the transformation matrices, this can be translated to the matrix relations

$$\mathbf{\Lambda}^{\mathrm{T}}\mathbf{K}_0\mathbf{\Lambda} = \mathbf{H}^{\mathrm{T}}\mathbf{K}_0\mathbf{\Lambda} = \mathbf{\Lambda}^{\mathrm{T}}\mathbf{K}_0\mathbf{H} = \mathbf{0}\,, \tag{4.43}$$

where $\mathbf{K}_0$ denotes the static part of $\mathbf{K}$ and is defined as

$$(\mathbf{K}_0)_{mn} = \langle \hat{\boldsymbol{n}} \times \boldsymbol{f}_m, \boldsymbol{\mathcal{K}}_0(\boldsymbol{f}_n)\rangle\,, \tag{4.44}$$

with

$$\begin{aligned}(\boldsymbol{\mathcal{K}}_0\boldsymbol{f})(\boldsymbol{r}) &= \hat{\boldsymbol{n}} \times \iint_\Gamma \nabla G_0(\boldsymbol{r},\boldsymbol{r}') \times \boldsymbol{f}(\boldsymbol{r}')\,\mathrm{d}\boldsymbol{r}' \\ &= \hat{\boldsymbol{n}} \times \iint_\Gamma \nabla\left(\frac{1}{4\pi R}\right) \times \boldsymbol{f}(\boldsymbol{r}')\,\mathrm{d}\boldsymbol{r}'\,.\end{aligned} \tag{4.45}$$

The kernel of the operator is then analyzed to isolate its static component as well as determine the asymptotic behavior of the dynamic part. Considering that $\omega \to 0$, the exponential $\mathrm{e}^{-\mathrm{j}kR}$ of the Green's function (2.43) can be developed with a Maclaurin expansion. Writing up to the first four terms, the series is approximated as

$$\begin{aligned}G_k(\boldsymbol{r},\boldsymbol{r}') &= \frac{1}{4\pi}\sum_{n=0}^{\infty}\frac{(-\mathrm{j}kR)^n}{n!R} \\ &\approx \frac{1}{4\pi}\left(\frac{1}{R} - \mathrm{j}k - \frac{k^2R}{2} + \frac{\mathrm{j}k^3R^2}{6} + \mathcal{O}(k^4)\right)\,.\end{aligned} \tag{4.46}$$

Since the second term is constant with respect to $\boldsymbol{r}$, the series for the gradient of the Green's function becomes

$$\begin{aligned}\nabla G_k(\boldsymbol{r},\boldsymbol{r}') &\approx \frac{1}{4\pi}\nabla\left(\frac{1}{R} - \mathrm{j}k - \frac{k^2R}{2} + \frac{\mathrm{j}k^3R^2}{6} + \mathcal{O}(k^4)\right) \\ &\approx \frac{1}{4\pi}\left(\nabla\left(\frac{1}{R}\right) - \frac{k^2}{2}\nabla R + \frac{\mathrm{j}k^3}{6}\nabla(R^2) + \mathcal{O}(k^4)\right)\,.\end{aligned} \tag{4.47}$$

The first term of the series is independent of the frequency and corresponds to the static part. This term therefore disappears when solenoidal functions are used according to the combinations described in (4.43).

Contrary to the pure dielectric setting, the wave numbers of the exterior and interior media have a different scaling in ω. Consequently, we write the kernels for the interior and exterior wave numbers

$$\nabla G_{k_0}(\boldsymbol{r},\boldsymbol{r}') \approx \frac{1}{4\pi}\left(\nabla\left(\frac{1}{R}\right) - \frac{\mu_0\epsilon_0\omega^2}{2}\nabla R + \mathrm{j}\,\frac{(\mu_0\epsilon_0)^{3/2}\omega^3}{6}\nabla(R^2) + \mathcal{O}(\omega^4)\right), \tag{4.48}$$

$$\nabla G_{k_1}(\boldsymbol{r},\boldsymbol{r}') \approx \frac{1}{4\pi}\left(\nabla\left(\frac{1}{R}\right) + \mathrm{j}\,\frac{\mu_1\sigma_1\omega}{2}\nabla R + (1-\mathrm{j})\frac{(\mu_1\sigma_1\omega)^{3/2}}{6\sqrt{2}}\nabla(R^2) + \mathcal{O}(\omega^2)\right). \tag{4.49}$$

Lastly, given that $\mathbf{K} = \mathbf{K}_{k_0} + \mathbf{K}_{k_1}$, the asymptotic scalings can be ascertained from the above gradient expansions by selecting the dominant real and imaginary terms in the sum, resulting in

$$\Re(\mathbf{K}) = \mathcal{O}(1)\,, \qquad \Im(\mathbf{K}) = \mathcal{O}(\omega)\,, \tag{4.50}$$

$$\Re(\mathbf{K}_d) = \mathcal{O}(\omega^{3/2})\,, \qquad \Im(\mathbf{K}_d) = \mathcal{O}(\omega)\,, \tag{4.51}$$

where $\mathbf{K}_d$ denotes the dynamic part of $\mathbf{K}$.

4.4.2 Electric Operator

In the case of the electric operator, the diagonal block matrices $\mathbf{T}_{\text{upper}}$ (4.11) and $\mathbf{T}_{\text{lower}}$ (4.12) only differ because of the impedance factor. For this reason, we rewrite the scalar factors using the definitions of k_0, k_1, η_0 and η_1 with respect to ω to obtain

$$k_0\eta_0 = \omega\mu_0 = \mathcal{O}(\omega)\,, \tag{4.52}$$

$$k_1\eta_1 = \omega\mu_1 = \mathcal{O}(\omega)\,, \tag{4.53}$$

$$k_0/\eta_0 = \omega\epsilon_0 = \mathcal{O}(\omega)\,, \tag{4.54}$$

$$k_1/\eta_1 = \omega\epsilon_1 = \omega\epsilon_0\epsilon_r' - \mathrm{j}\sigma_1 = \mathcal{O}(1)\,. \tag{4.55}$$

The frequency term in (4.55) is dominated by the constant conductivity term, which constitutes a major difference from the PMCHWT equation for lossless dielectrics [13] and creates an asymmetry between the upper and lower blocks.

Before examining the operator kernel, we also recall the following expression valid for any element of the scalar potential matrix, derived in Chapter 3,

$$(\mathbf{T}_{\Phi,k})_{mn} = -\iint_\Gamma \nabla\cdot\boldsymbol{f}_m(\boldsymbol{r}) \iint_\Gamma G_k(\boldsymbol{r},\boldsymbol{r}')\,\nabla'\cdot\boldsymbol{f}_n(\boldsymbol{r}')\,\mathrm{d}\boldsymbol{r}'\mathrm{d}\boldsymbol{r}\,. \tag{4.56}$$

This form is particularly useful to determine the asymptotic behavior for the quasi-Helmholtz components of the electric operator matrix. First, as inferred in Chapter 3, the scalar potential operator is canceled whenever a solenoidal function appears as the testing or source function. Since both Loop and global loop functions are divergence-free, we have the following relations

$$\mathbf{\Lambda}^{\mathrm{T}}\mathbf{T}_{\Phi,k} = \mathbf{T}_{\Phi,k}\mathbf{\Lambda} = \mathbf{H}^{\mathrm{T}}\mathbf{T}_{\Phi,k} = \mathbf{T}_{\Phi,k}\mathbf{H} = \mathbf{0}\,. \tag{4.57}$$

These cancellations of the scalar potential thus imply that the operator only remains in the Star-Star component of the decomposition, i.e. $\mathbf{\Sigma}^{\mathrm{T}}\mathbf{T}_{\Phi,k}\mathbf{\Sigma} \neq \mathbf{0}$.

Secondly, the vector and scalar potentials both share the same Green's function kernel, with the difference that the testing and source functions are either $\boldsymbol{f}$ for the vector potential, or $\nabla\cdot\boldsymbol{f}$ for the scalar potential. Writing out the expressions for the vector and scalar potentials with the Green's function as the kernel, we have

$$(\mathbf{T}_{A,k})_{mn} = \iint_\Gamma \boldsymbol{f}_m(\boldsymbol{r})\cdot\iint_\Gamma G_k(\boldsymbol{r},\boldsymbol{r}')\,\boldsymbol{f}_n(\boldsymbol{r}')\,\mathrm{d}\boldsymbol{r}'\mathrm{d}\boldsymbol{r}\,, \tag{4.58}$$

$$(\mathbf{T}_{\Phi,k})_{mn} = -\iint_\Gamma \nabla\cdot\boldsymbol{f}_m(\boldsymbol{r})\iint_\Gamma G_k(\boldsymbol{r},\boldsymbol{r}')\,\nabla'\cdot\boldsymbol{f}_n(\boldsymbol{r}')\,\mathrm{d}\boldsymbol{r}'\mathrm{d}\boldsymbol{r}\,. \tag{4.59}$$

Similarly to the magnetic operator, we develop the exponential of the Green's function with the Maclaurin series for the exterior and interior wave numbers

$$G_{k_0}(\boldsymbol{r},\boldsymbol{r}') \approx \frac{1}{4\pi}\left(\frac{1}{R} - \mathrm{j}k_0 - \frac{k_0^2}{2}R + \frac{\mathrm{j}k_0^3}{6}R^2 + \mathcal{O}(k_0^4)\right)\,, \tag{4.60}$$

$$G_{k_1}(\boldsymbol{r},\boldsymbol{r}') \approx \frac{1}{4\pi}\left(\frac{1}{R} - (1+\mathrm{j})\sqrt{\frac{\mu_1\sigma_1\omega}{2}} + \frac{\mathrm{j}\mu_1\sigma_1\omega}{2}R + \mathcal{O}(\omega^{3/2})\right)\,. \tag{4.61}$$

In both series expansions, the second term is independent of R. Moreover, as mentioned in Chapter 3, the integral of a Loop function on the surface considered is null. This is also true for global loop functions, as demonstrated in Appendix A. In other words, for a Loop or global loop function $\boldsymbol{l}$, we have

$$\iint_\Gamma \boldsymbol{l}(\boldsymbol{r})\,\mathrm{d}\boldsymbol{r} = \mathbf{0}\,. \tag{4.62}$$

This rule therefore applies for $(\mathbf{T}_{A,k})_{mn}$ when the source function $\boldsymbol{f}_n$ is solenoidal. In this case, the second term of the series above vanishes. Consequently, the real and imaginary asymptotic scalings of both operators inside and outside are

$$\Re((\mathbf{T}_{A,k_0})_{mn}) = \mathcal{O}(1)\,, \qquad \Im((\mathbf{T}_{A,k_0})_{mn}) = \begin{cases}\mathcal{O}(\omega^3) & \text{if } \boldsymbol{f}_n \text{ solenoidal}\\ \mathcal{O}(\omega) & \text{otherwise}\,,\end{cases} \tag{4.63}$$

$$\Re((\mathbf{T}_{\Phi,k_0})_{mn}) = \mathcal{O}(1)\,, \qquad \Im((\mathbf{T}_{\Phi,k_0})_{mn}) = \mathcal{O}(\omega)\,, \tag{4.64}$$

$$\Re((\mathbf{T}_{A,k_1})_{mn}) = \mathcal{O}(1)\,, \qquad \Im((\mathbf{T}_{A,k_1})_{mn}) = \begin{cases}\mathcal{O}(\omega) & \text{if } \boldsymbol{f}_n \text{ solenoidal}\\ \mathcal{O}(\omega^{1/2}) & \text{otherwise}\,,\end{cases} \tag{4.65}$$

$$\Re((\mathbf{T}_{\Phi,k_1})_{mn}) = \mathcal{O}(1)\,, \qquad \Im((\mathbf{T}_{\Phi,k_1})_{mn}) = \mathcal{O}(\omega^{1/2})\,. \tag{4.66}$$

Then, given the composition of the diagonal blocks $\mathbf{T}_{\text{upper}}$ (4.11) and $\mathbf{T}_{\text{lower}}$ (4.12), as well as the relations (4.52)–(4.55), the asymptotic scalings can be acquired for each quasi-Helmholtz component. The vector and scalar potential matrices are separated and considered for the upper and lower diagonal blocks as

$$\mathbf{T}_{A,\text{upper}} = -\,\mathrm{j}\omega\mu_0\mathbf{T}_{A,k_0} - \,\mathrm{j}\omega\mu_1\mathbf{T}_{A,k_1}\,, \tag{4.67}$$

$$\mathbf{T}_{\Phi,\text{upper}} \approx \frac{1}{\mathrm{j}\omega\epsilon_0}\mathbf{T}_{\Phi,k_0} + \frac{1}{\sigma_1}\mathbf{T}_{\Phi,k_1}\,, \tag{4.68}$$

$$\mathbf{T}_{A,\text{lower}} \approx -\,\mathrm{j}\omega\epsilon_0\mathbf{T}_{A,k_0} - \sigma_1\mathbf{T}_{A,k_1}\,, \tag{4.69}$$

$$\mathbf{T}_{\Phi,\text{lower}} = \frac{1}{\mathrm{j}\omega\mu_0}\mathbf{T}_{\Phi,k_0} + \frac{1}{\mathrm{j}\omega\mu_1}\mathbf{T}_{\Phi,k_1}\,, \tag{4.70}$$

where the approximations come from neglecting the non-dominant term of the complex permittivity at low frequency. Lastly, the final scalings can be derived from the above relations, resulting in

$$\Re((\mathbf{T}_{A,\text{upper}})_{mn}) = \begin{cases} \mathcal{O}(\omega^2) & \text{if } \boldsymbol{f}_n \text{ solenoidal} \\ \mathcal{O}(\omega^{3/2}) & \text{otherwise}\,, \end{cases} \tag{4.71}$$

$$\Re((\mathbf{T}_{\Phi,\text{upper}})_{mn}) = \mathcal{O}(1)\,, \tag{4.72}$$

$$\Re((\mathbf{T}_{A,\text{lower}})_{mn}) = \mathcal{O}(1)\,, \tag{4.73}$$

$$\Re((\mathbf{T}_{\Phi,\text{lower}})_{mn}) = \mathcal{O}(\omega^{-1/2})\,, \tag{4.74}$$

for the real parts and

$$\Im((\mathbf{T}_{A,\text{upper}})_{mn}) = \mathcal{O}(\omega)\,, \tag{4.75}$$

$$\Im((\mathbf{T}_{\Phi,\text{upper}})_{mn}) = \mathcal{O}(\omega^{-1})\,, \tag{4.76}$$

$$\Im((\mathbf{T}_{A,\text{lower}})_{mn}) = \begin{cases} \mathcal{O}(\omega) & \text{if } \boldsymbol{f}_n \text{ solenoidal} \\ \mathcal{O}(\omega^{1/2}) & \text{otherwise}\,, \end{cases} \tag{4.77}$$

$$\Im((\mathbf{T}_{\Phi,\text{lower}})_{mn}) = \mathcal{O}(\omega^{-1})\,, \tag{4.78}$$

for the imaginary parts.

4.4.3 Quasi-Helmholtz Decomposition of the PMCHWT Matrix

With the exhaustive analysis of the electric and magnetic operators, the asymptotic behavior of the entire matrix can now be summarized by writing the Loop-Star decomposed PMCHWT matrix in block form. Each of the four main blocks is divided as a submatrix of size 3×3. The Loop, harmonic and Star symbols on the left of the matrix correspond to the testing space, while the ones written above the

matrix indicate the source space. With this, the real and imaginary matrix scalings are, respectively,

$$\Re\left(\mathbf{Z_{LS}}\right) = \mathcal{O}\begin{array}{c} \\ \mathbf{\Lambda} \\ \mathbf{H} \\ \mathbf{\Sigma} \\ \mathbf{\Lambda} \\ \mathbf{H} \\ \mathbf{\Sigma} \end{array}\begin{array}{c} \begin{array}{ccc|ccc} \mathbf{\Lambda} & \mathbf{H} & \mathbf{\Sigma} & \mathbf{\Lambda} & \mathbf{H} & \mathbf{\Sigma} \end{array} \\ \left(\begin{array}{ccc|ccc} \omega^2 & \omega^2 & \omega^{3/2} & \omega^{3/2} & \omega^{3/2} & 1 \\ \omega^2 & \omega^2 & \omega^{3/2} & \omega^{3/2} & 1 & 1 \\ \omega^2 & \omega^2 & 1 & 1 & 1 & 1 \\ \hline \omega^{3/2} & \omega^{3/2} & 1 & 1 & 1 & 1 \\ \omega^{3/2} & 1 & 1 & 1 & 1 & 1 \\ 1 & 1 & 1 & 1 & 1 & \omega^{-1/2} \end{array}\right) \end{array}, \tag{4.79}$$

$$\Im\left(\mathbf{Z_{LS}}\right) = \mathcal{O}\begin{array}{c} \\ \mathbf{\Lambda} \\ \mathbf{H} \\ \mathbf{\Sigma} \\ \mathbf{\Lambda} \\ \mathbf{H} \\ \mathbf{\Sigma} \end{array}\begin{array}{c} \begin{array}{ccc|ccc} \mathbf{\Lambda} & \mathbf{H} & \mathbf{\Sigma} & \mathbf{\Lambda} & \mathbf{H} & \mathbf{\Sigma} \end{array} \\ \left(\begin{array}{ccc|ccc} \omega & \omega & \omega & \omega & \omega & \omega \\ \omega & \omega & \omega & \omega & \omega & \omega \\ \omega & \omega & \omega^{-1} & \omega & \omega & \omega \\ \hline \omega & \omega & \omega & \omega & \omega & \omega^{1/2} \\ \omega & \omega & \omega & \omega & \omega & \omega^{1/2} \\ \omega & \omega & \omega & \omega & \omega & \omega^{-1} \end{array}\right) \end{array}. \tag{4.80}$$

To identify the matrix breakdown, it is clearer and more convenient to write the asymptotic scalings independently of the distinction between real and imaginary parts, which results in

$$\mathbf{Z_{LS}} = \mathcal{O}\begin{array}{c} \\ \mathbf{\Lambda} \\ \mathbf{H} \\ \mathbf{\Sigma} \\ \mathbf{\Lambda} \\ \mathbf{H} \\ \mathbf{\Sigma} \end{array}\begin{array}{c} \begin{array}{ccc|ccc} \mathbf{\Lambda} & \mathbf{H} & \mathbf{\Sigma} & \mathbf{\Lambda} & \mathbf{H} & \mathbf{\Sigma} \end{array} \\ \left(\begin{array}{ccc|ccc} \omega & \omega & \omega & \omega & \omega & 1 \\ \omega & \omega & \omega & \omega & 1 & 1 \\ \omega & \omega & \omega^{-1} & 1 & 1 & 1 \\ \hline \omega & \omega & 1 & 1 & 1 & 1 \\ \omega & 1 & 1 & 1 & 1 & 1 \\ 1 & 1 & 1 & 1 & 1 & \omega^{-1} \end{array}\right) \end{array}. \tag{4.81}$$

Similar to the decomposition of the EFIE for PECs seen in Chapter 3, the diagonal Star-Star components grow unbounded and scale as $\mathcal{O}(\omega^{-1})$ due to the presence of the scalar potential term. Moreover, the poor behavior of the matrix is also due to the reciprocal scalings in ω. More precisely, in the low frequency limit, the application of the Gershgorin circle theorem reveals three groups of eigenvalue clusters:

- The third and sixth rows correspond to eigenvalues diverging to infinity;
- The first and second rows correspond to eigenvalues around zero;
- The fourth and fifth rows correspond to eigenvalues gathered inside constant disks.

The first and second categories are similar to the ones observed on the EFIE for PECs and dielectrics, although the eigenvalues for the second category remain around zero without necessarily converging to the origin. Despite not contributing to the matrix breakdown, the presence of the third category of eigenvalues invalidates the use of rescaling schemes proposed for pure dielectrics, hence the need to find a strategy adapted to lossy conductors.

4.4.4 Loss of Accuracy at Very Low Frequency

As described in Chapter 3, the low frequency analysis needs to account for potential partial losses in the solution as well, since eliminating the conditioning breakdown of the PMCHWT matrix does not necessarily guarantee an accurate solution. In particular, the computation of quantities of interest from the solution such as scattered fields may become impossible. In this context, we consider three types of frequently encountered excitations [73]:

- Plane wave excitation, e.g. fields radiated by a remote antenna;
- Inductive excitation, e.g. voltage feed within a circuit, with a global loop going through the excitation port;
- Capacitive excitation, counterpart of the inductive excitation, without a global loop passing through the excitation port.

In the case of plane waves, the current density solution is typically used to obtain the scattered electric far field, whereas for circuit simulations with inductive and capacitive excitations, the electric near field can be computed from the current solution, after which the volumic current inside the conductor is derived. Therefore, we need to identify which components of the solution are required to correctly obtain the desired fields for each type of excitation. This can be done with the following steps:

1. Obtain the asymptotic scalings of the right hand side $\mathbf{b}$.
2. Derive the asymptotic scalings of the inverse PMCHWT matrix $\mathbf{Z}^{-1}$.
3. Deduce the asymptotic scalings of the current density solution $\mathbf{x} = \mathbf{Z}^{-1}\mathbf{b}$.
4. From the expressions of the far or near fields, determine their scalings based on $\mathbf{x}$. The solution components that produce dominant scalings are then identified as the ones necessary for an accurate computation.

Right hand side

We start by determining the scalings of the quasi-Helmholtz decomposition of the right hand side excitations. For the plane wave, both electric and magnetic fields behave identically [13]. Expanding the exponential with the Maclaurin series, each right hand side element can be written as

$$\begin{aligned}(\mathbf{b})_m &= -\iint_\Gamma \hat{\boldsymbol{n}} \times \boldsymbol{f}_m(\boldsymbol{r}) \cdot \hat{\boldsymbol{n}} \times \boldsymbol{A}_0 \, \mathrm{e}^{-\mathrm{j}k_0 \hat{\boldsymbol{k}} \cdot \boldsymbol{r}} \, \mathrm{d}\boldsymbol{r} \\ &= -\iint_\Gamma \boldsymbol{f}_m(\boldsymbol{r}) \cdot \boldsymbol{A}_0 \, \mathrm{e}^{-\mathrm{j}k_0 \hat{\boldsymbol{k}} \cdot \boldsymbol{r}} \, \mathrm{d}\boldsymbol{r} \\ &\approx -\iint_\Gamma \boldsymbol{f}_m(\boldsymbol{r}) \cdot \boldsymbol{A}_0 \left(1 - \mathrm{j}k_0 \hat{\boldsymbol{k}} \cdot \boldsymbol{r} - \frac{k_0^2 (\hat{\boldsymbol{k}} \cdot \boldsymbol{r})^2}{2} + \mathcal{O}(k_0^3)\right) \mathrm{d}\boldsymbol{r} \,, \end{aligned} \tag{4.82}$$

where $\boldsymbol{A}_0$ is a constant vector characterizing the peak amplitude and polarization of the electric or magnetic field. Since the integral of solenoidal functions is null, the first term of the expansion vanishes when $\boldsymbol{f}_m$ is a Loop or global loop function. The scalings can thus be readily obtained from the expression above and are listed in the corresponding column in Table 4.1 for the electric and magnetic fields.

As for inductive and capacitive excitations, they are typically modeled with a voltage delta gap [73] or a magnetic frill around the feed point [33]. For this study, we examine the expressions of the fields created by a magnetic frill. The electric and magnetic fields are written, respectively, [85]

$$\boldsymbol{E}^i(\boldsymbol{r}) = -\int_{\text{frill}} \nabla G_{k_0}(\boldsymbol{r}, \boldsymbol{r}') \times \boldsymbol{m}(\boldsymbol{r}') \, \mathrm{d}\boldsymbol{r}' \,, \tag{4.83}$$

$$\begin{aligned}\boldsymbol{H}^i(\boldsymbol{r}) = &\frac{1}{\mathrm{j}\omega\eta_0^2} \nabla \int_{\text{frill}} G_{k_0}(\boldsymbol{r}, \boldsymbol{r}') \, \nabla' \cdot \boldsymbol{m}(\boldsymbol{r}') \, \mathrm{d}\boldsymbol{r}' \\ &+ \frac{k_0^2}{\mathrm{j}\omega\eta_0^2} \int_{\text{frill}} G_{k_0}(\boldsymbol{r}, \boldsymbol{r}') \, \boldsymbol{m}(\boldsymbol{r}') \, \mathrm{d}\boldsymbol{r}' \,, \end{aligned} \tag{4.84}$$

where $\boldsymbol{m}$ is the given magnetic current forming the frill. With a closer inspection of these expressions, we can recognize that $\boldsymbol{E}^i$ is defined with the magnetic operator $\boldsymbol{\mathcal{K}}_{k_0}$ (minus the cross product with the normal). Similarly, $\boldsymbol{H}^i$ is defined from the electric operator $\boldsymbol{\mathcal{T}}_{k_0}$, albeit with different factors. The analysis based on the series expansion of the kernel made previously can thus be reused, considering only the case of the exterior wave number. Additionally, on a multiply connected structure with handles, the source function $\boldsymbol{m}$ represents a poloidal loop surrounding the feed point. As a consequence, if the structure contains a toroidal loop passing through the frill, the problem is inductive and the static part of the Green's function in eq. (4.83) does not cancel out for the harmonic component. Otherwise, the problem is considered capacitive and the static part is removed [73, 15]. Lastly, the asymptotic scalings are summarized in Table 4.1 for each type of right hand side based on the above observations.

Table 4.1: Scalings of the real and imaginary parts of the excitation when $\omega \to 0$.

Right hand side $\mathcal{O}(\boldsymbol{b})$			
Component	Plane wave	Inductive	Capacitive
$\Re(\boldsymbol{E}^i_{\mathbf{\Lambda}}), \Im(\boldsymbol{E}^i_{\mathbf{\Lambda}})$	ω^2, ω	ω^2, ω^3	ω^2, ω^3
$\Re(\boldsymbol{E}^i_{\mathbf{H}}), \Im(\boldsymbol{E}^i_{\mathbf{H}})$	ω^2, ω	1, ω^3	ω^2, ω^3
$\Re(\boldsymbol{E}^i_{\mathbf{\Sigma}}), \Im(\boldsymbol{E}^i_{\mathbf{\Sigma}})$	1, ω	1, ω^3	1, ω^3
$\Re(\boldsymbol{H}^i_{\mathbf{\Lambda}}), \Im(\boldsymbol{H}^i_{\mathbf{\Lambda}})$	ω^2, ω	ω^4, ω	ω^4, ω
$\Re(\boldsymbol{H}^i_{\mathbf{H}}), \Im(\boldsymbol{H}^i_{\mathbf{H}})$	ω^2, ω	ω^4, ω	ω^4, ω
$\Re(\boldsymbol{H}^i_{\mathbf{\Sigma}}), \Im(\boldsymbol{H}^i_{\mathbf{\Sigma}})$	1, ω	ω^4, ω	ω^4, ω

Inverse matrix

Next, the asymptotic behavior of the inverse matrix is derived from the decomposition of the forward matrix $\mathbf{Z_{LS}}$ in eqs. (4.79) and (4.80). For example, with a recursive application of the block matrix inversion [49] on the block decomposition of $\mathbf{Z_{LS}}$, we obtain the real and imaginary scalings for the inverse,

$$\Re\left(\mathbf{Z}_{\mathbf{LS}}^{-1}\right) = \mathcal{O}\begin{array}{c} \\ \mathbf{\Lambda} \\ \mathbf{H} \\ \mathbf{\Sigma} \\ \mathbf{\Lambda} \\ \mathbf{H} \\ \mathbf{\Sigma} \end{array}\begin{array}{c} \begin{array}{ccc|ccc} \mathbf{\Lambda} & \mathbf{H} & \mathbf{\Sigma} & \mathbf{\Lambda} & \mathbf{H} & \mathbf{\Sigma} \end{array} \\ \left(\begin{array}{ccc|ccc} \omega^{-1/2} & 1 & \omega^{3/2} & 1 & 1 & 1 \\ 1 & 1 & \omega^2 & 1 & 1 & \omega^{3/2} \\ \omega^{3/2} & \omega^2 & \omega^2 & \omega^2 & \omega^2 & \omega^2 \\ \hline 1 & 1 & \omega^2 & 1 & \omega^{3/2} & \omega^{3/2} \\ 1 & 1 & \omega^2 & \omega^{3/2} & \omega^{3/2} & \omega^{3/2} \\ 1 & \omega^{3/2} & \omega^2 & \omega^{3/2} & \omega^{3/2} & \omega^{3/2} \end{array}\right) \end{array}, \tag{4.85}$$

$$\Im\left(\mathbf{Z}_{\mathbf{LS}}^{-1}\right) = \mathcal{O}\begin{array}{c} \\ \mathbf{\Lambda} \\ \mathbf{H} \\ \mathbf{\Sigma} \\ \mathbf{\Lambda} \\ \mathbf{H} \\ \mathbf{\Sigma} \end{array}\begin{array}{c} \begin{array}{ccc|ccc} \mathbf{\Lambda} & \mathbf{H} & \mathbf{\Sigma} & \mathbf{\Lambda} & \mathbf{H} & \mathbf{\Sigma} \end{array} \\ \left(\begin{array}{ccc|ccc} \omega^{-1} & \omega^{1/2} & \omega & \omega^{1/2} & \omega^{1/2} & \omega^{1/2} \\ \omega^{1/2} & \omega & \omega & \omega & \omega & \omega \\ \omega & \omega & \omega & \omega & \omega^{5/2} & \omega^{5/2} \\ \hline \omega^{1/2} & \omega & \omega & \omega & \omega & \omega \\ \omega^{1/2} & \omega & \omega^{5/2} & \omega & \omega & \omega \\ \omega^{1/2} & \omega & \omega^{5/2} & \omega & \omega & \omega \end{array}\right) \end{array}. \tag{4.86}$$

Table 4.2: Scalings of the real and imaginary parts of the surface current densities when $\omega \to 0$.

Surface current density $\mathcal{O}(\boldsymbol{x})$			
Component	Plane wave	Inductive	Capacitive
$\Re(\boldsymbol{j}_{\boldsymbol{\Lambda}}), \Im(\boldsymbol{j}_{\boldsymbol{\Lambda}})$	1, $\omega^{1/2}$	1, $\omega^{1/2}$	$\omega^{3/2}, \omega$
$\Re(\boldsymbol{j}_{\mathbf{H}}), \Im(\boldsymbol{j}_{\mathbf{H}})$	$\omega^{3/2}, \omega$	1, ω	ω^{2}, ω
$\Re(\boldsymbol{j}_{\boldsymbol{\Sigma}}), \Im(\boldsymbol{j}_{\boldsymbol{\Sigma}})$	ω^{2}, ω	ω^{2}, ω	ω^{2}, ω
$\Re(\boldsymbol{m}_{\boldsymbol{\Lambda}}), \Im(\boldsymbol{m}_{\boldsymbol{\Lambda}})$	$\omega^{3/2}, \omega$	1, ω	ω^{2}, ω
$\Re(\boldsymbol{m}_{\mathbf{H}}), \Im(\boldsymbol{m}_{\mathbf{H}})$	$\omega^{3/2}, \omega$	1, ω	$\omega^{2}, \omega^{5/2}$
$\Re(\boldsymbol{m}_{\boldsymbol{\Sigma}}), \Im(\boldsymbol{m}_{\boldsymbol{\Sigma}})$	$\omega^{3/2}, \omega$	$\omega^{3/2}, \omega$	$\omega^{2}, \omega^{5/2}$

Surface current density

Following the third step of the analysis, we can derive the scalings of the current density $\mathbf{x}$ from the decomposition of the inverse matrix and the different right hand sides. In particular, the decomposed solution is obtained with the operation $\mathbf{x}_{\mathbf{LS}} = \mathbf{Z}_{\mathbf{LS}}^{-1}\mathbf{b}_{\mathbf{LS}}$, where the subscript $_{\mathbf{LS}}$ denotes the Loop-Star decomposition. To illustrate the procedure, we detail the result, given a plane wave excitation, for the Loop component of the electric current density $\boldsymbol{j}_{\boldsymbol{\Lambda}}$, which corresponds to the first block of the vector $\mathbf{x}_{\mathbf{LS}}$. This is obtained by multiplying the first line of $\mathbf{Z}_{\mathbf{LS}}^{-1}$ (eqs. (4.85) and (4.86)) with the plane wave right hand side (first column of Table 4.1),

$$\begin{pmatrix} \omega^{-1/2} + \mathrm{j}\,\omega^{-1} \\ 1 + \mathrm{j}\,\omega^{1/2} \\ \omega^{3/2} + \mathrm{j}\,\omega \\ 1 + \mathrm{j}\,\omega^{1/2} \\ 1 + \mathrm{j}\,\omega^{1/2} \\ 1 + \mathrm{j}\,\omega^{1/2} \end{pmatrix}^{\mathrm{T}} \cdot \begin{pmatrix} \omega^{2} + \mathrm{j}\,\omega \\ \omega^{2} + \mathrm{j}\,\omega \\ 1 + \mathrm{j}\,\omega \\ \omega^{2} + \mathrm{j}\,\omega \\ \omega^{2} + \mathrm{j}\,\omega \\ 1 + \mathrm{j}\,\omega \end{pmatrix} = \mathcal{O}(1) + \mathrm{j}\,\mathcal{O}(\omega^{1/2})\,, \tag{4.87}$$

where the resulting real and imaginary asymptotic scalings are determined by the dominant terms of the product. This operation is repeated for all components of each type of excitation, which are compiled in Table 4.2. The dominant components are highlighted in red, with the electric and magnetic current densities evaluated separately.

Electric fields

For the last step, we examine the electric far and near fields computed from the electric and magnetic surface current densities. First, the far field approximation

is applied for the expression of the scattered field far from the object, expressed as [9]

$$\begin{aligned}\boldsymbol{E}(\boldsymbol{r}) \approx &- \frac{\mathrm{j}\omega\mu_0}{4\pi}\frac{\mathrm{e}^{-\mathrm{j}k_0 r}}{r}\iint_\Gamma \mathrm{e}^{\mathrm{j}k_0\boldsymbol{r}'\cdot\hat{\boldsymbol{r}}}\boldsymbol{j}_s(\boldsymbol{r}')\,\mathrm{d}\boldsymbol{r}' \\ &+ \hat{\boldsymbol{r}}\times\eta_0\left(\frac{\mathrm{j}\omega\epsilon_0}{4\pi}\frac{\mathrm{e}^{-\mathrm{j}k_0 r}}{r}\iint_\Gamma \mathrm{e}^{\mathrm{j}k_0\boldsymbol{r}'\cdot\hat{\boldsymbol{r}}}\boldsymbol{m}_s(\boldsymbol{r}')\,\mathrm{d}\boldsymbol{r}'\right), \end{aligned} \tag{4.88}$$

where $r = \|\boldsymbol{r}\|$ and $\hat{\boldsymbol{r}} = \boldsymbol{r}/\|\boldsymbol{r}\|$. Similarly to the asymptotic evaluations made until now, the exponential functions inside the integrals are expanded with the Maclaurin series as

$$\begin{aligned}\boldsymbol{E}(\boldsymbol{r}) \approx &- \frac{\mathrm{j}\omega\mu_0}{4\pi r}\iint_\Gamma\left(1+\mathrm{j}k_0\boldsymbol{r}'\cdot\hat{\boldsymbol{r}} - \frac{(k_0\boldsymbol{r}'\cdot\hat{\boldsymbol{r}})^2}{2} + \mathcal{O}(k_0^3)\right)\boldsymbol{j}_s(\boldsymbol{r}')\,\mathrm{d}\boldsymbol{r}' \\ &+ \hat{\boldsymbol{r}}\times\frac{\mathrm{j}k_0}{4\pi r}\iint_\Gamma\left(1+\mathrm{j}k_0\boldsymbol{r}'\cdot\hat{\boldsymbol{r}} - \frac{(k_0\boldsymbol{r}'\cdot\hat{\boldsymbol{r}})^2}{2} + \mathcal{O}(k_0^3)\right)\boldsymbol{m}_s(\boldsymbol{r}')\,\mathrm{d}\boldsymbol{r}', \end{aligned} \tag{4.89}$$

where the exponential functions outside of the integrals have been approximated with the first term of their series. When a solenoidal component of either of the current densities acts as the source, the first term of the corresponding integral disappears due to being constant with respect to $\boldsymbol{r}'$. The scalings of the current densities in the case of the plane wave are then inserted component by component to identify their individual contributions to the far field. As an example, we examine the asymptotic behavior of the field produced by the real and imaginary parts of $\boldsymbol{j}_{\boldsymbol{\Lambda}}$, which can be written, respectively,

$$-\frac{\mathrm{j}\omega\mu_0}{4\pi r}\iint_\Gamma\left(\mathrm{j}k_0\boldsymbol{r}'\cdot\hat{\boldsymbol{r}} - \frac{(k_0\boldsymbol{r}'\cdot\hat{\boldsymbol{r}})^2}{2} + \mathcal{O}(k_0^3)\right)\mathcal{O}(1)\,\mathrm{d}\boldsymbol{r}' = \mathcal{O}(\omega^2) + \mathrm{j}\,\mathcal{O}(\omega^3), \tag{4.90}$$

$$-\frac{\mathrm{j}\omega\mu_0}{4\pi r}\iint_\Gamma\left(\mathrm{j}k_0\boldsymbol{r}'\cdot\hat{\boldsymbol{r}} - \frac{(k_0\boldsymbol{r}'\cdot\hat{\boldsymbol{r}})^2}{2} + \mathcal{O}(k_0^3)\right)\mathcal{O}(\mathrm{j}\,\omega^{1/2})\,\mathrm{d}\boldsymbol{r}' = \mathcal{O}(\omega^{7/2}) + \mathrm{j}\,\mathcal{O}(\omega^{5/2}). \tag{4.91}$$

Each far field contribution obtained in this manner is gathered in Table 4.3 for the plane wave, where the notation has been reduced for clarity. More precisely, we write $(\Re,\Im)\,\boldsymbol{E}(\Re(\boldsymbol{j}_{\boldsymbol{\Lambda}})) = \Re(\boldsymbol{E}(\Re(\boldsymbol{j}_{\boldsymbol{\Lambda}})))$, $\Im(\boldsymbol{E}(\Re(\boldsymbol{j}_{\boldsymbol{\Lambda}})))$. The dominant scalings are highlighted in red to indicate the current density components that are required to correctly compute the field. For instance, $\Re(\boldsymbol{j}_{\boldsymbol{\Lambda}})$, $\Im(\boldsymbol{j}_{\boldsymbol{\Sigma}})$, and $\Im(\boldsymbol{m}_{\boldsymbol{\Sigma}})$ are necessary for a plane wave excitation.

For the inductive and capacitive cases, the electric near field inside the conductor is calculated from the complete expression of the electric field in free space (2.47),

written with the interior material quantities as

$$\begin{aligned}\boldsymbol{E}(\boldsymbol{r}) \approx \frac{1}{\sigma_1} \nabla \iint_\Gamma G_{k_1}(\boldsymbol{r},\boldsymbol{r}')\, \nabla' \cdot \boldsymbol{j}_s(\boldsymbol{r}')\, \mathrm{d}\boldsymbol{r}' \\ - \mathrm{j}\omega\mu_1 \iint_\Gamma G_{k_1}(\boldsymbol{r},\boldsymbol{r}')\, \boldsymbol{j}_s(\boldsymbol{r}')\, \mathrm{d}\boldsymbol{r}' \\ - \iint_\Gamma \nabla G_{k_1}(\boldsymbol{r},\boldsymbol{r}') \times \boldsymbol{m}_s(\boldsymbol{r}')\, \mathrm{d}\boldsymbol{r}' \,. \end{aligned} \tag{4.92}$$

The kernels are expanded once more for the purpose of extracting the dominant terms after the current density components are inserted. The series expansion is given by

$$\begin{aligned}\boldsymbol{E}(\boldsymbol{r}) \approx \frac{1}{4\pi\sigma_1} \iint_\Gamma \left(\nabla\left(\frac{1}{R}\right) + \frac{\mathrm{j}\mu_1\sigma_1\omega}{2}\nabla R + \mathcal{O}(\omega^{3/2})\right) \nabla' \cdot \boldsymbol{j}_s(\boldsymbol{r}')\, \mathrm{d}\boldsymbol{r}' \\ - \frac{\mathrm{j}\omega\mu_1}{4\pi} \iint_\Gamma \left(\frac{1}{R} - (1+\mathrm{j})\sqrt{\frac{\mu_1\sigma_1\omega}{2}} + \frac{\mathrm{j}\mu_1\sigma_1\omega}{2} R + \mathcal{O}(\omega^{3/2})\right) \boldsymbol{j}_s(\boldsymbol{r}')\, \mathrm{d}\boldsymbol{r}' \\ - \frac{1}{4\pi} \iint_\Gamma \left(\nabla\left(\frac{1}{R}\right) + \frac{\mathrm{j}\mu_1\sigma_1\omega}{2}\nabla R + \mathcal{O}(\omega^{3/2})\right) \times \boldsymbol{m}_s(\boldsymbol{r}')\, \mathrm{d}\boldsymbol{r}' \,. \end{aligned} \tag{4.93}$$

The resulting asymptotic scalings are found in Table 4.3, where the dominant elements have been highlighted in each column as for the plane wave.

Since the necessary current components for the computation of the electric field have been identified, we can now confirm whether or not there are critical losses for each excitation. By comparing the highlighted elements of Table 4.3 to the ones of Table 4.2, we can determine whether the low frequency current densities are sufficient on their own. On one hand, the near fields for both the inductive and capacitive right hand sides can be recovered with the default behavior of the current densities. As a result, these scenarios only require a cure for the matrix breakdown. Evidently, the preconditioning for the matrix must guarantee that the necessary components are still retrieved afterward. On the other hand, the far field for a plane wave excitation requires three components: $\Re(\boldsymbol{j}_{\boldsymbol{\Lambda}})$, $\Im(\boldsymbol{j}_{\boldsymbol{\Sigma}})$ and $\Im(\boldsymbol{m}_{\boldsymbol{\Sigma}})$. However, Table 4.2 reveals that the second one, $\Im(\boldsymbol{j}_{\boldsymbol{\Sigma}})$, is dominated and lost at low frequencies, which means that the far field cannot be computed accurately. Therefore, a good preconditioning strategy must not only produce a well-conditioned matrix, but also ensure that the solution retains the elements needed to derive the respective quantities of interest.

4.5 Stabilization Scheme with Quasi-Helmholtz Projectors

Now that the low frequency instabilities of the PMCHWT equation have been identified, a suitable approach must be proposed to both precondition the matrix

Table 4.3: Scalings of the real and imaginary parts of the electric far/near fields when $\omega \to 0$.

Far field (FF) or near field (NF) $\mathcal{O}(\boldsymbol{E})$			
Component	Plane wave (FF)	Inductive (NF)	Capacitive (NF)
$(\Re, \Im)\, \boldsymbol{E}(\Re(\boldsymbol{j_\Lambda}))$	ω^2, ω^3	ω^2, ω	$\omega^{7/2}$, $\omega^{5/2}$
$(\Re, \Im)\, \boldsymbol{E}(\Im(\boldsymbol{j_\Lambda}))$	$\omega^{7/2}$, $\omega^{5/2}$	$\omega^{3/2}$, $\omega^{5/2}$	ω^2, ω^3
$(\Re, \Im)\, \boldsymbol{E}(\Re(\boldsymbol{j_H}))$	$\omega^{7/2}, \omega^{9/2}$	ω^2, ω	ω^4, ω^3
$(\Re, \Im)\, \boldsymbol{E}(\Im(\boldsymbol{j_H}))$	ω^4, ω^3	ω^2, ω^3	ω^2, ω^3
$(\Re, \Im)\, \boldsymbol{E}(\Re(\boldsymbol{j_\Sigma}))$	ω^4, ω^3	ω^2, ω^3	ω^2, ω^3
$(\Re, \Im)\, \boldsymbol{E}(\Im(\boldsymbol{j_\Sigma}))$	ω^2, ω^3	ω^2, ω	ω^2, ω
$(\Re, \Im)\, \boldsymbol{E}(\Re(\boldsymbol{m_\Lambda}))$	$\omega^{7/2}, \omega^{9/2}$	1, ω	ω^2, ω^3
$(\Re, \Im)\, \boldsymbol{E}(\Im(\boldsymbol{m_\Lambda}))$	ω^4, ω^3	ω^2, ω	ω^2, ω
$(\Re, \Im)\, \boldsymbol{E}(\Re(\boldsymbol{m_H}))$	$\omega^{7/2}, \omega^{9/2}$	1, ω	ω^2, ω^3
$(\Re, \Im)\, \boldsymbol{E}(\Im(\boldsymbol{m_H}))$	ω^4, ω^3	ω^2, ω	$\omega^{7/2}, \omega^{5/2}$
$(\Re, \Im)\, \boldsymbol{E}(\Re(\boldsymbol{m_\Sigma}))$	$\omega^{7/2}, \omega^{5/2}$	$\omega^{3/2}, \omega^{5/2}$	ω^2, ω^3
$(\Re, \Im)\, \boldsymbol{E}(\Im(\boldsymbol{m_\Sigma}))$	ω^2, ω^3	ω^2, ω	$\omega^{7/2}, \omega^{5/2}$

and secure a correct solution. To this end, we define the following diagonal matrices,

$$\mathbf{L} = \operatorname{diag}\begin{pmatrix} a_L & b_L & c_L & d_L & e_L & f_L \end{pmatrix}, \tag{4.94}$$

$$\mathbf{R} = \operatorname{diag}\begin{pmatrix} a_R & b_R & c_R & d_R & e_R & f_R \end{pmatrix}, \tag{4.95}$$

that contain scalar rescaling coefficients to be selected according to the analysis of the previous section. The rescaling matrices are then multiplied on the left and right of the system matrix as follows

$$\mathbf{L}\mathbf{Z}_{\mathbf{LS}}\mathbf{R} = \mathcal{O}\begin{pmatrix} a_L a_R\,\omega & a_L b_R\,\omega & \dots & a_L f_R \\ b_L a_R\,\omega & \ddots & & \vdots \\ \vdots & & \ddots & \vdots \\ f_L a_R & \dots & \dots & f_L f_R\,\omega^{-1} \end{pmatrix}. \tag{4.96}$$

A naive and straightforward approach is to apply a simple diagonal preconditioning, similar to the EFIE for PECs, using

$$\mathbf{L} = \mathbf{R} = \operatorname{diag}\begin{pmatrix} \omega^{-1/2} & \omega^{-1/2} & \omega^{1/2} & 1 & 1 & \omega^{1/2} \end{pmatrix}, \tag{4.97}$$

to obtain constant scalings on the diagonal, which results in the decomposed matrix

$$\mathbf{LZ_{LS}R} = \mathcal{O}\begin{array}{c} \\ \mathbf{\Lambda} \\ \mathbf{H} \\ \mathbf{\Sigma} \\ \mathbf{\Lambda} \\ \mathbf{H} \\ \mathbf{\Sigma} \end{array}\begin{array}{c} \begin{array}{ccc} \mathbf{\Lambda} & \mathbf{H} & \mathbf{\Sigma} \end{array} \\ \left(\begin{array}{ccc|ccc} 1 & 1 & \omega & \omega^{1/2} & \omega^{1/2} & 1 \\ 1 & 1 & \omega & \omega^{1/2} & \omega^{-1/2} & 1 \\ \omega & \omega & 1 & \omega^{1/2} & \omega^{1/2} & \omega \\ \hline \omega^{1/2} & \omega^{1/2} & \omega^{1/2} & 1 & 1 & \omega^{1/2} \\ \omega^{1/2} & \omega^{-1/2} & \omega^{1/2} & 1 & 1 & \omega^{1/2} \\ 1 & 1 & \omega & \omega^{1/2} & \omega^{1/2} & 1 \end{array}\right) \end{array}\begin{array}{c} \\ \mathbf{\Lambda} \\ \mathbf{H} \\ \mathbf{\Sigma} \\ \mathbf{\Lambda} \\ \mathbf{H} \\ \mathbf{\Sigma} \end{array}. \tag{4.98}$$

However, as highlighted in the matrix, two elements of the off-diagonal blocks become unbounded at low frequency, therefore invalidating the use of a basic diagonal preconditioner. Instead, the rescaling coefficients must be chosen one by one to comply with the low frequency requirements.

In addition, to optimize the condition number, the decomposed matrix scalings in (4.81) are written with the corresponding scalar factors from the dominant operators as

$$\mathbf{Z_{LS}} = \mathcal{O}\begin{array}{c} \\ \mathbf{\Lambda} \\ \mathbf{H} \\ \mathbf{\Sigma} \\ \mathbf{\Lambda} \\ \mathbf{H} \\ \mathbf{\Sigma} \end{array}\begin{array}{c} \begin{array}{ccc} \mathbf{\Lambda} & \mathbf{H} & \mathbf{\Sigma} \end{array} \\ \left(\begin{array}{ccc|ccc} \omega\mu_0 & \omega\mu_0 & \omega\mu_0 & \omega & \omega & 1 \\ \omega\mu_0 & \omega\mu_0 & \omega\mu_0 & \omega & 1 & 1 \\ \omega\mu_0 & \omega\mu_0 & (\omega\epsilon_0)^{-1} & 1 & 1 & 1 \\ \hline \omega & \omega & 1 & \sigma_1 & \sigma_1 & \sigma_1 \\ \omega & 1 & 1 & \sigma_1 & \sigma_1 & \sigma_1 \\ 1 & 1 & 1 & \sigma_1 & \sigma_1 & (\omega\mu_0)^{-1} \end{array}\right) \end{array}\begin{array}{c} \\ \mathbf{\Lambda} \\ \mathbf{H} \\ \mathbf{\Sigma} \\ \mathbf{\Lambda} \\ \mathbf{H} \\ \mathbf{\Sigma} \end{array}. \tag{4.99}$$

We start by rewriting the Loop-Star decomposed equation along with the rescaling matrices as

$$\mathbf{LZ_{LS}Ry} = \mathbf{L}\begin{pmatrix} \mathbf{A}^{\mathrm{T}} & \mathbf{0} \\ \mathbf{0} & \mathbf{A}^{\mathrm{T}} \end{pmatrix}\mathbf{b}\,, \tag{4.100}$$

where $\mathbf{y}$ is the auxiliary solution such that

$$\mathbf{x} = \begin{pmatrix} \mathbf{A} & \mathbf{0} \\ \mathbf{0} & \mathbf{A} \end{pmatrix}\mathbf{Ry}\,. \tag{4.101}$$

From this relation, we can directly derive the asymptotic scalings for the auxiliary

solution obtained from the preconditioned equation as

$$\mathbf{y} = \mathbf{R}^{-1} \begin{pmatrix} \mathbf{A}^{-1} & \mathbf{0} \\ \mathbf{0} & \mathbf{A}^{-1} \end{pmatrix} \mathbf{x} = \mathcal{O} \begin{pmatrix} a_R^{-1} \boldsymbol{j}_{\mathbf{\Lambda}} \\ b_R^{-1} \boldsymbol{j}_{\mathbf{H}} \\ c_R^{-1} \boldsymbol{j}_{\mathbf{\Sigma}} \\ d_R^{-1} \boldsymbol{m}_{\mathbf{\Lambda}} \\ e_R^{-1} \boldsymbol{m}_{\mathbf{H}} \\ f_R^{-1} \boldsymbol{m}_{\mathbf{\Sigma}} \end{pmatrix}, \tag{4.102}$$

which will be used to determine whether the necessary current density components for each type of excitation are preserved or not. Regarding the removal of the matrix breakdown, the coefficients must be selected so as to eliminate the presence of unbounded elements without introducing null spaces caused by vanishing rows or columns. In summary, the rescaling coefficients will be chosen to simultaneously cure the matrix breakdown as well as recover the essential elements of the solution.

Referring to the original matrix (4.99), we first adjust the unbounded Star-Star blocks on the diagonal which scale as $\mathcal{O}(\omega^{-1})$ by fixing

$$c_L = c_R = (\omega \epsilon_0)^{1/2}, \tag{4.103}$$

$$f_L = f_R = (\omega \mu_0)^{1/2}. \tag{4.104}$$

Then, rewriting the decomposed matrix, we obtain

$$\mathbf{L}\mathbf{Z}_{\mathbf{LS}}\mathbf{R} = \mathcal{O} \begin{array}{c} \\ \mathbf{\Lambda} \\ \mathbf{H} \\ \mathbf{\Sigma} \\ \mathbf{\Lambda} \\ \mathbf{H} \\ \mathbf{\Sigma} \end{array} \begin{array}{c} \begin{array}{ccc} \mathbf{\Lambda} & \mathbf{H} & \mathbf{\Sigma} \end{array} \\ \left(\begin{array}{ccc|ccc} \omega & \omega & \omega^{3/2} & \omega & \omega & \omega^{1/2} \\ \omega & \omega & \omega^{3/2} & \omega & 1 & \omega^{1/2} \\ \omega^{3/2} & \omega^{3/2} & 1 & \omega^{1/2} & \omega^{1/2} & \omega \\ \hline \omega & \omega & \omega^{1/2} & 1 & 1 & \omega^{1/2} \\ \omega & 1 & \omega^{1/2} & 1 & 1 & \omega^{1/2} \\ \omega^{1/2} & \omega^{1/2} & \omega & \omega^{1/2} & \omega^{1/2} & 1 \end{array} \right) \end{array}, \tag{4.105}$$

where the factors μ_0, ϵ_0, and σ_1 have been omitted for readability. Although the unbounded elements have been corrected, the first row and first column induce a null space. Nevertheless, note that this operation also has the positive consequence of allowing the retrieval of $\Im(\boldsymbol{j}_{\mathbf{\Sigma}})$ for the plane wave excitation, which was previously lost at low frequencies. To delete the newly generated null space, we select the coefficients

$$a_L = a_R = (\omega \mu_0)^{-1/2}, \tag{4.106}$$

thus resulting in the matrix scalings

$$\mathbf{LZ_{LS}R} = \mathcal{O}\begin{array}{c} \\ \mathbf{\Lambda} \\ \mathbf{H} \\ \mathbf{\Sigma} \\ \mathbf{\Lambda} \\ \mathbf{H} \\ \mathbf{\Sigma} \end{array}\begin{array}{c} \begin{array}{ccc} \mathbf{\Lambda} & \mathbf{H} & \mathbf{\Sigma} \end{array} \\ \left(\begin{array}{ccc|ccc} 1 & \omega^{1/2} & \omega & \omega^{1/2} & \omega^{1/2} & 1 \\ \omega^{1/2} & \omega & \omega^{3/2} & \omega & 1 & \omega^{1/2} \\ \omega & \omega^{3/2} & 1 & \omega^{1/2} & \omega^{1/2} & \omega \\ \hline \omega^{1/2} & \omega & \omega^{1/2} & 1 & 1 & \omega^{1/2} \\ \omega^{1/2} & 1 & \omega^{1/2} & 1 & 1 & \omega^{1/2} \\ 1 & \omega^{1/2} & \omega & \omega^{1/2} & \omega^{1/2} & 1 \end{array}\right) \end{array}. \tag{4.107}$$

Next, we select the second coefficients left and right in order to optimize the second row and column,

$$b_L = b_R = (\omega\mu_0)^{-1/2}\,, \tag{4.108}$$

which now gives

$$\mathbf{LZ_{LS}R} = \mathcal{O}\begin{array}{c} \\ \mathbf{\Lambda} \\ \mathbf{H} \\ \mathbf{\Sigma} \\ \mathbf{\Lambda} \\ \mathbf{H} \\ \mathbf{\Sigma} \end{array}\begin{array}{c} \begin{array}{ccc} \mathbf{\Lambda} & \mathbf{H} & \mathbf{\Sigma} \end{array} \\ \left(\begin{array}{ccc|ccc} 1 & 1 & \omega & \omega^{1/2} & \omega^{1/2} & 1 \\ 1 & 1 & \omega & \omega^{1/2} & \omega^{-1/2} & 1 \\ \omega & \omega & 1 & \omega^{1/2} & \omega^{1/2} & \omega \\ \hline \omega^{1/2} & \omega^{1/2} & \omega^{1/2} & 1 & 1 & \omega^{1/2} \\ \omega^{1/2} & \omega^{-1/2} & \omega^{1/2} & 1 & 1 & \omega^{1/2} \\ 1 & 1 & \omega & \omega^{1/2} & \omega^{1/2} & 1 \end{array}\right) \end{array}. \tag{4.109}$$

To compensate for the introduced unbounded elements, we then define

$$e_L = (\omega\mu_0)^{1/2}\,, \tag{4.110}$$

$$e_R = (\omega/\sigma_1)^{1/2}\,, \tag{4.111}$$

where the choice of the factor for e_L is linked to the quasi-Helmholtz projectors and will be clarified afterward. The matrix scalings are then written as

$$\mathbf{LZ_{LS}R} = \mathcal{O}\begin{array}{c} \\ \mathbf{\Lambda} \\ \mathbf{H} \\ \mathbf{\Sigma} \\ \mathbf{\Lambda} \\ \mathbf{H} \\ \mathbf{\Sigma} \end{array}\begin{array}{c} \begin{array}{ccc} \mathbf{\Lambda} & \mathbf{H} & \mathbf{\Sigma} \end{array} \\ \left(\begin{array}{ccc|ccc} 1 & 1 & \omega & \omega^{1/2} & \omega & 1 \\ 1 & 1 & \omega & \omega^{1/2} & 1 & 1 \\ \omega & \omega & 1 & \omega^{1/2} & \omega & \omega \\ \hline \omega^{1/2} & \omega^{1/2} & \omega^{1/2} & 1 & \omega^{1/2} & \omega^{1/2} \\ \omega & 1 & \omega & \omega^{1/2} & \omega & \omega \\ 1 & 1 & \omega & \omega^{1/2} & \omega & 1 \end{array}\right) \end{array}. \tag{4.112}$$

Although the matrix appears stable, the auxiliary solution for the inductive excitation now scales as

$$\mathbf{y} = \mathcal{O}\begin{pmatrix} \omega^{1/2} + \mathrm{j}\,\omega \\ \omega^{1/2} + \mathrm{j}\,\omega^{3/2} \\ \omega^{3/2} + \mathrm{j}\,\omega^{1/2} \\ 1 + \mathrm{j}\,\omega \\ \omega^{-1/2} + \mathrm{j}\,\omega^{1/2} \\ \omega + \mathrm{j}\,\omega^{1/2} \end{pmatrix}, \tag{4.113}$$

thus indicating that the component $\Re(\boldsymbol{m}_{\mathbf{\Lambda}})$, required for the computation of the near field, is dominated and lost. As a consequence, we select the remaining two coefficients accordingly,

$$d_L = (\omega\sigma_1)^{-1/2}, \tag{4.114}$$

$$d_R = (\omega/\sigma_1)^{1/2}, \tag{4.115}$$

with d_L chosen so as to maintain the fourth diagonal block independent from the frequency. Summarizing, the final set of left and right coefficients is defined as

$$\begin{pmatrix} a_L \\ b_L \\ c_L \\ d_L \\ e_L \\ f_L \end{pmatrix} = \begin{pmatrix} (\omega\mu_0)^{-1/2} \\ (\omega\mu_0)^{-1/2} \\ (\omega\epsilon_0)^{1/2} \\ (\omega\sigma_1)^{-1/2} \\ (\omega\mu_0)^{1/2} \\ (\omega\mu_0)^{1/2} \end{pmatrix}, \quad \begin{pmatrix} a_R \\ b_R \\ c_R \\ d_R \\ e_R \\ f_R \end{pmatrix} = \begin{pmatrix} (\omega\mu_0)^{-1/2} \\ (\omega\mu_0)^{-1/2} \\ (\omega\epsilon_0)^{1/2} \\ (\omega/\sigma_1)^{1/2} \\ (\omega/\sigma_1)^{1/2} \\ (\omega\mu_0)^{1/2} \end{pmatrix}. \tag{4.116}$$

The associated preconditioned matrix is thus

$$\mathbf{L}\mathbf{Z}_{\mathbf{LS}}\mathbf{R} = \mathcal{O}\begin{array}{c} \\ \mathbf{\Lambda} \\ \mathbf{H} \\ \mathbf{\Sigma} \\ \mathbf{\Lambda} \\ \mathbf{H} \\ \mathbf{\Sigma} \end{array}\begin{array}{c} \begin{array}{ccc} \mathbf{\Lambda} & \mathbf{H} & \mathbf{\Sigma} \end{array} \\ \left(\begin{array}{ccc|ccc} 1 & 1 & \omega & \omega & \omega & 1 \\ 1 & 1 & \omega & \omega & 1 & 1 \\ \omega & \omega & 1 & \omega & \omega & \omega \\ \hline 1 & 1 & 1 & 1 & 1 & 1 \\ \omega & 1 & \omega & \omega & \omega & \omega \\ 1 & 1 & \omega & \omega & \omega & 1 \end{array}\right) \end{array}\begin{array}{c} \\ \mathbf{\Lambda} \\ \mathbf{H} \\ \mathbf{\Sigma} \\ \mathbf{\Lambda} \\ \mathbf{H} \\ \mathbf{\Sigma} \end{array}, \tag{4.117}$$

which is now free of conditioning breakdown. Furthermore, the asymptotic behavior of the auxiliary solution for all excitations is detailed in Table 4.4. The components that are effectively recovered at low frequencies are highlighted and include the necessary elements for the derivation of the far or near fields according to each type of right hand side.

Table 4.4: Scalings of the real and imaginary parts of the auxiliary solution when $\omega \to 0$.

Auxiliary solution $\mathcal{O}(\mathbf{y})$			
Component	Plane wave	Inductive	Capacitive
$\Re(\boldsymbol{j}_{\mathbf{\Lambda}}), \Im(\boldsymbol{j}_{\mathbf{\Lambda}})$	$\omega^{1/2}$, ω	$\omega^{1/2}$, ω	$\omega^2, \omega^{3/2}$
$\Re(\boldsymbol{j}_{\mathbf{H}}), \Im(\boldsymbol{j}_{\mathbf{H}})$	$\omega^2, \omega^{3/2}$	$\omega^{1/2}$, $\omega^{3/2}$	$\omega^{5/2}, \omega^{3/2}$
$\Re(\boldsymbol{j}_{\mathbf{\Sigma}}), \Im(\boldsymbol{j}_{\mathbf{\Sigma}})$	$\omega^{3/2}, \omega^{1/2}$	$\omega^{3/2}, \omega^{1/2}$	$\omega^{3/2}, \omega^{1/2}$
$\Re(\boldsymbol{m}_{\mathbf{\Lambda}}), \Im(\boldsymbol{m}_{\mathbf{\Lambda}})$	$\omega, \omega^{1/2}$	$\omega^{-1/2}$, $\omega^{1/2}$	$\omega^{3/2}, \omega^{1/2}$
$\Re(\boldsymbol{m}_{\mathbf{H}}), \Im(\boldsymbol{m}_{\mathbf{H}})$	$\omega, \omega^{1/2}$	$\omega^{-1/2}$, $\omega^{1/2}$	$\omega^{3/2}, \omega^2$
$\Re(\boldsymbol{m}_{\mathbf{\Sigma}}), \Im(\boldsymbol{m}_{\mathbf{\Sigma}})$	$\omega, \omega^{1/2}$	$\omega, \omega^{1/2}$	$\omega^{3/2}, \omega^2$

The selected coefficients in (4.116) must now be applied through the quasi-Helmholtz projectors. The four available projectors, $\mathbf{P}^{\mathbf{\Lambda H}}$, $\mathbf{P}^{\mathbf{\Sigma}}$, $\mathbb{P}^{\mathbf{\Lambda}}$, and $\mathbb{P}^{\mathbf{\Sigma H}}$, are defined such that the harmonic subspace is always paired with either the Loop or Star subspace. To comply with this property, the coefficients are associated accordingly, given

$$\left.\begin{aligned} a_L &= b_L \\ a_R &= b_R \\ d_R &= e_R \end{aligned}\right\} \Rightarrow \mathbf{P}^{\mathbf{\Lambda H}}, \tag{4.118}$$

$$e_L = f_L \;\} \Rightarrow \mathbb{P}^{\mathbf{\Sigma H}}. \tag{4.119}$$

Consequently, the complete projectors are defined on the left side, as

$$\mathbf{M}_1 = (\omega\mu_0)^{-1/2}\,\mathbf{P}^{\mathbf{\Lambda H}} + (\omega\epsilon_0)^{1/2}\,\mathbf{P}^{\mathbf{\Sigma}}, \tag{4.120}$$

$$\mathbb{M}_2 = (\omega\sigma_1)^{-1/2}\,\mathbb{P}^{\mathbf{\Lambda}} + (\omega\mu_0)^{1/2}\,\mathbb{P}^{\mathbf{\Sigma H}}, \tag{4.121}$$

and on the right side, as

$$\mathbf{M}_3 = (\omega\mu_0)^{-1/2}\,\mathbf{P}^{\mathbf{\Lambda H}} + (\omega\epsilon_0)^{1/2}\,\mathbf{P}^{\mathbf{\Sigma}}, \tag{4.122}$$

$$\mathbf{M}_4 = (\omega/\sigma_1)^{1/2}\,\mathbf{P}^{\mathbf{\Lambda H}} + (\omega\mu_0)^{1/2}\,\mathbf{P}^{\mathbf{\Sigma}}. \tag{4.123}$$

As explained in Section 4.2, the application of the dual projector $\mathbb{M}_2$ requires the use of the inverse of the mixed Gram matrix. Therefore, the full preconditioned formulation is finally expressed as [28]

$$\begin{pmatrix} \mathbf{M}_1 & \mathbf{0} \\ \mathbf{0} & \mathbb{M}_2\mathbf{G}^{-1} \end{pmatrix} \mathbf{Z} \begin{pmatrix} \mathbf{M}_3 & \mathbf{0} \\ \mathbf{0} & \mathbf{M}_4 \end{pmatrix} \mathbf{y} = \begin{pmatrix} \mathbf{M}_1 & \mathbf{0} \\ \mathbf{0} & \mathbb{M}_2\mathbf{G}^{-1} \end{pmatrix} \mathbf{b}, \tag{4.124}$$

where $\mathbf{y}$ is the auxiliary solution, from which we derive the current density solution

$$\mathbf{x} = \begin{pmatrix} \mathbf{M}_3 & \mathbf{0} \\ \mathbf{0} & \mathbf{M}_4 \end{pmatrix} \mathbf{y} \,. \tag{4.125}$$

4.6 Implementation Details

In this section, we specify several important details related to the implementation of the proposed formulation. Specifically, these remarks must be taken into account to ensure the accuracy and reliability of the scheme. First, when applying the quasi-Helmholtz projectors, the Loop-Star cancellations described in Section 4.4 must be enforced explicitly. Due to the limited machine precision, the terms that should disappear, such as the scalar potential with solenoidal functions, leave residual errors that can be amplified by the rescaling coefficients.

Specifically, in the case of the electric operator, we have the cancellations [5]

$$\mathbf{P}^{\mathbf{\Lambda H}}\mathbf{T}_{\Phi,k} = \mathbf{T}_{\Phi,k}\mathbf{P}^{\mathbf{\Lambda H}} = \mathbb{P}^{\mathbf{\Lambda}}\mathbf{G}^{-1}\mathbf{T}_{\Phi,k} = \mathbf{0} \,, \tag{4.126}$$

which lead to the following formulas for the diagonal blocks,

$$\begin{aligned} \mathbf{M}_1\mathbf{T}_{\text{upper}}\mathbf{M}_3 &= \mathbf{M}_1\mathbf{T}_{A,\text{upper}}\mathbf{M}_3 \\ &\quad + \omega\epsilon_0\, \mathbf{P}^{\mathbf{\Sigma}}\mathbf{T}_{\Phi,\text{upper}}\mathbf{P}^{\mathbf{\Sigma}} \,, \qquad (4.127) \\ \mathbb{M}_2\mathbf{T}_{\text{lower}}\mathbf{M}_4 &= \mathbb{M}_2\mathbf{T}_{A,\text{lower}}\mathbf{M}_4 \\ &\quad + \omega\mu_0\, \mathbb{P}^{\mathbf{\Sigma H}}\mathbf{G}^{-1}\mathbf{T}_{\Phi,\text{lower}}\mathbf{P}^{\mathbf{\Sigma}} \,. \qquad (4.128) \end{aligned}$$

As for the magnetic operator, we have the cancellation relation for the static component of $\mathbf{K}_k$ [13],

$$\mathbb{P}^{\mathbf{\Lambda}}\mathbf{G}^{-1}\mathbf{K}_0\mathbf{P}^{\mathbf{\Lambda H}} = \mathbf{0} \,. \tag{4.129}$$

This nullification applies to the lower left off-diagonal block, which must be computed explicitly as

$$\begin{aligned} \mathbb{M}_2\mathbf{K}\mathbf{M}_3 &= \mathbb{M}_2\mathbf{K}_d\mathbf{M}_3 \\ &\quad + (\epsilon_0/\sigma_1)^{1/2}\, \mathbb{P}^{\mathbf{\Lambda}}\mathbf{G}^{-1}\mathbf{K}_0\mathbf{P}^{\mathbf{\Sigma}} \\ &\quad + \omega(\mu_0\epsilon_0)^{1/2}\, \mathbb{P}^{\mathbf{\Sigma H}}\mathbf{G}^{-1}\mathbf{K}_0\mathbf{P}^{\mathbf{\Sigma}} \\ &\quad + \mathbb{P}^{\mathbf{\Sigma H}}\mathbf{G}^{-1}\mathbf{K}_0\mathbf{P}^{\mathbf{\Lambda H}} \,. \end{aligned} \tag{4.130}$$

Additionally, the dynamic part of the operator, $\mathbf{K}_d$, should be calculated by specifically excluding the static term of the kernel (4.47), rather than computing the difference $\mathbf{K}_k - \mathbf{K}_0$, to prevent numerical errors. For the upper right off-diagonal block, however, the use of primal projectors on both the left and right sides does not produce any particular cancellation. This is due to the fact that $\mathbf{H}^{\mathrm{T}}\mathbf{K}_0\mathbf{H}$ may be different from zero, which means that $\mathbf{P}^{\mathbf{\Lambda H}}\mathbf{K}_0\mathbf{P}^{\mathbf{\Lambda H}} \neq \mathbf{0}$.

Similarly, the static term for the plane wave right hand side must also be extracted from the exponential inside the integral when applying the projectors $\mathbf{P}^{\mathbf{\Lambda H}}$ and $\mathbb{P}^{\mathbf{\Lambda}}\mathbf{G}^{-1}$ [5]. In other words, the first term of the expansion in (4.82) is deliberately omitted during the computation in those cases [99]. As a result, the right hand side is written as

$$\begin{aligned}\begin{pmatrix}\mathbf{M}_1\mathbf{e}\\ \mathbb{M}_2\mathbf{G}^{-1}\mathbf{h}\end{pmatrix} &= \begin{pmatrix}(\omega\mu_0)^{-1/2}\,\mathbf{P}^{\mathbf{\Lambda H}} & \mathbf{0}\\ \mathbf{0} & (\omega\sigma_1)^{-1/2}\,\mathbb{P}^{\mathbf{\Lambda}}\mathbf{G}^{-1}\end{pmatrix}\begin{pmatrix}\mathbf{e}_{\text{ext}}\\ \mathbf{h}_{\text{ext}}\end{pmatrix}\\ &+ \begin{pmatrix}(\omega\epsilon_0)^{1/2}\,\mathbf{P}^{\mathbf{\Sigma}} & \mathbf{0}\\ \mathbf{0} & (\omega\mu_0)^{1/2}\,\mathbb{P}^{\mathbf{\Sigma H}}\mathbf{G}^{-1}\end{pmatrix}\begin{pmatrix}\mathbf{e}\\ \mathbf{h}\end{pmatrix},\end{aligned} \tag{4.131}$$

where the subscript $_{\text{ext}}$ refers to the extracted right hand side.

The next detail involves the Green's function defined for lossy media. More precisely, the complex wave number k_1 generates a complex and a real exponential. From the definition of k_1 in (4.3), we have

$$\begin{aligned}G_{k_1}(\boldsymbol{r},\boldsymbol{r}') &= \frac{\mathrm{e}^{-\mathrm{j}k_1 R}}{4\pi R}\\ &= \frac{1}{4\pi R}\,\mathrm{e}^{-\mathrm{j}\,(1-\mathrm{j})R/\delta}\\ &= \frac{1}{4\pi R}\,\mathrm{e}^{-\mathrm{j}\,R/\delta}\,\mathrm{e}^{-R/\delta}\,.\end{aligned} \tag{4.132}$$

The second exponential has a real negative exponent, and therefore decays more and more rapidly as the skin depth δ decreases, or equivalently, the exponential becomes smaller when the frequency and/or conductivity increase. Consequently, standard methods such as the Gaussian integration, which are frequently used to compute integral operators in the absence of singularities, are unable to capture the fast variation of the Green's function. Instead, specialized approaches for lossy media should be employed, such as those found in [74, 70, 95]. For elements calculated analytically, singularity extraction techniques [93, 44, 40] were used for the computation of the discretized matrix and right hand side, although alternative methods such as singularity cancellation [45, 89] may be employed.

While the presented preconditioned integral equation has been devised to be functional at low frequencies, the formulation is still entirely compatible with simulations at higher frequencies. In that case, the quasi-Helmholtz decomposition and rescaling procedure are not necessary. From the perspective of implementation, the rescaling coefficients can therefore simply be set to 1 [62], which is equivalent to using the original PMCHWT equation.

Furthermore, regarding time and memory performance, the proposed formulation can be accelerated with the use of fast solvers [30, 100], as described in Chapter 3, to attain a quasi-linear complexity as $\mathcal{O}(N \log N)$. This is made possible since the preconditioning approach built on the quasi-Helmholtz projectors can

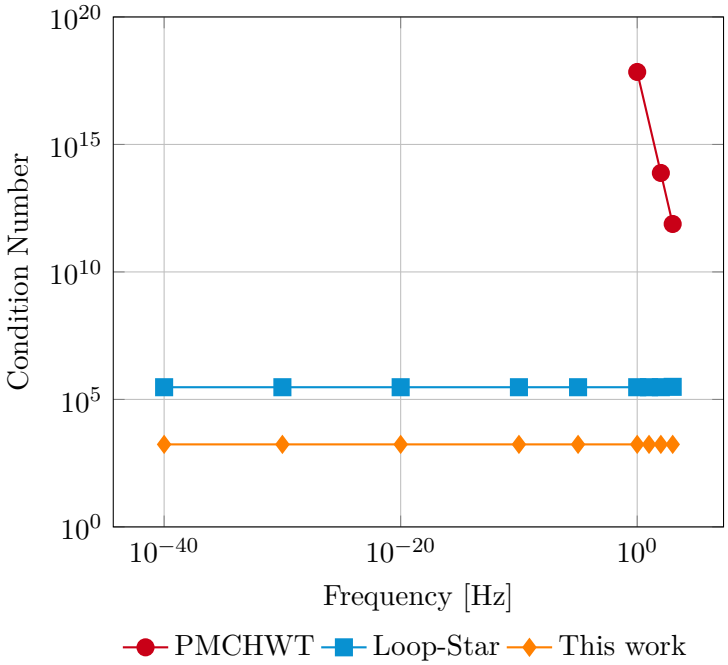

Figure 4.2: Sphere of radius 1 m with 1048 elements and $\sigma_1 = 10^3\,\mathrm{S\,m^{-1}}$: Condition number as a function of the frequency.

be applied in quasi-linear complexity with the help of multigrid preconditioners [65, 59]. As for the computational overhead introduced by the preparation and application of the preconditioner, it is effectively counterbalanced by the smaller number of iterations needed for the iterative solver to converge. As the frequency becomes lower and lower, the original PMCHWT formulation converges much more slowly, until it is ultimately unable to obtain a correct solution, whereas the proposed equation remains stable.

4.7 Numerical Results

A variety of experiments are presented to demonstrate the stability and accuracy of the proposed strategy. For each experiment, we have fixed the relative real permittivity and permeability as $\epsilon_r' = 1$ and $\mu_r = 1$. The results are obtained with plane wave excitations while the inductive and capacitive cases are currently under study.

4.7.1 Sphere

For the first configuration, we simulated a simply connected sphere of radius 1 m and conductivity $\sigma_1 = 10^3\,\mathrm{S\,m^{-1}}$. The structure was discretized with 1048

triangular elements, which result in 3144 unknowns. First, the condition numbers were computed for the standard PMCHWT equation, the Loop-Star method and the new formulation at different frequencies, illustrated in Figure 4.2. The original PMCHWT matrix clearly displays a fast degeneration of its condition number, whereas both the Loop-Star method and the new formulation remain stable until very low frequencies. However, the condition number achieved with the proposed formulation is significantly lower than that of the Loop-Star scheme, given that the quasi-Helmholtz projectors are well-conditioned.

Next, we compared the amplitude of the electric and magnetic current densities against those obtained with the eddy current specific formulation [78] introduced in Section 4.3, in the case of a plane wave excitation. The current densities have been computed at the centroids of a subset of elements located at a constant longitude, shown in Figure 4.3. For the magnetic current density, an analytical solution is also available for comparison [14, 64]. The Loop-Star method and the new formulation are in good agreement with both the analytical and eddy current solutions, whereas the PMCHWT equation completely fails to return correct results. This shows the capacity of the new strategy to maintain a satisfying accuracy until arbitrarily low frequencies.

The scattered far field for a plane wave excitation was then verified against a Mie solution, illustrated in Figure 4.4. As predicted by the theory, the PMCHWT method delivers a wrong result while the Loop-Star and new methods both match very well with the Mie solution.

Lastly, to confirm the validity of the new formulation at higher frequencies, we have simulated an exciting plane wave at 10 MHz. We have also selected a conductivity $\sigma_1 = 1\,\mathrm{mS\,m^{-1}}$ to further invalidate the eddy current conditions. The standard PMCHWT equation and the eddy current formulation have been tested along with the new method, using as reference an analytical solution based on vector spherical harmonics. The electric and magnetic current densities have been obtained and are illustrated in Figure 4.5. The results show that the original PMCHWT equation and the new method are in good agreement with the reference solution. The eddy current solution, however, is entirely erroneous due to the invalidity of the quasi-static approximation, thus demonstrating the capability of the new solver to maintain accuracy at higher frequencies where eddy current models cannot.

4.7.2 Torus

To verify the applicability of the new method to structures including handles, we simulated a torus with circular cross section, of major radius 1.5 m, minor radius 0.5 m and conductivity $\sigma_1 = 10^3\,\mathrm{S\,m^{-1}}$. The geometry was discretized with 1620 triangular elements, which leads to 4860 unknowns. The harmonic subspace contains two global loops. The condition numbers are first computed for the same

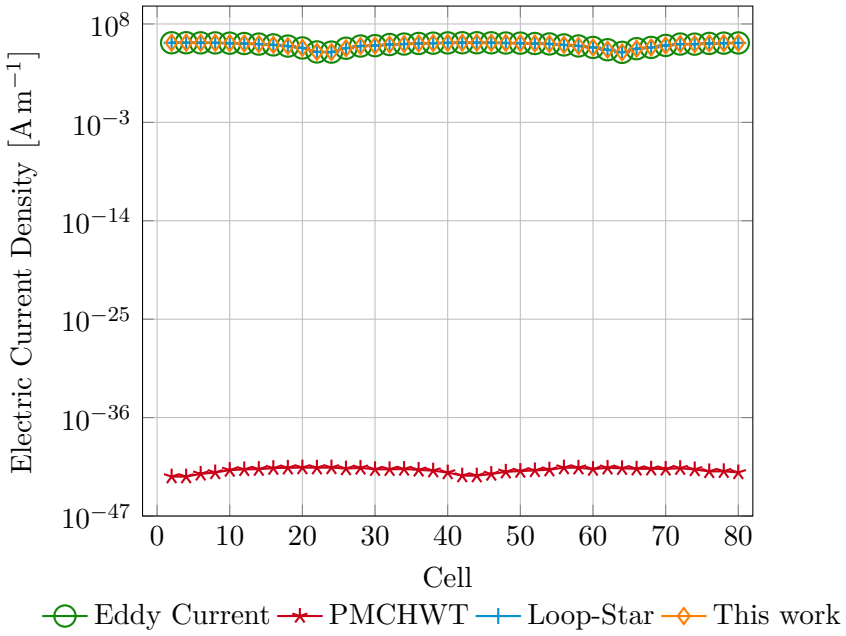

(a)

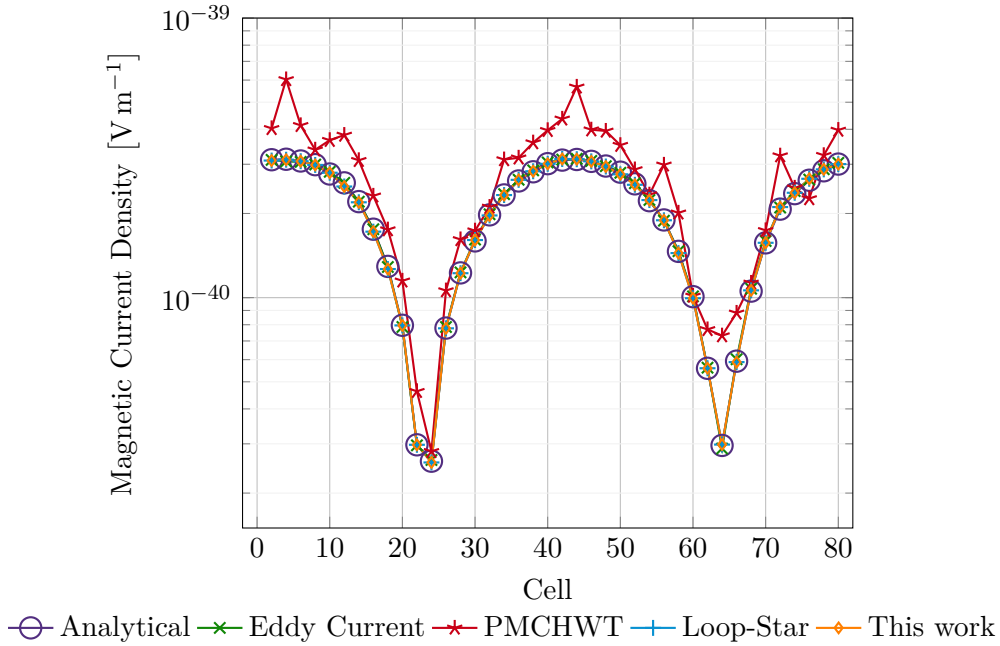

(b)

Figure 4.3: Sphere of radius 1 m with 1048 elements and $\sigma_1 = 10^3\,\mathrm{S\,m^{-1}}$: (a) Electric and (b) magnetic current density amplitude on elements of constant longitude given an exciting plane wave of frequency $f = 10^{-40}\,\mathrm{Hz}$ propagating along $-\hat{\boldsymbol{x}}$, polarized in the $-\hat{\boldsymbol{y}}$ direction and with $B_0 = 1\,\mathrm{T}$.

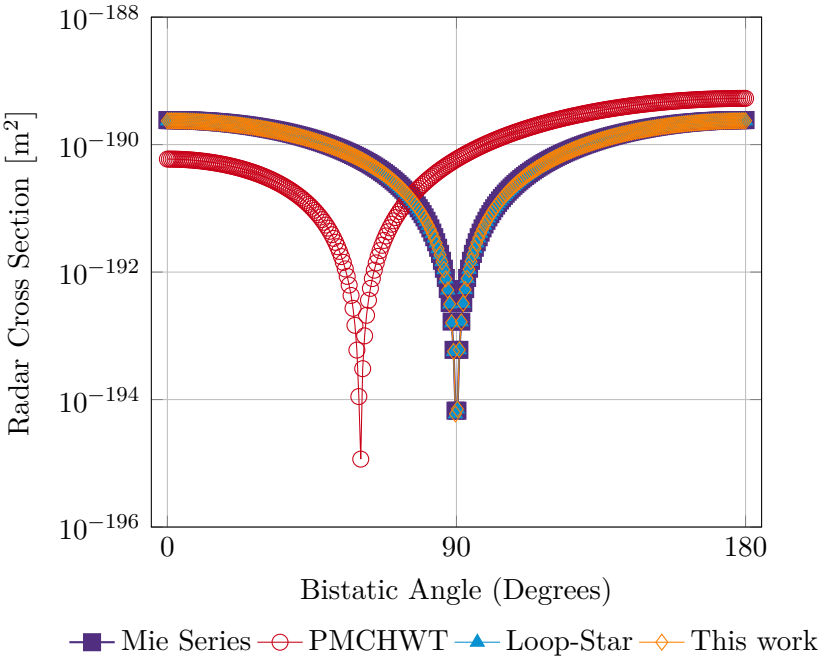

Figure 4.4: Sphere of radius 1 m with 1048 elements and $\sigma_1 = 10^3\,\mathrm{S\,m^{-1}}$: Radar cross section given an exciting plane wave of frequency $f = 10^{-40}\,\mathrm{Hz}$ propagating along $-\hat{\boldsymbol{z}}$, polarized in the $\hat{\boldsymbol{x}}$ direction and with $E_0 = 1\,\mathrm{V\,m^{-1}}$.

formulations as in the case of the sphere, and are illustrated in Figure 4.6. Similar results are observed for the torus, namely, that the conditioning of the PMCHWT equation rapidly saturates, while the Loop-Star and the new methods preserve a constant condition number, which is lower for the latter. Therefore, the presence of global loops is well supported by the new formulation in terms of conditioning.

The electric and magnetic current densities were next validated with an exciting plane wave, with the eddy current solver as a reference. The current densities were calculated around the handle of the torus, displayed in Figure 4.7. The graphs demonstrate matching results between the new method, the Loop-Star strategy and the eddy current formulation, while the original PMCHWT gives erroneous results.

The scattered far field was computed as well for a plane wave excitation. The radar cross section is plotted in Figure 4.8, showing that the new formulation agrees well with the Loop-Star method, and that the PMCHWT equation remains completely inaccurate.

We then simulated an inductive scenario using a circular ring of major radius 1.0 m, minor radius 0.2 m and conductivity $\sigma_1 = 10^3\,\mathrm{S\,m^{-1}}$. A plane wave corresponding to an injected voltage of 1 mV at 50 Hz is used as the excitation. The object was discretized with 1750 triangular elements, for 5250 unknowns. From circuit theory, we first obtain a resistance of $R = 0.05\,\Omega$ from the conductivity and

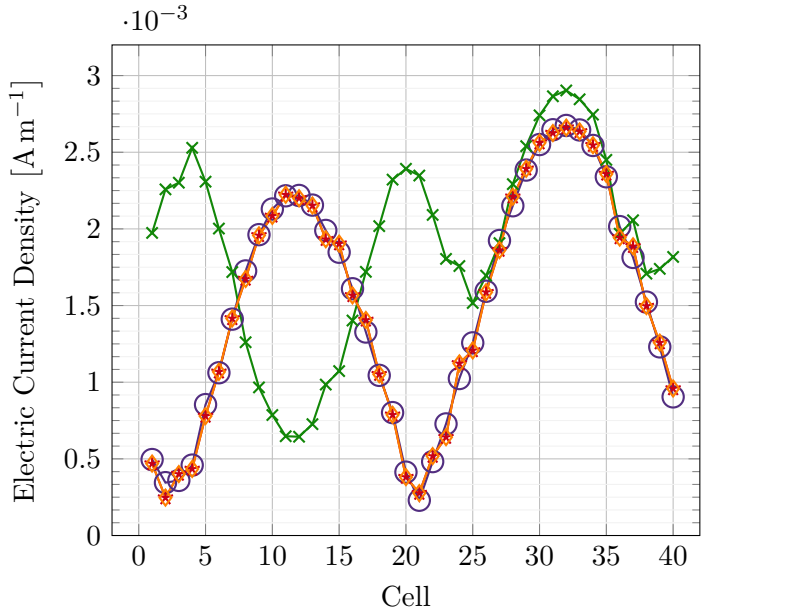

(a)

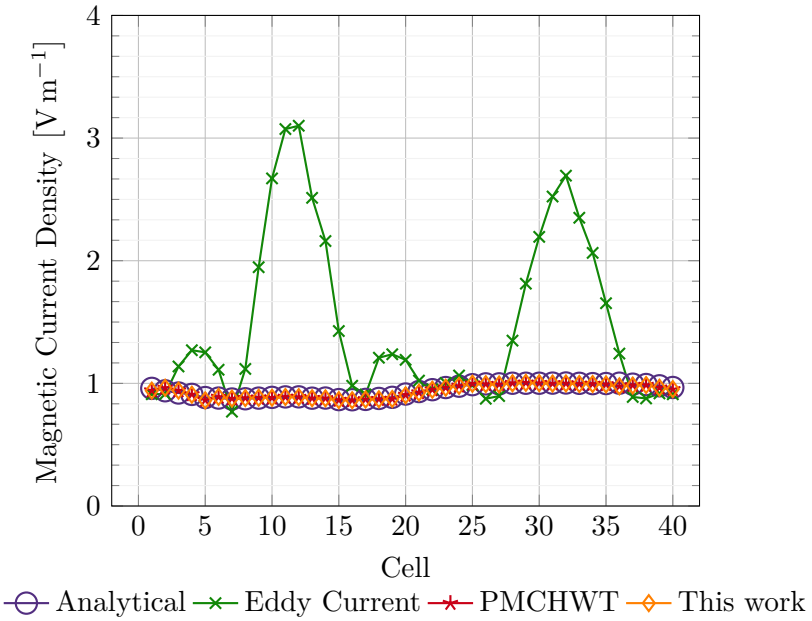

(b)

Figure 4.5: Sphere of radius 1 m with 1048 elements and $\sigma_1 = 1\,\mathrm{mS\,m^{-1}}$: (a) Electric and (b) magnetic current density amplitude on elements of constant longitude given an exciting plane wave of frequency $f = 10\,\mathrm{MHz}$ propagating along $-\hat{\boldsymbol{z}}$, polarized in the $\hat{\boldsymbol{x}}$ direction and with $E_0 = 1\,\mathrm{V\,m^{-1}}$.

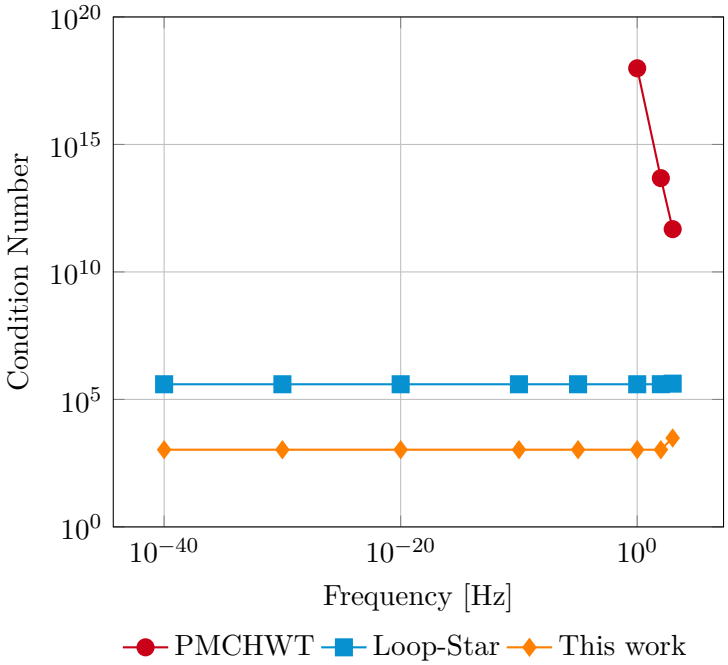

Figure 4.6: Torus of major and minor radii 1.5 m and 0.5 m with 1620 elements and $\sigma_1 = 10^3\,\mathrm{S\,m^{-1}}$: Condition number as a function of the frequency.

dimensions of the conductor, which gives a predicted current of $I = V/R = 20\,\mathrm{mA}$ after applying Ohm's law. This corresponds to an average eddy current density of $I/A = 0.159\,\mathrm{A\,m^{-2}}$, where A is the area of the cross section. The eddy currents obtained with the new formulation are constant along the axis of the ring (z-axis) and vary linearly on the cross section, as shown in Figure 4.9, with an average amplitude matching the above value. The eddy currents were also computed slightly below the surface and plotted in Figure 4.10, where they can be seen to flow around the ring.

4.7.3 Time Performance

The conditioning effect of the different formulations is directly reflected in the convergence rate of the solution obtained via iterative solvers, thus impacting the overall time performance. Figure 4.11 illustrates the decaying speed of the residual error from the Generalized Minimal Residual (GMRES) iterative method, using a plane wave excitation in the case of a torus. Our formulation successfully converged to the correct solution in 255 iterations. However, the Loop-Star method required 3410 iterations, whereas the original PMCHWT equation converged to an incorrect solution.

To further illustrate that the computational overhead introduced by the preconditioning process is compensated by the significantly lower number of iterations

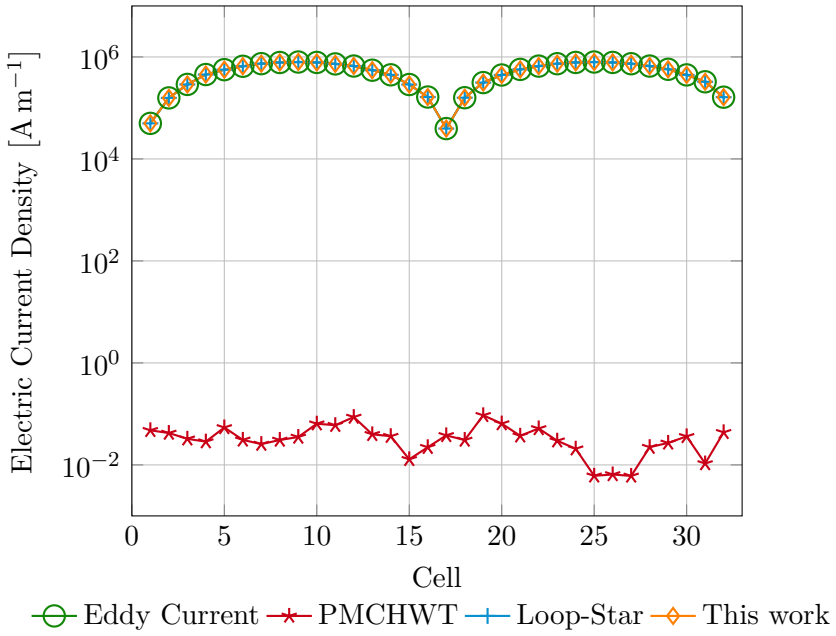

(a)

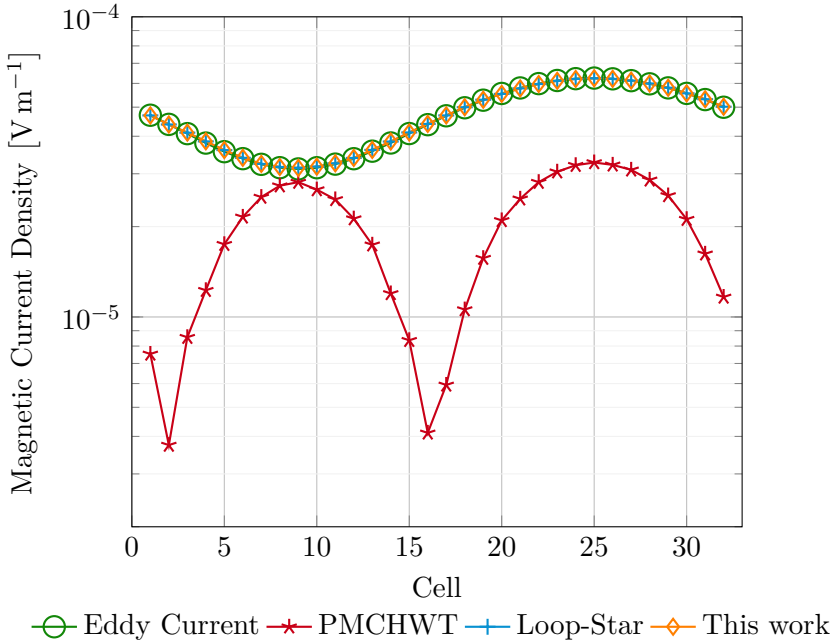

(b)

Figure 4.7: Torus of major and minor radii 1.5 m and 0.5 m with 1620 elements and $\sigma_1 = 10^3\,\mathrm{S\,m^{-1}}$: (a) Electric and (b) magnetic current density amplitude on elements around the handle given an exciting plane wave of frequency $f = 10^{-5}\,\mathrm{Hz}$ propagating along $-\hat{\boldsymbol{x}}$, polarized in the $-\hat{\boldsymbol{y}}$ direction and with $B_0 = 1\,\mathrm{T}$.

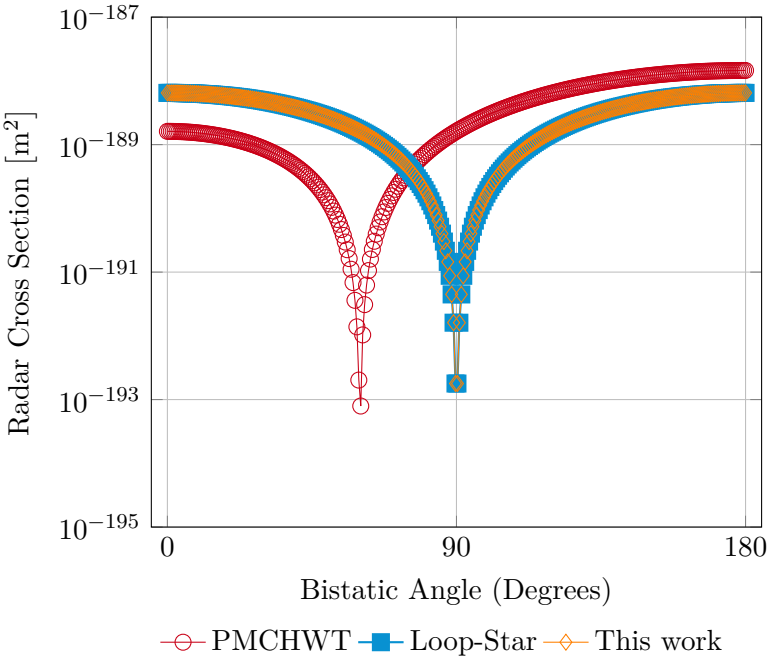

Figure 4.8: Torus of major and minor radii 1.5 m and 0.5 m with 1620 elements and $\sigma_1 = 10^3\,\mathrm{S\,m^{-1}}$: Radar cross section given an exciting plane wave of frequency $f = 10^{-40}\,\mathrm{Hz}$ propagating along $-\hat{\boldsymbol{z}}$, polarized in the $\hat{\boldsymbol{x}}$ direction and with $E_0 = 1\,\mathrm{V\,m^{-1}}$.

required for the new formulation, we have performed a comparative runtime experiment against the standard PMCHWT equation. The simulation was made for a sphere of radius 1 m, of conductivity $\sigma_1 = 1\,\mathrm{mS\,m^{-1}}$, and discretized with 2792 triangles, corresponding to 8376 unknowns. A plane wave oscillating at 5 MHz illuminates the object. The setup time (including preconditioning), overall computation time, and number of iterations for the GMRES method are given in Table 4.5. Note that the indicated timings have been obtained without a fast matrix vector product algorithm. As predicted, the difference in terms of total time is substantial compared to the additional time required to apply the preconditioning scheme, justifying the benefit of using the new formulation. Moreover, given that the setup time and condition number are independent from the type of excitation, similar

Table 4.5: Setup and computation time comparison between the PMCHWT equation and the new formulation.

Formulation	Setup time (s)	Nb. of iterations	Total time (s)
PMCHWT	59	1062	150
This work	68	276	98

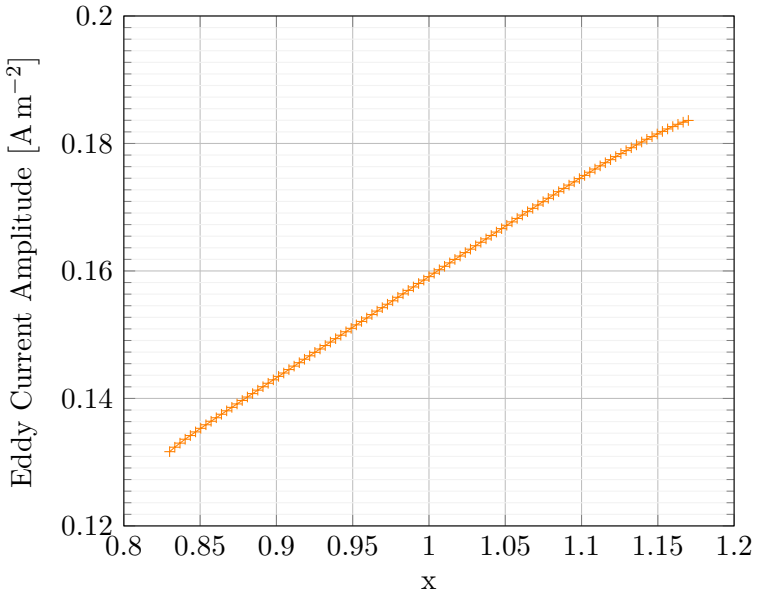

Figure 4.9: Torus of major and minor radii 1.0 m and 0.2 m with 1750 elements and $\sigma_1 = 10^3\,\mathrm{S\,m^{-1}}$: Eddy current inside the torus along the x-axis given a voltage excitation of value $V = 1\,\mathrm{mV}$ at frequency $f = 50\,\mathrm{Hz}$ (the torus is symmetrical about the z-axis).

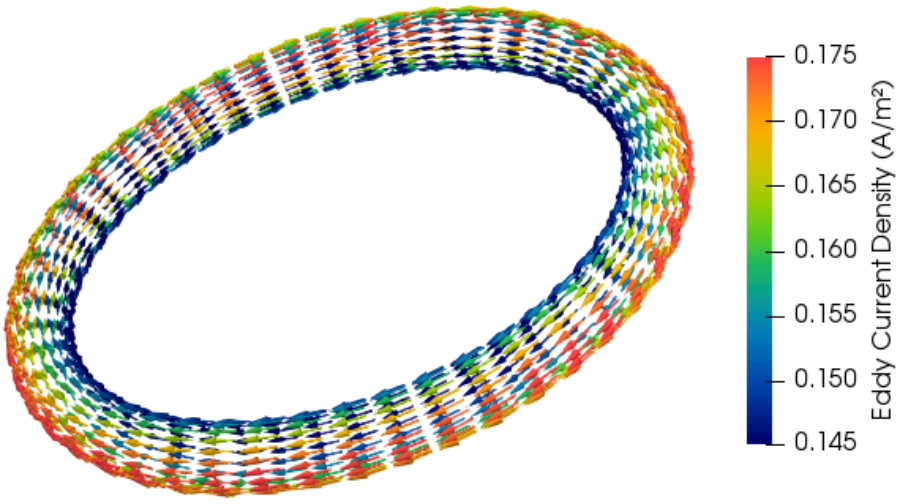

Figure 4.10: Torus of major and minor radii 1.0 m and 0.2 m with 1750 elements and $\sigma_1 = 10^3\,\mathrm{S\,m^{-1}}$: Eddy current density given a voltage excitation of value $V = 1\,\mathrm{mV}$ at frequency $f = 50\,\mathrm{Hz}$.

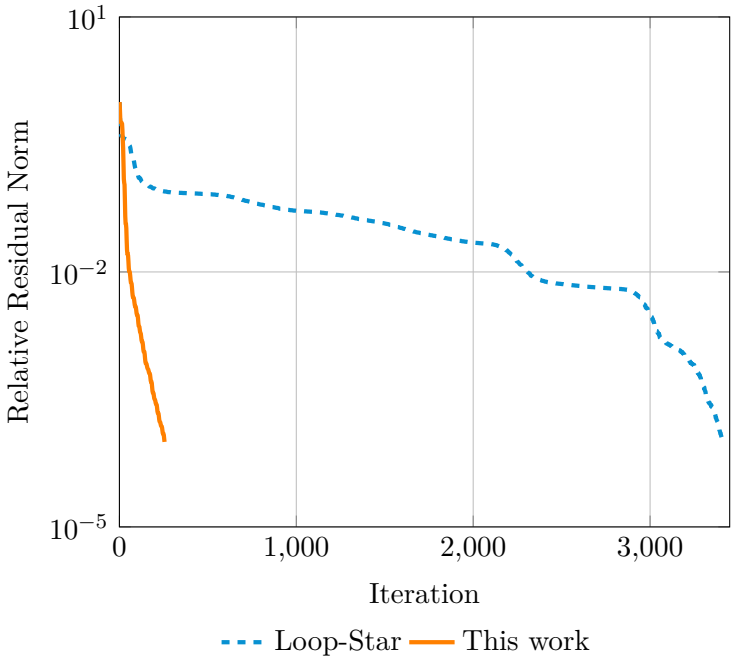

Figure 4.11: Torus of major and minor radii 1.5 m and 0.5 m with 1620 elements and $\sigma_1 = 10^3\,\mathrm{S\,m^{-1}}$: Convergence of the residual error for the Generalized Minimal Residual algorithm with relative tolerance 10^{-4} given an exciting plane wave of frequency $f = 10^{-40}\,\mathrm{Hz}$ propagating along $-\hat{\boldsymbol{z}}$, polarized in the $\hat{\boldsymbol{x}}$ direction and with $E_0 = 1\,\mathrm{V\,m^{-1}}$.

results are expected for the inductive and capacitive cases.

4.7.4 Jet Engine Shell

In the last experiment, we simulated a plane wave illuminating the outer shell of a jet engine with an average aluminum conductivity $\sigma_1 = 2 \times 10^7\,\mathrm{S\,m^{-1}}$ to confirm the applicability of our scheme to a non canonical example. The mesh was made of 9196 elements, corresponding to 27 588 unknowns. The electric current density was computed on the surface of the object, illustrated in Figure 4.12. Using the GMRES iterative solver, the Loop-Star PMCHWT method and the new formulation both reached the same solution, in 18 317 and 3241 iterations, respectively, confirming again the improved performance of our scheme.

4.8 Conclusion

In this chapter, a new boundary element method employing primal and dual quasi-Helmholtz projectors for the simulation of eddy current scenarios has been

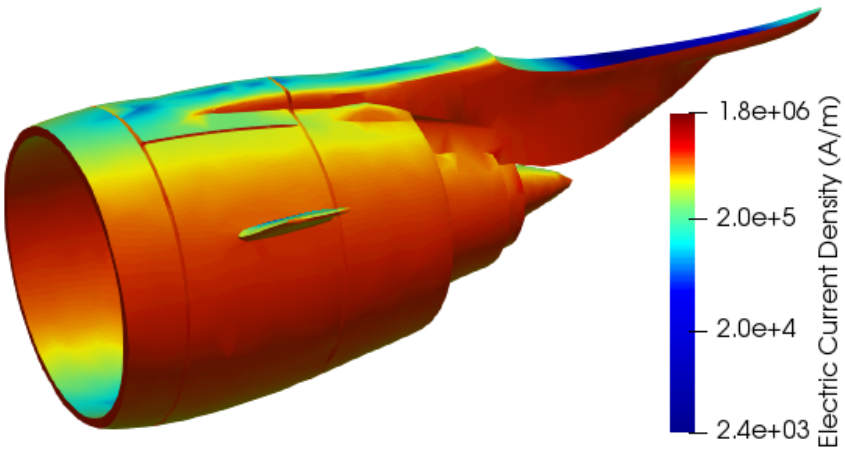

Figure 4.12: Jet engine outer shell of length 0.9 m with 9196 elements and $\sigma_1 = 2 \times 10^7\,\mathrm{S\,m^{-1}}$: Electric current density norm given an exciting plane wave of frequency $f = 10^{-40}\,\mathrm{Hz}$ propagating along $-\hat{\boldsymbol{z}}$, polarized in the $\hat{\boldsymbol{x}}$ direction and with $E_0 = 1\,\mathrm{V\,m^{-1}}$.

presented. The formulation was designed to offer several beneficial and attractive features:

- No conditioning breakdown: The new integral equation is free of condition number breakdown and all components of the solution that are necessary to derive relevant quantities are also assured for very low frequencies.
- Full-wave formulation: Unlike eddy current models limited to low frequencies and the original PMCHWT equation unadapted for them, the proposed strategy can transition between high and low frequencies with ease.
- Quasi-linear complexity: The construction and application cost of the quasi-Helmholtz projectors is well suited for use in conjunction with fast solvers.
- Support for multiply connected structures: Geometries containing handles are automatically supported without additional computational overhead.

The reliability and accuracy of the results obtained with the proposed method have been confirmed through different canonical and realistic examples.

While this chapter focuses on low frequencies where the breakdown occurs, the new method proves particularly advantageous in the mid frequency range where neither the quasi-static approximation nor standard equations are usable. The proposed formulation could be integrated into existing simulation software for the computer-aided design of various devices, such as antennas, circuits, and so on, operating in wide frequency ranges. Further possible improvements, including ongoing efforts, are suggested in Chapter 6.

Chapter 5

High Frequency Preconditioning Strategy Based on Spectral Analysis

In this chapter, we introduce a well-conditioned and resonance-free formulation for high frequency simulations. The electric operator suffers from a growing condition number when the frequency increases, and internal resonances are also present for both electric and magnetic equations when the structure is closed. We investigate the properties of these integral equations to determine the nature of the breakdown and other specific issues encountered at high frequencies. A spectral study of the operators is presented in two dimensions for the case of the infinite cylinder. A new resonance-free and stable formulation for high frequencies is then proposed as a result of that analysis. Part of this chapter has been published in the conference publication [26].

5.1 Introduction

The high frequency regime is characterized by a small wavelength compared to the size of the object under study. Typical high frequency scenarios include for example antenna radiation and waveguide propagation, which are greatly relevant and widespread applications. In practice, for simulations, the regime is defined by the product kh being constant while $k \to \infty$, where k is the wave number and h is the average edge length of the mesh discretization. In other words, the level of discretization is maintained in terms of wavelengths, which is imposed by the Nyquist-Shannon sampling theorem.

At very high frequencies, specific methods such as physical or geometrical optics [55, 69] can be applied due to the behavior of electromagnetic waves in those conditions. Nonetheless, these approaches present some limitations, such as the inability

to properly take into account the effect of sharp edges. On the other hand, full-wave integral equations such as the EFIE for Perfect Electric Conductors (PEC) are also valid at high frequencies, but unfortunately experience conditioning issues [91]. In addition, for closed structures, internal resonances may also appear and can produce non physical solutions. A few solutions to the high frequency ill-conditioning have been proposed in literature [2, 17, 34].

In this chapter, we propose an alternative new integral equation formulation that is well-conditioned in the high frequency, but also dense discretization regimes, and suppresses internal resonances. An analysis based on the study of the singular value spectrum of various operators for the infinite cylinder is detailed to highlight the different issues encountered at high frequencies.

The layout of this chapter is as follows. The integral operators originally presented in Chapter 2 are first reintroduced in Section 5.2 for the 2D case, along with the associated discretization strategy. Next, the operators are examined individually in Section 5.3 through a spectral analysis to uncover the sources of ill-conditioning specific to each of them. Section 5.4 then presents a few combination strategies to remove some of the causes for the bad conditioning. The observations made from those different approaches thus lead to the proposition of the new formulation built with the Helmholtz operator in Section 5.5. Lastly, concluding remarks are given in Section 5.6.

5.2 Integral Operators in Two Dimensions

5.2.1 Integral Equations

Consider a PEC scatterer Ω_1 that is translationally invariant along the z-axis, and surrounded by the air medium Ω_0 in the presence of an electromagnetic field $(\boldsymbol{E}^i, \boldsymbol{H}^i)$. Given the invariant property, the problem can be reduced to two dimensions in the xy-plane, where the boundary of the cross section is denoted as Γ, and $\hat{\boldsymbol{n}}$, $\hat{\boldsymbol{t}}$ are the outward unit normal and unit tangent to the boundary, respectively, as illustrated in Figure 5.1.

In this context, the integral operators defined in Chapter 2 need to be written on the line boundary Γ. The 2D Green's function, which is the solution to the Helmholtz equation in free space with the Sommerfeld radiation condition (2.42), is now expressed as [52, 90]

$$G_k(\boldsymbol{r}, \boldsymbol{r}') = -\frac{\mathrm{j}}{4} H_0^{(2)}(k \left\| \boldsymbol{r} - \boldsymbol{r}' \right\|) \,, \tag{5.1}$$

where $H_0^{(2)}$ is the Hankel function of zeroth order and second kind, defined as

$$H_0^{(2)}(z) = J_0(z) - \mathrm{j} Y_0(z) \,, \tag{5.2}$$

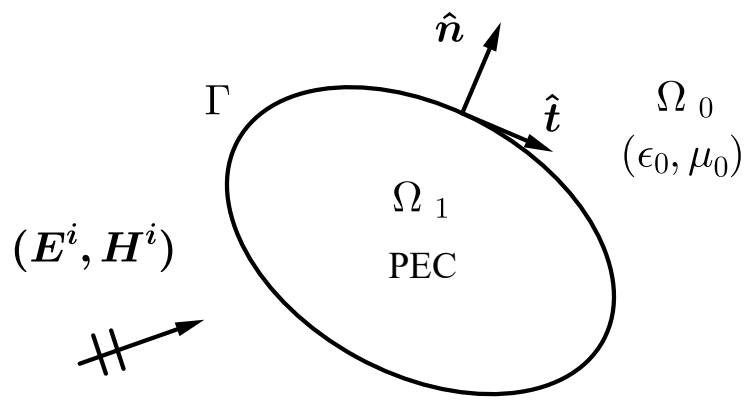

Figure 5.1: Cross section in the xy-plane of a z-invariant perfect electric conductor Ω_1 immersed in the air in the presence of an incident electromagnetic field $(\boldsymbol{E}^i, \boldsymbol{H}^i)$.

with J_0 and Y_0 the Bessel functions of the first and second kind, respectively, and of the zeroth order. The integral operators appearing in the EFIE and MFIE are defined on the boundary Γ as [90]

$$(\mathcal{S}_k f)(\boldsymbol{r}) = \frac{k\eta}{4} \int_\Gamma H_0^{(2)}(k\,\|\boldsymbol{r}-\boldsymbol{r}'\|)\, f(\boldsymbol{r}')\,\mathrm{d}\boldsymbol{r}'\,, \tag{5.3}$$

$$\begin{aligned}(\mathcal{N}_k f)(\boldsymbol{r}) = {} & \frac{k\eta}{4}\,\hat{\boldsymbol{t}} \cdot \int_\Gamma H_0^{(2)}(k\,\|\boldsymbol{r}-\boldsymbol{r}'\|)\, f(\boldsymbol{r}')\,\hat{\boldsymbol{t}}'\,\mathrm{d}\boldsymbol{r}' \\ & + \frac{\eta}{4k}\,\hat{\boldsymbol{t}} \cdot \nabla \int_\Gamma H_0^{(2)}(k\,\|\boldsymbol{r}-\boldsymbol{r}'\|) \nabla' \cdot (f(\boldsymbol{r}')\,\hat{\boldsymbol{t}}')\,\mathrm{d}\boldsymbol{r}'\,,\end{aligned} \tag{5.4}$$

$$(\mathcal{D}_k f)(\boldsymbol{r}) = \frac{\mathrm{j}k}{4} \int_\Gamma \cos\psi'\, H_1^{(2)}(k\,\|\boldsymbol{r}-\boldsymbol{r}'\|)\, f(\boldsymbol{r}')\,\mathrm{d}\boldsymbol{r}'\,, \tag{5.5}$$

$$(\mathcal{D}_k^* f)(\boldsymbol{r}) = \frac{\mathrm{j}k}{4} \int_\Gamma \cos\psi\, H_1^{(2)}(k\,\|\boldsymbol{r}-\boldsymbol{r}'\|)\, f(\boldsymbol{r}')\,\mathrm{d}\boldsymbol{r}'\,, \tag{5.6}$$

where $H_1^{(2)}$ is the Hankel function of the second kind and first order, and ψ, ψ' are, respectively, the angles between $\boldsymbol{r}-\boldsymbol{r}'$ and the surface normal vectors at positions $\boldsymbol{r}$ and $\boldsymbol{r}'$.

In two dimensions, any translationally invariant problem can be separated into the Transverse Magnetic (TM) and Tranverse Electric (TE) polarizations using the principle of superposition [48, 90]. In the case of TM polarization, the electric field is in the invariant z-direction, while the magnetic field is included in the plane. Since the electric surface current density is defined as

$$\boldsymbol{j}_s = \hat{\boldsymbol{n}} \times \boldsymbol{H}\,, \tag{5.7}$$

it only has a component along the z-axis. Conversely, in the TE case, the electric field and electric current density are inside the plane. In particular, $\boldsymbol{j}_s$ is tangential

to the boundary Γ. By taking advantage of this decomposition, the EFIE and MFIE can be rewritten as scalar equations. For the TM polarization, the EFIE becomes

$$\mathcal{S}_k(j_z) = E_z^i \,, \tag{5.8}$$

where j_z and E_z^i are the components along the z-axis of the current density and the incident electric field, respectively. In the TE case, the EFIE reads

$$\mathcal{N}_k(j_t) = E_t^i \,, \tag{5.9}$$

where j_t and E_t^i are the tangential components of the current density and the incident electric field, respectively. As for the MFIE, it is written in TM and TE polarizations, respectively, as

$$\frac{1}{2}\, j_z + \mathcal{D}_k^*(j_z) = H_t^i \,, \tag{5.10}$$

$$\frac{1}{2}\, j_t + \mathcal{D}_k(j_t) = H_z^i \,. \tag{5.11}$$

Lastly, we introduce the scalar Helmholtz operator

$$\mathcal{H}_k(f) = \left(k^2 + \Delta_\Gamma\right)(f) \,, \tag{5.12}$$

where Δ_Γ is the Laplace-Beltrami operator.

5.2.2 Discretization Strategy

To apply the boundary element method, the surface Γ is meshed with linear segments of average length h. At high frequencies, the edge length is typically chosen to be (smaller than) a tenth of the wavelength, i.e $h \leq \lambda/10$. Given that the unknown is a scalar quantity, we use either the pulse or hat basis functions [43]. The pulse functions are piecewise constant and defined for each segment e_i as

$$p_i(\boldsymbol{r}) = \begin{cases} 1 & \text{if } \boldsymbol{r} \in e_i \\ 0 & \text{if } \boldsymbol{r} \notin e_i \end{cases} . \tag{5.13}$$

The hat basis functions are instead defined on each vertex $\boldsymbol{v}_i$ where they have a value of 1 and decrease linearly to 0 on the adjacent vertices. They are expressed as

$$h_i(\boldsymbol{r}) = \begin{cases} \dfrac{\|\boldsymbol{r} - \boldsymbol{v}_{i-1}\|}{l_i^-} & \text{if } \boldsymbol{r} \in e_i^- \\ \dfrac{\|\boldsymbol{v}_{i+1} - \boldsymbol{r}\|}{l_i^+} & \text{if } \boldsymbol{r} \in e_i^+ \end{cases} , \tag{5.14}$$

where $l_i^\pm$ represents the length of edge $e_i^\pm$. Both types of basis functions are illustrated in Figure 5.2.

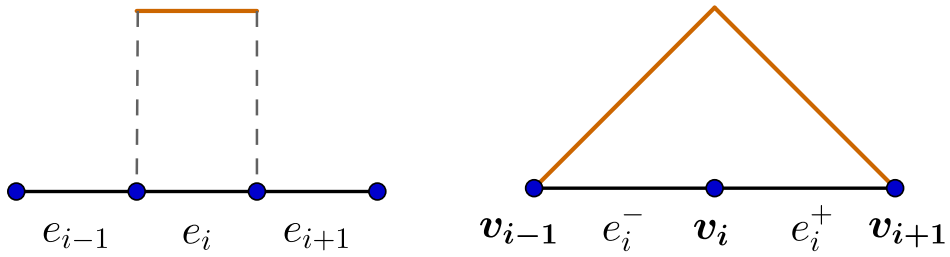

(a) (b)

Figure 5.2: (a) Pulse and (b) hat basis functions.

5.3 Spectral Analysis

In order to study the high frequency behavior of the integral operators, we consider an infinite cylinder with a circular cross section of radius a. We call spectrum elements of the continuous operator the equivalent of the eigenvalues for the discrete operator, which can be obtained analytically for this specific canonical geometry. On the circle, all operators share the same eigenvectors of the form [90]

$$v_q = \mathrm{e}^{-\mathrm{j}q\phi}\,, \quad q \in \mathbb{Z}\,, \tag{5.15}$$

which correspond to the Fourier modes. For any operator $\mathcal{A}$ defined on the circle, we denote its spectrum elements as $\lambda_q(\mathcal{A})$, $q \in \mathbb{Z}$, such that

$$\mathcal{A}v_q = \lambda_q(\mathcal{A})\, v_q\,, \tag{5.16}$$

where q is called the spectral index.

The fundamental case of the circle presents several benefits that facilitate the spectral analysis. First of all, given that all operators share the same eigenvectors, their spectrum elements can be added and multiplied one to one when adding and multiplying operators. For instance, given two operators $\mathcal{A}$ and $\mathcal{B}$, we have the properties, for any index q,

$$\lambda_q(\mathcal{A}+\mathcal{B}) = \lambda_q(\mathcal{A}) + \lambda_q(\mathcal{B})\,, \tag{5.17}$$

$$\lambda_q(\mathcal{A}\mathcal{B}) = \lambda_q(\mathcal{A})\lambda_q(\mathcal{B})\,. \tag{5.18}$$

This is particularly useful when designing multiplicative preconditioning strategies and combined equations. Additionally, since we are working with normal operators due to being on the circle [90], the singular values can be obtained simply by taking the absolute value of the spectrum elements. As will be shown afterward, the singular value spectrum can also be plotted against the spectral index rather than in decreasing order as conventionally done numerically. Consequently, conditioning tendencies and other phenomena such as resonances can be observed and understood more easily.

Moreover, by discretizing the circle with segments of the same length, the obtained boundary element matrices have the convenient property of being circulant. Due to this characteristic, the matrices can be reduced to one row only since the other rows are simply obtained by rotation. In this case, the discrete Fourier transform can be applied to perform matrix-matrix and matrix-vector products in quasi-linear complexity, as well as to get a fast singular value decomposition and a fast direct inverse. In the following, the spectra of different operators will be investigated to identify the high frequency asymptotic behavior and other specificities such as internal resonances.

5.3.1 TM EFIE

We start with the analysis of the EFIE in TM polarization (5.8). To find the spectrum elements $\lambda_q(\mathcal{S}_k)$ of the TM Electric Field Integral Operator (TM EFIO), we write

$$\mathcal{S}_k \, \mathrm{e}^{-\mathrm{j}q\phi} = \lambda_q(\mathcal{S}_k) \, \mathrm{e}^{-\mathrm{j}q\phi} \, . \tag{5.19}$$

Then, the Hankel function can be expressed in cylindrical coordinates as [90]

$$H_0^{(2)}(k \, \|\boldsymbol{\rho} - \boldsymbol{\rho}'\|) = \sum_{q=-\infty}^{\infty} J_q(ka) H_q^{(2)}(ka) \, \mathrm{e}^{-\mathrm{j}q(\phi-\phi')} \, . \tag{5.20}$$

From the definition of the operator $\mathcal{S}_k$ (5.3), the spectrum elements are thus expressed as [90, 52]

$$\lambda_q(\mathcal{S}_k) = \frac{1}{2} \, k\eta\pi a \, J_q(ka) \, H_q^{(2)}(ka) \, , \tag{5.21}$$

which are plotted in Figure 5.3 in the complex plane, for $0 \leq q \leq 149$. From this representation, a couple of issues can be observed. First, the spectrum elements pass by the origin multiple times, which corresponds to the resonance phenomenon and results in an unbounded condition number. Second, they appear to converge toward zero for large spectral indices. For a clearer inspection, we take the absolute value of the spectrum elements, from which the singular values are directly derived. The spectrum obtained in this way is displayed in Figure 5.4 at $2, 4$, and $6\,\mathrm{GHz}$ to illustrate the effect of the increase in frequency.

The concerns mentioned above from the complex representation can now be interpreted more easily from these graphs. The spectrum is divided into different portions with respect to the spectral index. The left section contains oscillations and represents the hyperbolic regime, characterized by $q < ka$. The zeros appearing in that part correspond to internal resonances and are linked to the existence of non physical solutions inside the closed cylinder [2, 90].

The right end of the spectrum represents the elliptic regime corresponding to $q > ka$. The effect of a denser discretization can be observed in that part, since on the circle, the spectrum of an operator matrix is an approximation of the analytical

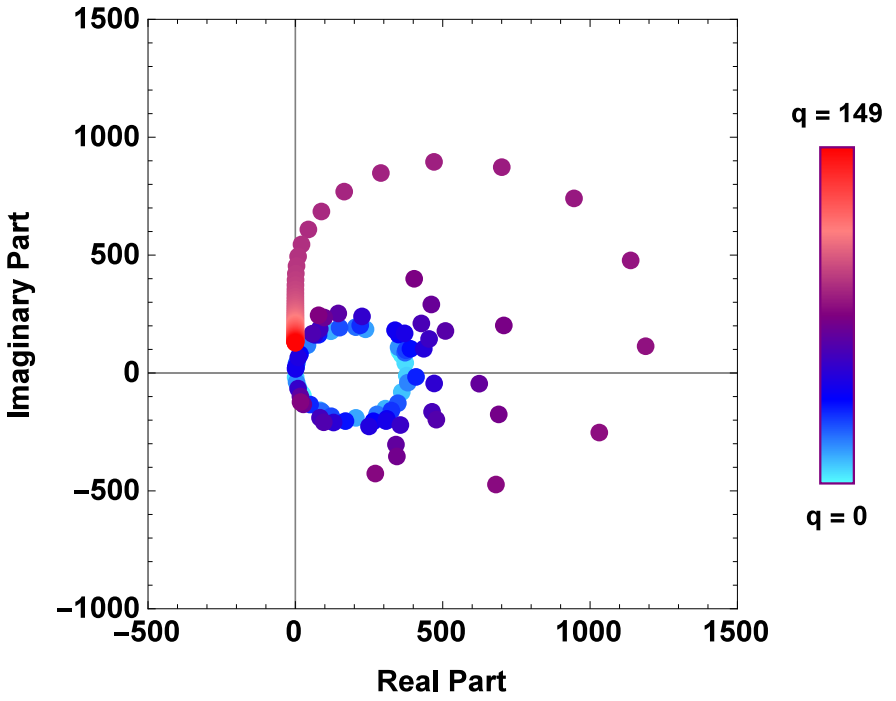

Figure 5.3: Eigenvalues of the TM EFIO at $f = 4\,\mathrm{GHz}$ for a circle of radius 1.

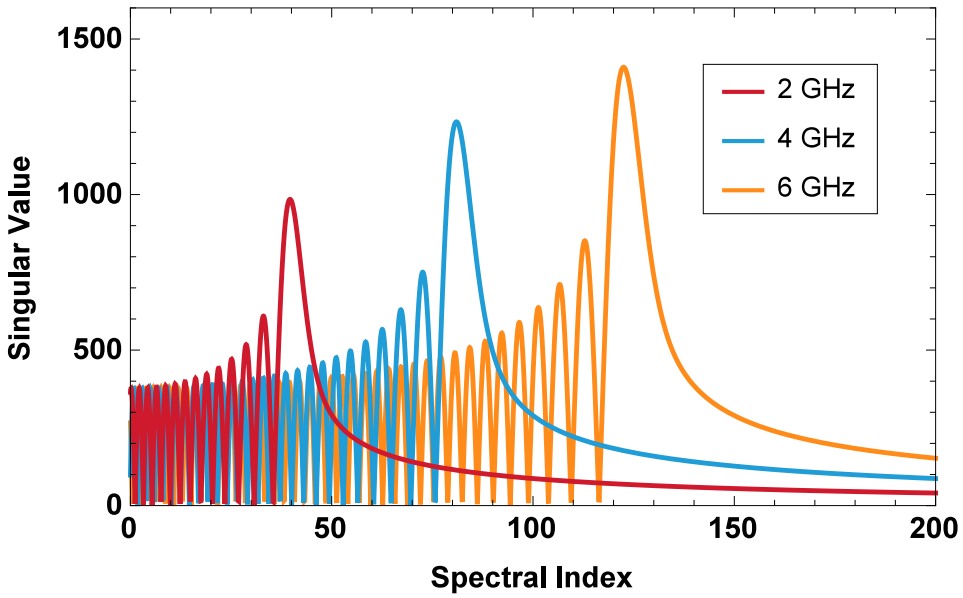

Figure 5.4: Singular value spectrum of the TM EFIO at different frequencies for a circle of radius 1.

spectrum. More precisely, if the discretized operator matrix is of size $N \times N$, then its spectrum corresponds to the analytical one for spectral indices in the range $0 \leq q \leq N-1$, only differing due to discretization error [90]. In the case of the TM EFIO, as observed in the complex plane, the singular values approach zero for higher spectral indices. This can also be confirmed through the asymptotic expressions of the Bessel and Hankel functions for large orders [67],

$$J_q(z) \underset{q\to+\infty}{\sim} \frac{1}{\sqrt{2\pi q}} \left(\frac{ez}{2q}\right)^q , \tag{5.22}$$

$$H_q^{(2)}(z) \underset{q\to+\infty}{\sim} \mathrm{j}\sqrt{\frac{2}{\pi q}} \left(\frac{ez}{2q}\right)^{-q} . \tag{5.23}$$

Substituting these into eq. (5.21), the spectrum elements of the TM EFIE operator asymptotically behave following

$$\lambda_q(\mathcal{S}_k) \underset{q\to+\infty}{\sim} \frac{\mathrm{j}k\eta a}{2q} , \tag{5.24}$$

which clearly converges to zero when $q \to \infty$. This type of elliptic behavior with q^{-n}, $n > 0$, is characteristic of the smoothing nature of this operator [90].

Lastly, the transitioning values around $q \approx ka$ constitute the major cause of the high frequency breakdown, which is due to the highest peak located between the hyperbolic and elliptic parts of the spectrum. This peak is connected to a surface resonance phenomenon and its value increases with the frequency, thus resulting in a conditioning breakdown [2].

5.3.2 TE EFIE

The spectrum elements of the TE EFIO (5.9) are defined so that

$$\mathcal{N}_k \, \mathrm{e}^{-\mathrm{j}q\phi} = \lambda_q(\mathcal{N}_k) \, \mathrm{e}^{-\mathrm{j}q\phi} . \tag{5.25}$$

and are expressed as [90]

$$\lambda_q(\mathcal{N}_k) = \frac{1}{2} \, k\eta\pi a \, J_q'(ka) \, H_q'^{(2)}(ka) , \tag{5.26}$$

where the $'$ symbol indicates the derivative. The values are illustrated in the complex plane as before in Figure 5.5. Similarly to the TM counterpart, the resonance phenomenon is observed due to spectrum elements passing through zero. For large spectral indices instead, the values diverge to infinity along the negative imaginary axis. The singular value spectrum is displayed in Figure 5.6 to identify these properties. The graph effectively exhibits internal resonances that increase in number

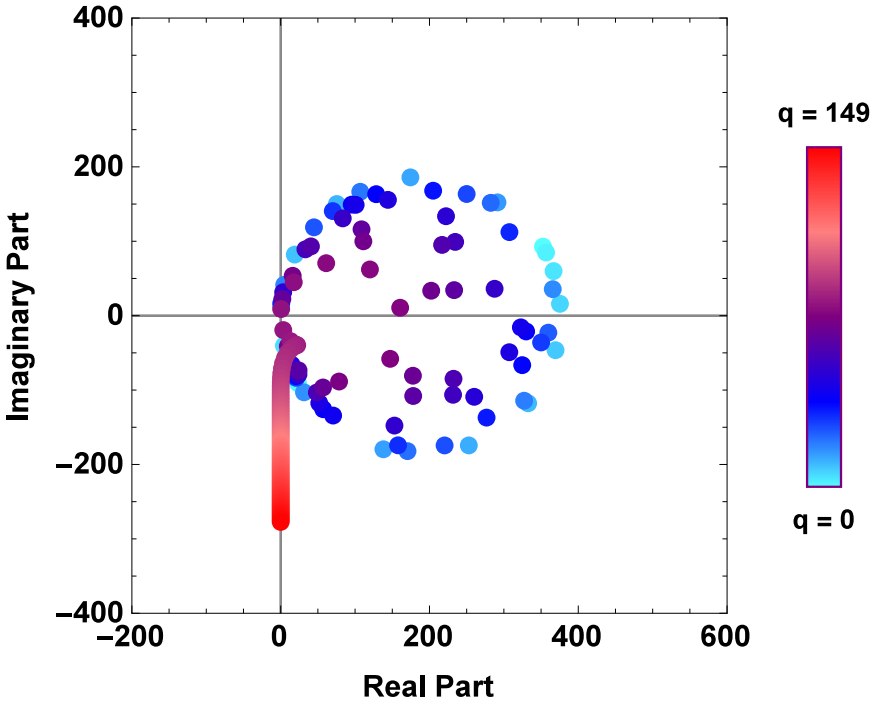

Figure 5.5: Eigenvalues of the TE EFIO at $f = 4\,\mathrm{GHz}$ for a circle of radius 1.

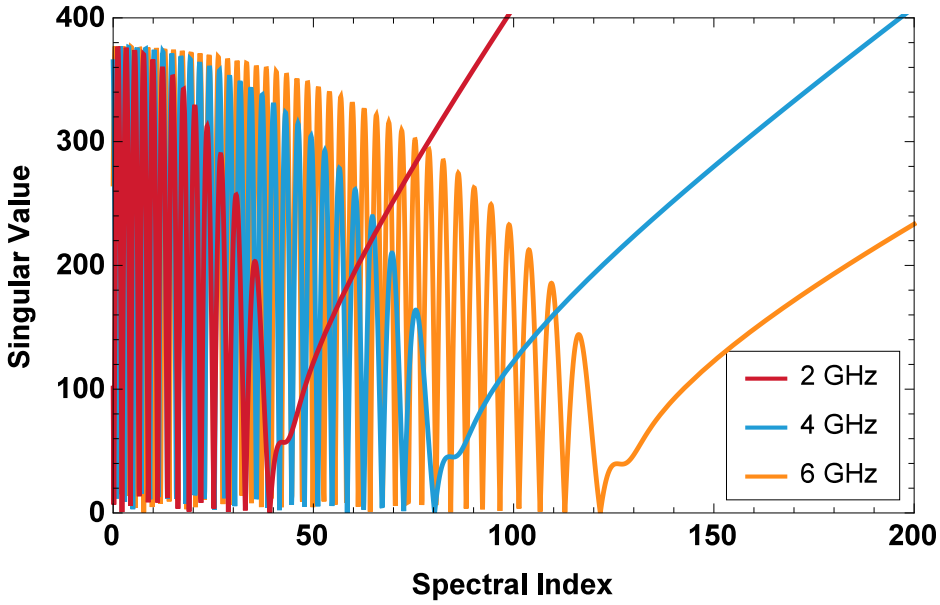

Figure 5.6: Singular value spectrum of the TE EFIO at different frequencies for a circle of radius 1.

with higher frequencies in the oscillating section. In the elliptic part of the spectrum, the values grow unboundedly, which is also seen in the expression of the spectrum elements for large orders [90],

$$\lambda_q(\mathcal{N}_k) \underset{q\to+\infty}{\sim} -\frac{\mathrm{j}q\eta}{2ka}\,. \tag{5.27}$$

The spectrum elements asymptotically follow q^n, $n > 0$, and indicate the differentiating power of the scalar potential operator [90]. Finally, in the intermediate section of the spectrum, rather than a growing peak, a small decreasing bump can be observed right after the last oscillating peak, located around index $q \approx ka$.

5.3.3 TM and TE MFIE

The MFIOs defined for the TM and TE polarizations on the circle in eqs. (5.10) and (5.11) share the same spectrum elements [52, 90]. We use the notation for the TM MFIO but the results are valid for both polarizations. Therefore, we have

$$(\mathcal{I}/2 + \mathcal{D}_k^*)\,\mathrm{e}^{-\mathrm{j}q\phi} = \lambda_q(\mathcal{I}/2 + \mathcal{D}_k^*)\,\mathrm{e}^{-\mathrm{j}q\phi}\,. \tag{5.28}$$

As a result, the spectrum elements for the MFIO are defined as

$$\lambda_q(\mathcal{I}/2 + \mathcal{D}_k^*) = -\frac{1}{2}\,\mathrm{j}k\pi a\, J_q'(ka)\, H_q^{(2)}(ka)\,. \tag{5.29}$$

An examination of the complex representation in Figure 5.7 reveals both similar and distinct features from the EFIO. On one hand, the spectrum elements form a circle passing through the origin, meaning that resonances are also present for the MFIE operator. On the other hand, the values converge to the real value 0.5, thus indicating stability in the dense discretization regime. This is a consequence of the MFIO being a second-kind operator, here composed of the sum of an identity and a compact operator [90]. For the frequency dependent behavior, the singular value spectrum is illustrated in Figure 5.8. The increase of frequency simply adds more oscillations and resonances, but the maximum amplitude remains fixed. Moreover, the convergence for large spectral indices clearly appears, so that the only issue for this operator is the presence of the internal resonances, which are usually removed by building a Combined Field Integral Equation (CFIE).

5.3.4 Helmholtz

The derivation of the spectrum for the Helmholtz operator $\mathcal{H}_k$ is more straightforward given its relatively simpler expression. For any index $q \in \mathbb{Z}$, applying the operator to the eigenvector $\mathrm{e}^{-\mathrm{j}q\phi}$ gives

$$\mathcal{H}_k(\mathrm{e}^{-\mathrm{j}q\phi}) = \left(k^2 + \Delta_\Gamma\right)\mathrm{e}^{-\mathrm{j}q\phi} \tag{5.30}$$

$$= \left(k^2 - \left(\frac{q}{a}\right)^2\right)\mathrm{e}^{-\mathrm{j}q\phi}\,, \tag{5.31}$$

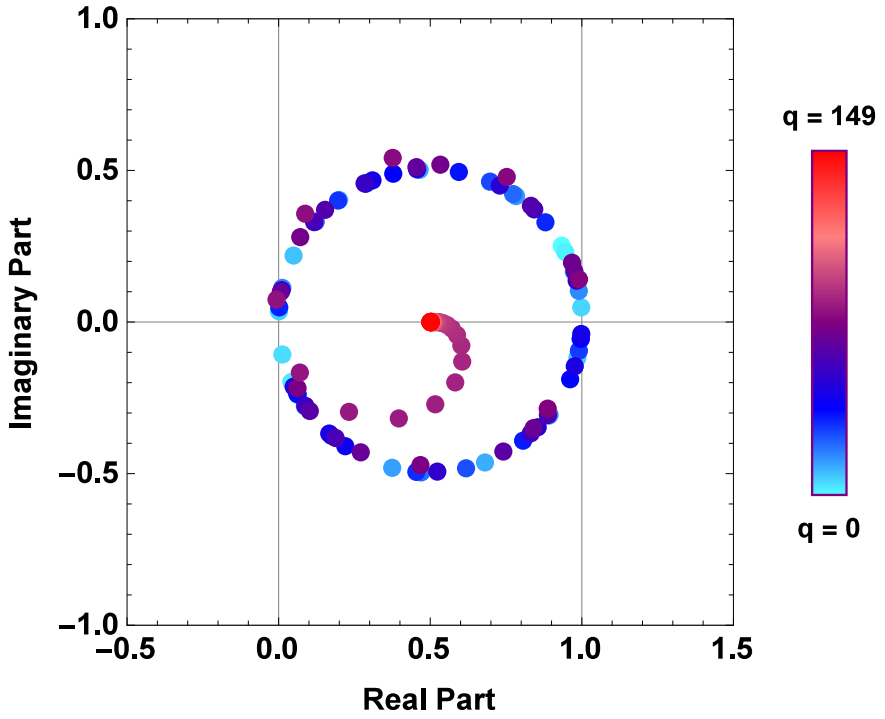

Figure 5.7: Eigenvalues of the MFIO at $f = 4\,\mathrm{GHz}$ for a circle of radius 1.

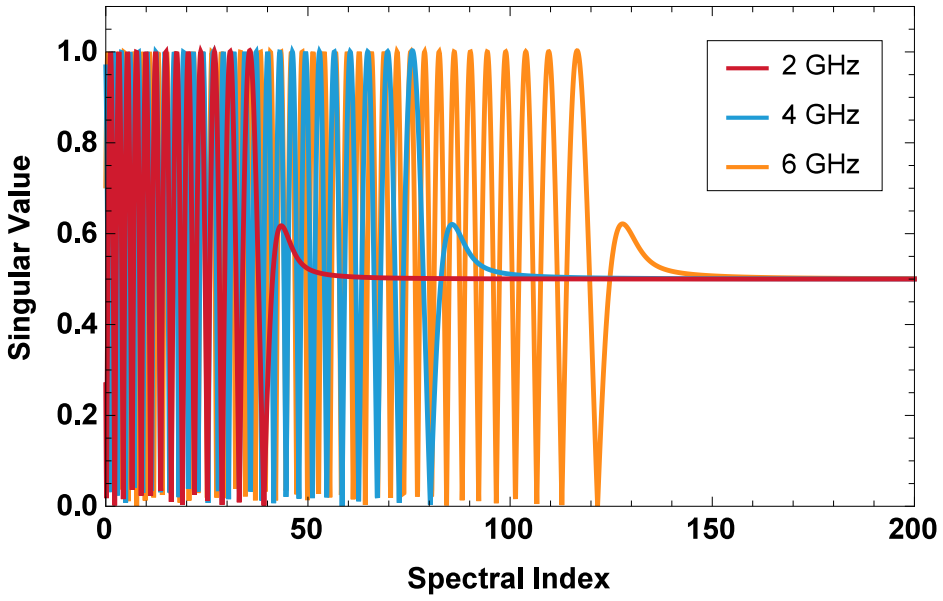

Figure 5.8: Singular value spectrum of the MFIO at different frequencies for a circle of radius 1.

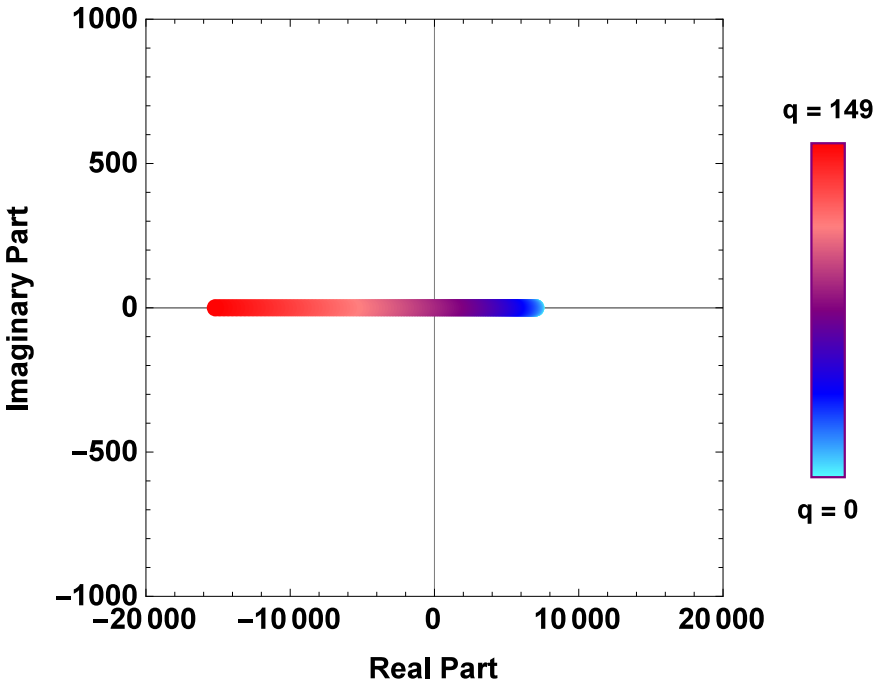

Figure 5.9: Eigenvalues of the Helmholtz operator at $f = 4\,\mathrm{GHz}$ for a circle of radius 1.

from which we deduce the spectrum elements expressed as

$$\lambda_q(\mathcal{H}_k) = k^2 - \left(\frac{q}{a}\right)^2 . \tag{5.32}$$

This corresponds to a quadratic function with an offset equal to k^2. In particular, the function has a zero when $q = ka$, matching the spectral position between the hyperbolic and elliptic regimes. All values are real, as can be seen from the complex representation in Figure 5.9. The singular value spectrum is plotted in Figure 5.10 and clearly shows the zero located at $q = ka$. As implied by the Laplacian operator and the asymptotic expression of the spectrum elements for large orders $(-(q/a)^2)$, the Helmholtz operator has a stronger differentiating power compared with the TE EFIO. This property will become useful afterward for the design of the new formulation.

5.4 Conditioning Treatments

To summarize the observations made for the above operators, the possible spectral issues that affect the conditioning are:

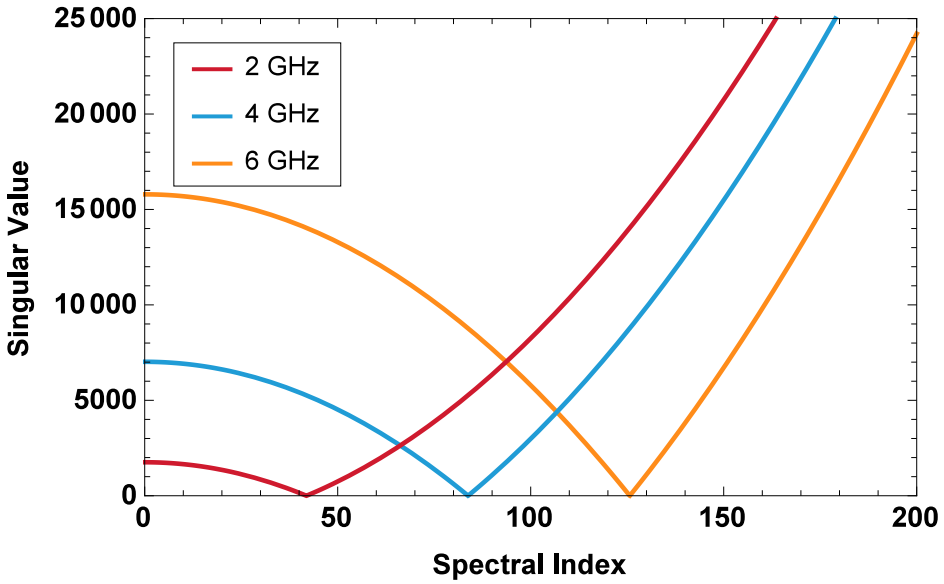

Figure 5.10: Singular value spectrum of the Helmholtz operator at different frequencies for a circle of radius 1.

- Internal resonances: the presence of zeros in the oscillating part of the spectrum corresponds to the existence of non physical solutions due to the closed cylinder and evidently results in an unbounded condition number. This issue involves both electric and magnetic equations.
- High frequency breakdown: the increase of frequency causes a growth of the surface resonance peak of the TM EFIO spectrum and thus an increase of the condition number.
- Dense discretization breakdown: at a given frequency, a finer discretization of the mesh increases the number of unknowns and the largest spectral index. Both EFIOs experience a breakdown in this case, where the TM EFIO spectrum converges to zero while the TE EFIO spectrum diverges to infinity. Although the focus of the chapter is on the high frequency breakdown, the two types of ill-conditioning are closely related in this scenario due to the requirement for the level of discretization with respect to the wavelength.

In the following, we aim to propose a formulation for the TM polarization which is well-conditioned with regards to each of these aspects.

5.4.1 Combined Field Integral Equation

We start by examining the standard CFIE, which is usually employed to treat resonances. The formulation is built by adding together the EFIE (5.8) and MFIE

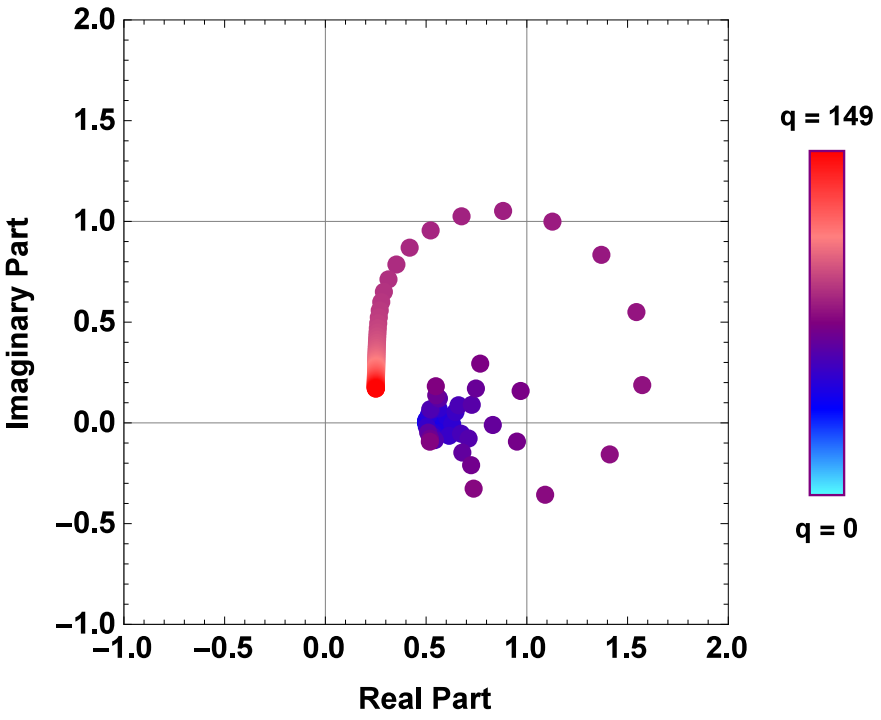

Figure 5.11: Eigenvalues of the CFIO at $f = 4\,\text{GHz}$ for a circle of radius 1.

(5.10) [61], written as

$$\alpha \frac{1}{\eta} \mathcal{S}_k(j_z) + (1-\alpha) \left(\frac{\mathcal{I}}{2} + \mathcal{D}_k^* \right)(j_z) = \alpha \frac{1}{\eta} E_z^i + (1-\alpha) H_t^i \,, \tag{5.33}$$

where α is used to balance the contribution of each term, and taken as 0.5 for the rest of the chapter to obtain an equal contribution from both equations [54]. Moreover, the EFIE has been multiplied by $1/\eta$ to normalize the operator with respect to the MFIE. As mentioned previously, the derivation of the spectrum for combined equations is fairly simple on the circle. For any spectral index q, the spectrum elements of the CFIO can be written as

$$\alpha \frac{1}{\eta} \lambda_q(\mathcal{S}_k) + (1-\alpha)\, \lambda_q(\mathcal{I}/2 + \mathcal{D}_k^*) \,. \tag{5.34}$$

These values are plotted at 4 GHz in the complex plane in Figure 5.11 and the singular value spectrum is illustrated in Figure 5.12 for increasing frequencies on a circle of radius 1.

From both graphs, we can observe that internal resonances have been entirely eliminated. More precisely, the combination of the EFIE and MFIE prevents the apparition of a resonant nullspace for real frequencies [24]. Furthermore, the operator is also stable in the elliptic part, which can be seen with the large order

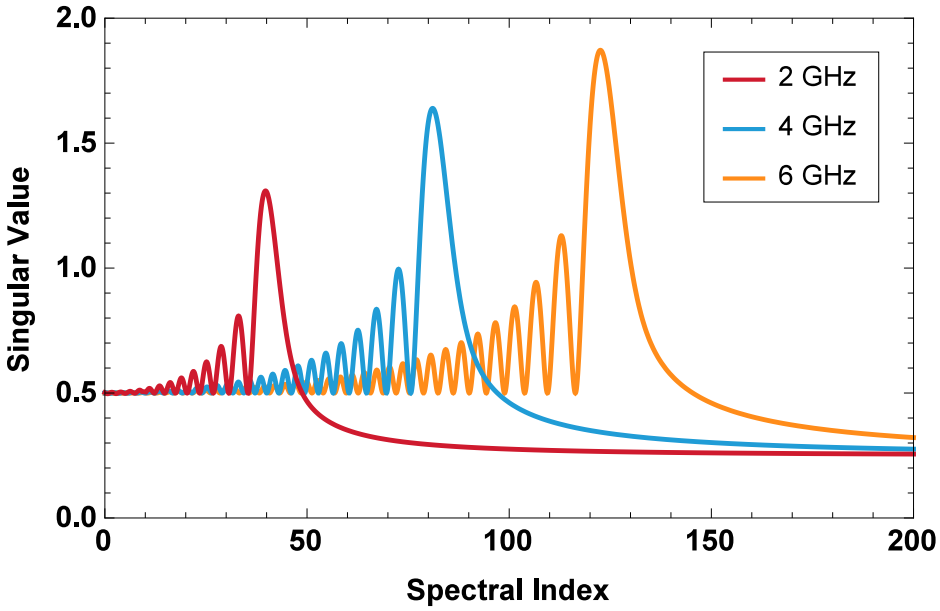

Figure 5.12: Singular value spectrum of the standard CFIO at different frequencies for a circle of radius 1.

approximation [90]

$$\alpha \frac{1}{\eta} \lambda_q(\mathcal{S}_k) + (1-\alpha)\, \lambda_q(\mathcal{I}/2 + \mathcal{D}_k^*) \underset{q\to+\infty}{\sim} \frac{\mathrm{j}ka}{4q} + \frac{1}{4} + \frac{(ka)^2}{8|q|^3} \underset{q\to+\infty}{\sim} \frac{1}{4}\,. \tag{5.35}$$

Unfortunately, the CFIE still suffers from the high frequency breakdown, inherited from the EFIE, as shown by the growing surface resonance peak. Consequently, although the CFIE is able to remove resonances and preserve the second-kind property of the MFIO, it still needs to be improved to include a cure for the high frequency ill-conditioning.

5.4.2 Calderón EFIE and CFIE

The high frequency breakdown caused by the peak growth can be fixed with a multiplication by another adequate operator. In particular, we refer to the following Calderón identity [66],

$$\mathcal{N}_k\, \mathcal{S}_k = \frac{\mathcal{I}}{4} - \mathcal{D}_k^{*2}\,. \tag{5.36}$$

This relation shows that we can obtain a second-kind operator when multiplying both EFIE operators. This identity is therefore generally used to fix the dense

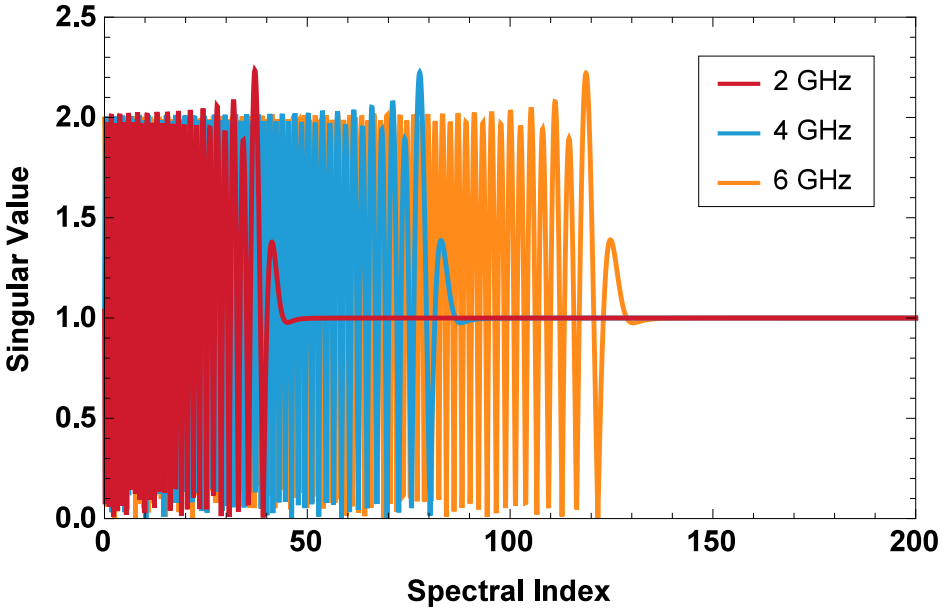

Figure 5.13: Singular value spectrum of the Calderón EFIO at different frequencies for a circle of radius 1.

discretization breakdown of the EFIE [4, 29]. Here we consider the 2D equation

$$\frac{4}{\eta^2}\,\mathcal{N}_k\,\mathcal{S}_k(j_z) = \frac{4}{\eta^2}\,\mathcal{N}_k\,E_z^i\,, \tag{5.37}$$

where the normalization is made to obtain an exact identity. The associated spectrum elements are thus

$$\frac{4}{\eta^2}\,\lambda_q(\mathcal{N}_k)\lambda_q(\mathcal{S}_k)\,, \tag{5.38}$$

and the associated singular value spectrum is plotted in Figure 5.13 at different frequencies. As predicted by the Calderón identity, the end of the spectrum effectively converges toward a constant value for large spectral indices [90]. More interestingly, the peak increase of the TM EFIO has been compensated by the TE EFIO so that the maximum amplitude of the oscillations remains constant with the frequency. The remaining operation is thus the removal of the internal resonances.

Based on the results obtained for the CFIE in the previous subsection, we consider adding the MFIE to the Calderón EFIE, which gives the following Calderón CFIE

$$\frac{4\,\alpha}{\eta^2}\,\mathcal{N}_k\,\mathcal{S}_k(j_z) + 2\,(1-\alpha)\,\left(\frac{\mathcal{I}}{2} + \mathcal{D}_k^*\right)(j_z) = \frac{4\,\alpha}{\eta^2}\,\mathcal{N}_k\,E_z^i + 2\,(1-\alpha)H_t^i\,, \tag{5.39}$$

and the corresponding spectrum elements

$$\frac{4\,\alpha}{\eta^2}\,\lambda_q(\mathcal{N}_k)\lambda_q(\mathcal{S}_k) + 2\,(1-\alpha)\,\lambda_q(\mathcal{I}/2 + \mathcal{D}_k^*)\,. \tag{5.40}$$

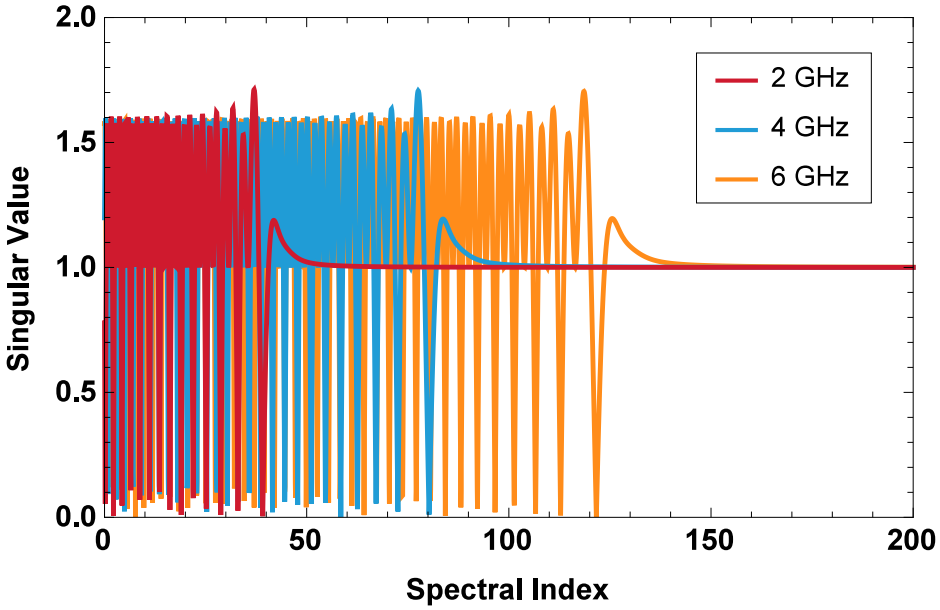

Figure 5.14: Singular value spectrum of the Calderón CFIO at different frequencies for a circle of radius 1.

The resulting singular value spectrum is illustrated in Figure 5.14, where only part of the zeros have been actually eliminated.

5.4.3 Complex Calderón CFIE

In order to remove the remaining resonances while maintaining the high frequency and dense discretization properties obtained thus far, the use of a suitable complex wave number was suggested in [2, 31]. The modified wave number, denoted as k_m, is used in the TE EFIE operator, as well as in a second MFIE operator added for symmetry. The complex Calderón CFIE operator is thus written

$$\frac{4\,k_m}{k\eta^2}\,\alpha\,\mathcal{N}_{k_m}\,\mathcal{S}_k + 4\,(1-\alpha)\left(\frac{\mathcal{I}}{2} - \mathcal{D}^*_{k_m}\right)\left(\frac{\mathcal{I}}{2} + \mathcal{D}^*_{k}\right), \tag{5.41}$$

where the additional factors have been included for appropriate asymptotic normalization. The requirements for the complex wave number are that $\Re(k_m) \propto k$ and $\Im(k_m) \propto k^{1/3}$. We have chosen the value proposed in [35, 7, 34, 6] and derived from an optimization problem,

$$k_m = k - \mathrm{j}0.4k^{1/3}a^{-2/3}\,. \tag{5.42}$$

The spectrum elements for this operator are thus

$$\frac{4\,k_m}{k\eta^2}\,\alpha\,\lambda_q(\mathcal{N}_{k_m})\,\lambda_q(\mathcal{S}_k) + 4\,(1-\alpha)\,\lambda_q(\mathcal{I}/2 - \mathcal{D}^*_{k_m})\,\lambda_q(\mathcal{I}/2 + \mathcal{D}^*_{k})\,, \tag{5.43}$$

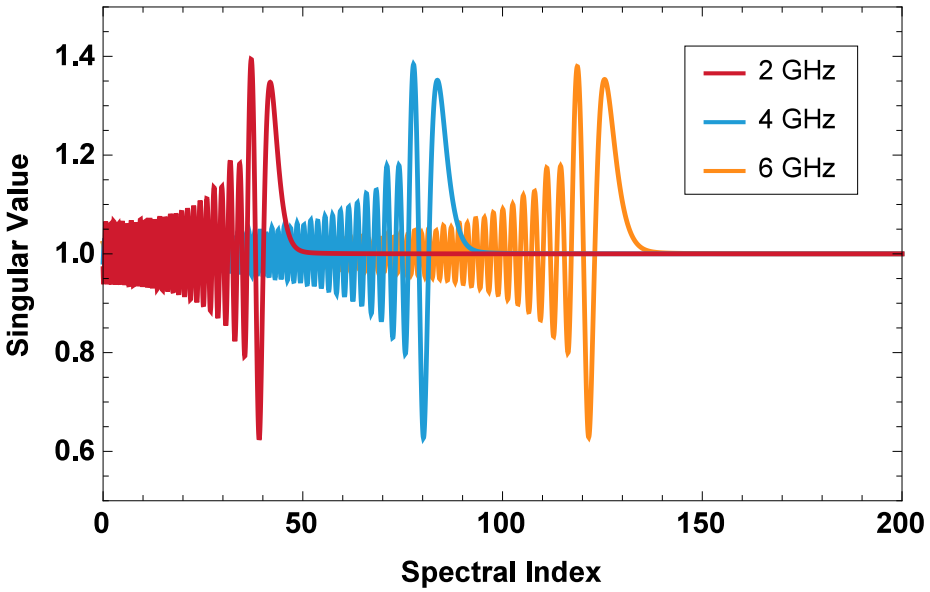

Figure 5.15: Singular value spectrum of the complex Calderón CFIO at different frequencies for a circle of radius 1.

where

$$\lambda_q(\mathcal{I}/2 - \mathcal{D}^*_{k_m}) = 1 + \frac{1}{2}\,\mathrm{j}k\pi a\, J'_q(ka)\, H^{(2)}_q(ka)\,. \tag{5.44}$$

The choice of normalization factors has been made from the large order expansion of the spectrum elements. More precisely, the asymptotic expressions for the EFIO and MFIO [67, 90] are

$$\lambda_q(\mathcal{S}_k) \underset{q\to+\infty}{\sim} \frac{\mathrm{j}k\eta a}{2q}\,, \tag{5.45}$$

$$\lambda_q(\mathcal{N}_k) \underset{q\to+\infty}{\sim} -\frac{\mathrm{j}q\eta}{2ka}\,, \tag{5.46}$$

$$\lambda_q(\mathcal{D}^*_k) \underset{q\to+\infty}{\sim} \frac{1}{2}\,. \tag{5.47}$$

From these expansions, the normalization factor of the MFIE term is straightforward. As for the EFIE term, multiplying the expressions for the TM EFIO and the TE EFIO gives

$$\lambda_q(\mathcal{N}_{k_m})\,\lambda_q(\mathcal{S}_k) \underset{q\to+\infty}{\sim} \frac{k\eta^2}{4k_m}\,, \tag{5.48}$$

hence the factor used in (5.43).

The singular values are then plotted in Figure 5.15 for several frequencies. We can observe from the graph that the formulation obtained does not contain zeros, and therefore seems free of internal resonances. Additionally, the spectrum appears stable in the high frequency and dense discretization regimes. The complex plane

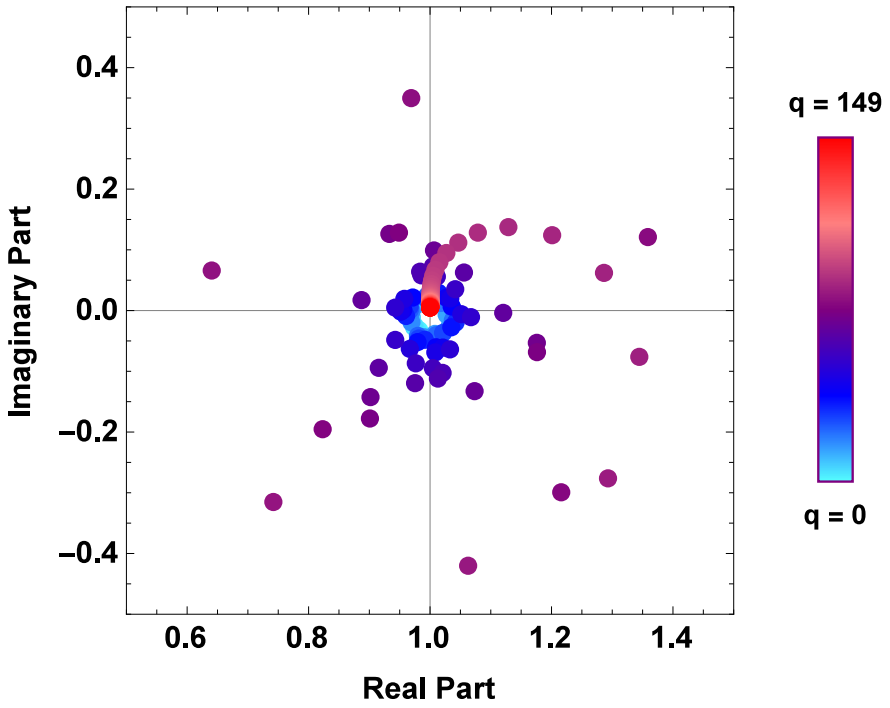

Figure 5.16: Eigenvalues of the complex Calderón CFIO at $f = 4\,\mathrm{GHz}$ for a circle of radius 1.

representation is also given in Figure 5.16, where the values are cleanly grouped around 1. From numerical evidence, this integral equation effectively treats the target issues highlighted at the beginning of this section by exploiting the Calderón identity. In the following section, we propose an alternative integral equation that does not rely on this identity.

5.5 Helmholtz Operator-Based High Frequency Stable Formulation

We now design a new combined formulation by taking advantage of the properties of the Helmholtz operator introduced previously rather than the Calderón identity. Compared with the complex Calderón CFIE, the TE EFIE operator is replaced by an operator with the same differentiating power while the MFIE term is left untouched. More precisely, the square root of the Helmholtz operator has the same differentiating power as the TE EFIO, characterized by an expression for their spectrum elements containing q (power $+1$) for large orders. By inserting the complex wave number (5.42) defined previously, the real zero of the Helmholtz operator is also removed, as seen in Figure 5.17, so that its spectrum presents a

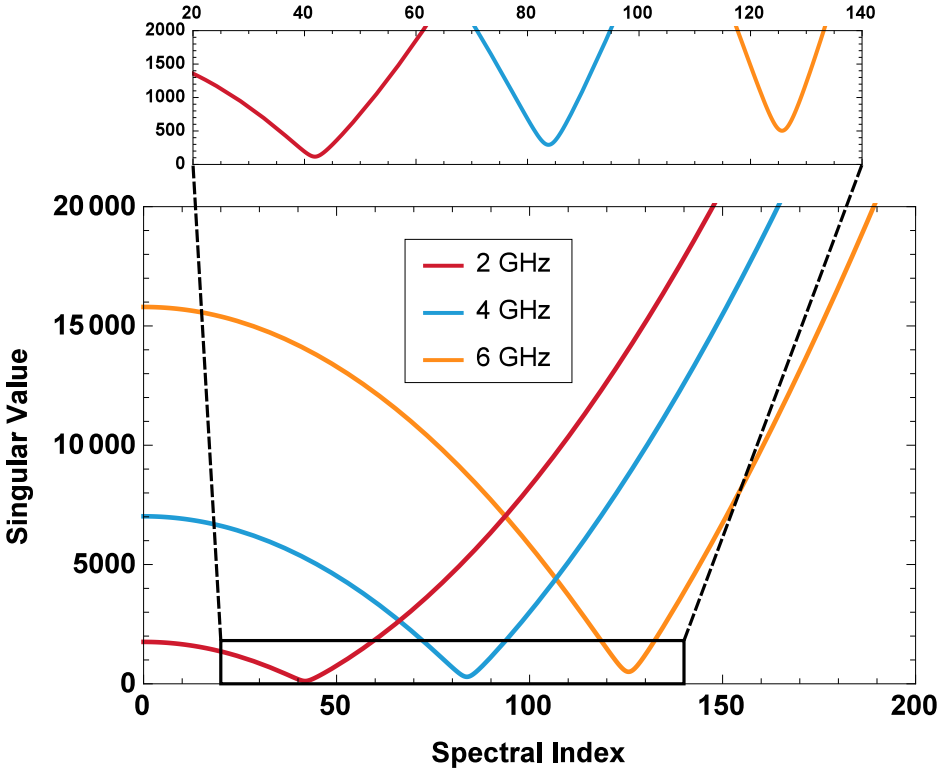

Figure 5.17: Singular value spectrum of the Helmholtz operator with complex wave number k_m at different frequencies for a circle of radius 1.

minimum which can counteract the growing peak of the TM EFIO.

However, finding the square root of a matrix is an expensive operation. Therefore, rather than directly replacing the TE EFIO by the square root of the Helmholtz operator, the latter is first applied as a whole. Since it has a differentiating power $+2$, whereas the TM EFIO is characterized by an smoothing power -1, a second TM EFIO including the complex wave number k_m is used to obtain a constant asymptotic value. As a result, we define the new Helmholtz preconditioned CFIE

$$\frac{4\,\alpha}{k k_m \eta^2 a^2}\,\mathcal{S}_{k_m}\,\mathcal{H}_{k_m}\,\mathcal{S}_k + 4\,(1-\alpha)\left(\frac{\mathcal{I}}{2} - \mathcal{D}^*_{k_m}\right)\left(\frac{\mathcal{I}}{2} + \mathcal{D}^*_{k}\right) = \frac{4\,\alpha}{k k_m \eta^2 a^2}\,\mathcal{S}_{k_m}\,\mathcal{H}_{k_m}\,E^i_z + 4\,(1-\alpha)\left(\frac{\mathcal{I}}{2} - \mathcal{D}^*_{k_m}\right) H^i_t\,, \quad (5.49)$$

where the normalization factors are again selected to get a large order asymptotic value of 1 for the spectrum, given that

$$\lambda_q(\mathcal{H}_k) \underset{q\to+\infty}{\sim} -\left(\frac{q}{a}\right)^2\,, \quad (5.50)$$

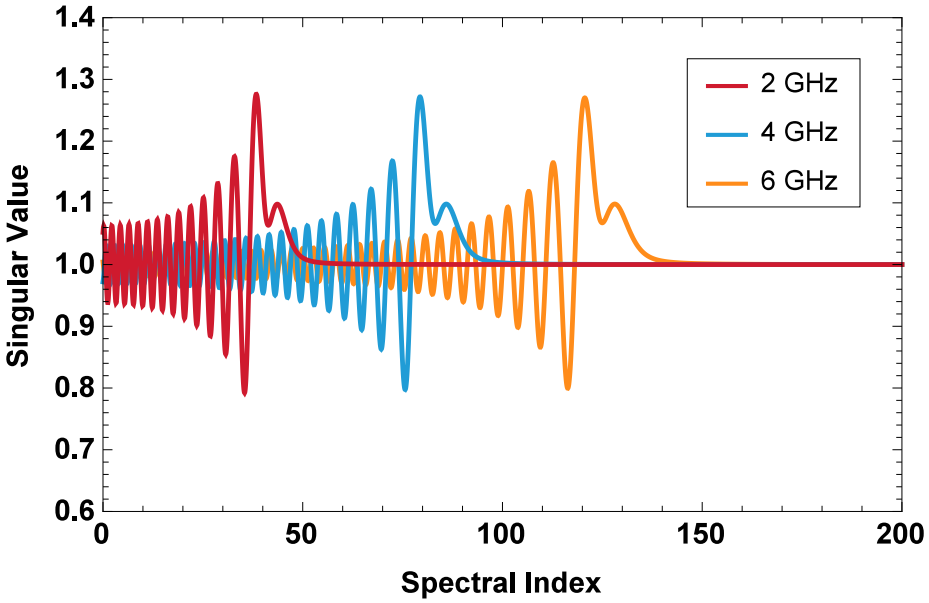

Figure 5.18: Singular value spectrum of the Helmholtz preconditioned CFIO at different frequencies for a circle of radius 1.

from which we obtain the expression for the EFIE term,

$$\lambda_q(\mathcal{S}_{k_m})\,\lambda_q(\mathcal{H}_{k_m})\,\lambda_q(\mathcal{S}_k) \underset{q\to+\infty}{\sim} \frac{kk_m\eta^2a^2}{4}\,. \tag{5.51}$$

Therefore, the spectrum elements associated to the proposed integral equation are

$$\frac{4\,\alpha}{kk_m\eta^2a^2}\,\lambda_q(\mathcal{S}_{k_m})\,\lambda_q(\mathcal{H}_{k_m})\,\lambda_q(\mathcal{S}_k) + 4\,(1-\alpha)\,\lambda_q(\mathcal{I}/2-\mathcal{D}^*_{k_m})\,\lambda_q(\mathcal{I}/2+\mathcal{D}^*_k)\,. \tag{5.52}$$

The singular value spectrum is given in Figure 5.18 and appears similar to the spectrum of the complex Calderón CFIO, i.e. a finite and constant condition number (which is also slightly better) can be observed since the spectrum does not present any zeros and there are neither high frequency nor dense discretization breakdowns. The complex plane representation in Figure 5.19 also shows the spectrum elements clearly clustered around and converging to 1.

5.6 Conclusion

We have presented in this chapter a novel boundary integral equation to model PECs at high frequencies. The formulation was derived as the outcome of a spectral analysis in two dimensions on the infinite cylinder by taking advantage of the fact that the eigenvectors are shared by all operators on this canonical geometry. The

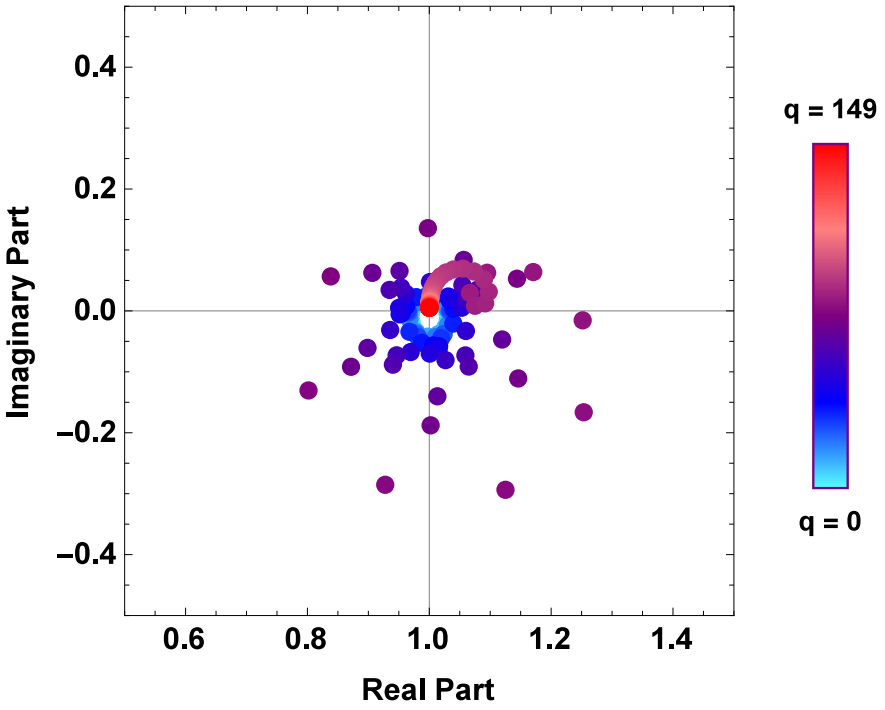

Figure 5.19: Eigenvalues of the Helmholtz preconditioned CFIO at $f = 4\,\mathrm{GHz}$ for a circle of radius 1.

proposed equation appears well-conditioned from several viewpoints and presents additional strong points compared with existing methods:

- High frequency stability: By taking advantage of the Helmholtz operator and incorporating a specific complex wave number, the high frequency ill-conditioning of the EFIE caused by the surface resonance can be effectively cured.
- Constant conditioning for finer discretizations: The dense discretization breakdown originally present for the EFIE is also removed with the proposed scheme. This issue holds as much importance as the high frequency breakdown in the regime of study given that larger frequencies also require a finer mesh.
- No internal resonances: The resonances that appear in the oscillating part of both EFIO and MFIO spectra are completely eliminated by combining the operators and inserting a complex wave number.
- Better complexity and performance: The adopted approach only involves the computation of two integral operators (TM EFIO and MFIO), considering

that the Helmholtz operator is purely derivative. As a result, the formulation is simpler to construct while preserving excellent conditioning properties.

This preliminary approach revolves around the canonical cylinder and specifically aims to provide more insight into the use of boundary integral equations for high frequencies. Current considerations and future prospects are given in the next closing chapter.

Chapter 6

Conclusion and Future Research

The work described in this thesis was centered around the notion of integral equation preconditioning, which constitutes one of the major aspects of computational electromagnetics. In particular, we successfully presented two original contributions of great interest for practical applications. We first introduced a well-conditioned equation for the simulation of eddy currents, which employs a quasi-Helmholtz decomposition with projectors on the Poggio-Miller-Chang-Harrington-Wu-Tsai (PMCHWT) equation for lossy conductors. Secondly, we proposed a stable 2D formulation designed for high frequencies on the infinite cylinder, taking advantage of the Helmholtz operator to offer a simpler and more efficient strategy. While both equations effectively fulfill their roles, further research avenues are available to improve their performance and attractiveness. On the topic of eddy current modeling, potential leads include:

- Enhancement of the solver: Additional features can be integrated to improve the solver, notably regarding the acceleration of the simulations with a fast solver to fully leverage the proposed scheme. Thorough implementation of other test cases could also be added, starting with scenarios based on voltage excitations.

- Adaptive full-wave solver: Currently, the passage from low to high frequency is done manually by setting to 1 the rescaling coefficients, or, equivalently, by simply using the original PMCHWT equation. Ideally, the solver should be able to automatically determine whether the projector-based preconditioning is needed depending on the size of the geometry and the simulation frequency.

- Dense discretization preconditioning: The increase of the condition number with finer discretizations is left untouched by the use of quasi-Helmholtz projectors. Therefore, an adapted preconditioning method such as a Calderón scheme could be incorporated to completely remove this type of breakdown, such as done in [13].

- Layered structures: For complex objects involving different types of materials, the preconditioned equation could be extended to create a multi-layer PMCHWT formulation that takes into account the changes of parameters between layers.

As for the subject of high frequency preconditioning, the work described in this thesis constitutes a foundation opening the path to several prospects for further contributions. A variety of interesting research ideas can be investigated, among which are:

- Complete solver implementation: Starting with the implementation of the proposed formulation, the setup of a numerical simulation environment for high frequencies along with an adequate fast solver would form a solid basis for future improvements including those mentioned below.

- Extension to arbitrary 2D structures: The proposed formulation is valid for the particular case of the infinite cylinder and serves as groundwork for a generalization to arbitrary shapes. The choice of the complex wave number should play an important role in this endeavor.

- Adaptation for 3D geometries: The transition to scenarios in three dimensions is undoubtedly quite intricate as it introduces further challenges. Similar to the infinite cylinder in 2D, a study on the canonical sphere could serve to establish a reliable starting point to evaluate the characteristics of 3D operators at high frequencies.

- Estimation of the impact of the spectral error: The application of the boundary element method to obtain matrix equations represents an approximation of the spectrum elements for each operator, and thus of the spectrum. As detailed in [90], a spectral error is introduced by the discretization process, which could be examined to evaluate whether it has detrimental consequences or not.

- Spectrum dispersion of the Helmholtz operator: Another issue related to the discretization shifts the eigenvalues of the Helmholtz operator so that its peak progressively diverges as the frequency increases. As a result, the operator cannot properly act as a preconditioner for the EFIE at very high frequencies. While this phenomenon might be linked to the spectral error, the insertion of a frequency offset inside the complex wave number could be one solution to this issue.

Appendix A

Cancellation of the Integral of a Global Loop Function

Consider a global loop function $\boldsymbol{h}$ defined on the smooth boundary Γ of a closed object $\Omega \in \mathbb{R}^3$. The objective is to demonstrate that

$$\iint_{\Gamma} \boldsymbol{h}(\boldsymbol{r})\,\mathrm{d}\boldsymbol{r} = \boldsymbol{0}\,. \tag{A.1}$$

Proof. Let $\boldsymbol{C} \in \mathbb{R}^3$ be a constant vector field. Then, using a vector identity for the divergence operator, we can write

$$\begin{aligned}
\langle \boldsymbol{h}, \boldsymbol{C} \rangle &= \iint_{\Gamma} \boldsymbol{h}(\boldsymbol{r}) \cdot \boldsymbol{C}\,\mathrm{d}\boldsymbol{r} && \text{(A.2)}\\
&= \iint_{\Gamma} \boldsymbol{h}(\boldsymbol{r}) \cdot \nabla\,(\boldsymbol{r} \cdot \boldsymbol{C})\,\mathrm{d}\boldsymbol{r} && \text{(A.3)}\\
&= -\iint_{\Gamma} \nabla \cdot \boldsymbol{h}(\boldsymbol{r})\,(\boldsymbol{r} \cdot \boldsymbol{C})\,\mathrm{d}\boldsymbol{r} && \text{(A.4)}\\
&= 0\,, && \text{(A.5)}
\end{aligned}$$

since a global loop function is divergence-free. From here, we denote the x, y and z components of any vectorial quantity with the indices $\{x, y, z\}$ respectively.

Next, we consider $\boldsymbol{C} = C_x \hat{\boldsymbol{x}}$, with $C_x \in \mathbb{R}$ a non-zero constant. Therefore, given eq. (A.5), we have

$$\begin{aligned}
\langle \boldsymbol{h}, \boldsymbol{C} \rangle &= \iint_{\Gamma} h_x(\boldsymbol{r})\,C_x + h_y(\boldsymbol{r})\,C_y + h_z(\boldsymbol{r})\,C_z\,\mathrm{d}\boldsymbol{r} && \text{(A.6)}\\
&= \iint_{\Gamma} h_x(\boldsymbol{r})\,C_x\,\mathrm{d}\boldsymbol{r} && \text{(A.7)}\\
&= 0\,. && \text{(A.8)}
\end{aligned}$$

Since C_x is constant, this results in

$$\iint_{\Gamma} h_x(\boldsymbol{r})\,\mathrm{d}\boldsymbol{r} = 0\,. \tag{A.9}$$

The same result can be obtained with the y and z components. Thus we finally obtain

$$\iint_\Gamma \boldsymbol{h}(\boldsymbol{r})\,\mathrm{d}\boldsymbol{r} = \iint_\Gamma h_x(\boldsymbol{r})\,\hat{\boldsymbol{x}} + h_y(\boldsymbol{r})\,\hat{\boldsymbol{y}} + h_z(\boldsymbol{r})\,\hat{\boldsymbol{z}}\,\mathrm{d}\boldsymbol{r} \tag{A.10}$$

$$= \hat{\boldsymbol{x}} \iint_\Gamma h_x(\boldsymbol{r})\,\mathrm{d}\boldsymbol{r} + \hat{\boldsymbol{y}} \iint_\Gamma h_y(\boldsymbol{r})\,\mathrm{d}\boldsymbol{r} + \hat{\boldsymbol{z}} \iint_\Gamma h_z(\boldsymbol{r})\,\mathrm{d}\boldsymbol{r} \tag{A.11}$$

$$= \boldsymbol{0}\,. \tag{A.12}$$

□

List of Symbols

Abbreviations

BC	Buffa-Christiansen
BEM	Boundary Element Method
CFIE/CFIO	Combined Field Integral Equation/Operator
EFIE/EFIO	Electric Field Integral Equation/Operator
FEM	Finite Element Method
GMRES	Generalized Minimal Residual
MFIE/MFIO	Magnetic Field Integral Equation/Operator
PEC	Perfect Electric Conductor
PMCHWT	Poggio-Miller-Chang-Harrington-Wu-Tsai
RWG	Rao-Wilton-Glisson

Functions

G_k	Green's function
$H_q^{(2)}$	Hankel function of the second kind and order q
J_q	Bessel function of the first kind and order q
Y_q	Bessel function of the second kind and order q

Matrices

$\mathbf{I}$	Identity matrix
$\mathbf{\Lambda}$	Loop to RWG matrix
$\mathbf{\Sigma}$	Star to RWG matrix

$\mathbf{H}$	Global loop to RWG matrix
$\mathbf{P}^{\mathbf{\Lambda H}}$	Loop-Global loop projector
$\mathbf{P}^{\mathbf{\Sigma}}$	Star projector
$\mathbb{P}^{\mathbf{\Lambda}}$	Dual Loop projector
$\mathbb{P}^{\mathbf{\Sigma H}}$	Dual Star-Global loop projector

Notations

a, b	Scalar in $\mathbb{C}$
$\mathbf{a}, \mathbf{b}$	Vector in $\mathbb{C}^m$
$\mathbf{A}, \mathbf{B}$	Matrix in $\mathbb{C}^{m \times n}$
$\mathcal{A}, \mathcal{B}$	Scalar operator
$\boldsymbol{\mathcal{A}}, \boldsymbol{\mathcal{B}}$	Vectorial operator
$(\mathbf{A})_{mn}$	Element (m, n) of $\mathbf{A}$
$\mathbf{A}^{\mathrm{T}}, \mathbf{b}^{\mathrm{T}}$	Transpose of $\mathbf{A}$, $\mathbf{b}$
$\mathbf{A}^{-1}$	Matrix inverse of $\mathbf{A}$
$\mathbf{A}^{+}$	Moore-Penrose pseudo inverse of $\mathbf{A}$
$\Re$, $\Im$	Real, imaginary part
$\|\cdot\|$	Euclidean norm or matrix spectral norm
$\nabla \times \mathbf{A}$	Curl of $\mathbf{A}$
$\nabla \cdot \mathbf{A}$	Divergence of $\mathbf{A}$
$\nabla\Phi$	Gradient of Φ
∇^2, Δ	Laplace operator
Δ_Γ	Laplace-Beltrami operator
$\mathcal{O}$	Big-O Landau symbol

Operators

$\mathcal{H}_k$	Helmholtz operator

$\boldsymbol{\mathcal{K}}_k$	Magnetic operator
$\boldsymbol{\mathcal{T}}_k$	Electric operator
$\boldsymbol{\mathcal{T}}_{\Phi,k}$	Scalar potential operator
$\boldsymbol{\mathcal{T}}_{A,k}$	Vector potential operator

Physical Quantities

$\boldsymbol{E}$	Electric field (V/m)
$\boldsymbol{H}$	Magnetic field (A/m)
$\boldsymbol{D}$	Electric flux density (C/m^2)
$\boldsymbol{B}$	Magnetic flux density (T, Wb/m^2)
$\boldsymbol{j}$	Electric current density (A/m^2)
$\boldsymbol{m}$	Magnetic current density (V/m^2)
$\boldsymbol{j}_s$	Surface electric current density (A/m)
$\boldsymbol{m}_s$	Surface magnetic current density (V/m)
ρ_e	Electric charge density (C/m^3)
ρ_m	Magnetic charge density (Wb/m^3)
ϵ, ϵ_0, ϵ_r	Electric permittivity, of the vacuum (F/m), relative
μ, μ_0, μ_r	Magnetic permeability, of the vacuum (H/m), relative
η	Impedance (Ω)
σ	Conductivity (S/m)
f	Frequency (Hz)
ω	Angular frequency (rad/s)
λ	Wavelength (m)
k	Wave number (m^{-1})
δ	Skin depth (m)
c	Speed of light (m/s)

Other Quantities

$\hat{\boldsymbol{n}}$	Unit normal vector
$\hat{\boldsymbol{t}}$	Unit tangent vector
h	Average mesh element edge length (m)
$\kappa(\mathbf{A})$	Condition number of $\mathbf{A}$
$\sigma(\mathbf{A})$	Singular value of $\mathbf{A}$
$\lambda_q^{\mathcal{A}}$	Eigenvalue of $\mathcal{A}$ with spectral index q

Publications

[26] Tiffany L Chhim, Simon B Adrian, and Francesco P Andriulli. "On the Spectral Behavior and Normalization of a Resonance-Free and High-Frequency Stable Integral Equation". In: *2018 IEEE International Symposium on Antennas and Propagation & USNC/URSI National Radio Science Meeting*. IEEE. 2018, pp. 2447–2448.

[27] Tiffany L Chhim et al. "A Quasi-Helmholtz Projector Stabilized Full Wave Solver Encompassing the Eddy Current Regime". In: *2019 International Conference on Electromagnetics in Advanced Applications (ICEAA)*. IEEE. 2019, pp. 1236–1238.

[28] Tiffany L Chhim et al. "Eddy Current Modeling in Multiply Connected Regions via a Full-Wave Solver Based on the Quasi-Helmholtz Projectors". In: *IEEE Open Journal of Antennas and Propagation* 1 (2020), pp. 534–548.

Bibliography

[1] Francesco P Andriulli. "Loop-Star and Loop-Tree Decompositions: Analysis and Efficient Algorithms". In: *IEEE Transactions on Antennas and Propagation* 60.5 (2012), pp. 2347–2356.

[2] Francesco P Andriulli, Ignace Bogaert, and Kristof Cools. "On the High Frequency Behavior and Stabilization of a Preconditioned and Resonance-Free Formulation". In: *2015 International Conference on Electromagnetics in Advanced Applications (ICEAA)*. IEEE. 2015, pp. 1321–1324.

[3] Francesco P Andriulli, Anita Tabacco, and Giuseppe Vecchi. "Solving the EFIE at Low Frequencies with a Conditioning that Grows Only Logarithmically with the Number of Unknowns". In: *IEEE Transactions on Antennas and Propagation* 58.5 (2010), pp. 1614–1624.

[4] Francesco P Andriulli et al. "A Multiplicative Calderon Preconditioner for the Electric Field Integral Equation". In: *IEEE Transactions on Antennas and Propagation* 56.8 (2008), pp. 2398–2412.

[5] Francesco P Andriulli et al. "On a Well-Conditioned Electric Field Integral Operator for Multiply Connected Geometries". In: *IEEE Transactions on Antennas and Propagation* 61.4 (2013), pp. 2077–2087.

[6] Xavier Antoine and Marion Darbas. "Generalized Combined Field Integral Equations for the Iterative Solution of the Three-Dimensional Helmholtz Equation". In: *ESAIM: Mathematical Modelling and Numerical Analysis* 41.1 (2007), pp. 147–167.

[7] Xavier Antoine, Marion Darbas, and Ya Yan Lu. "An Improved Surface Radiation Condition for High-Frequency Acoustic Scattering Problems". In: *Computer Methods in Applied Mechanics and Engineering* 195.33-36 (2006), pp. 4060–4074.

[8] Ercument Arvas, Roger Harrington, and Joseph Mautz. "Radiation and Scattering from Electrically Small Conducting Bodies of Arbitrary Shape". In: *IEEE Transactions on Antennas and Propagation* 34.1 (1986), pp. 66–77.

[9] Constantine A Balanis. *Advanced Engineering Electromagnetics*. John Wiley & Sons, 2012.

[10] Yang Bao, Zhiwei Liu, and Jiming Song. "Adaptive Cross Approximation Algorithm for Accelerating BEM in Eddy Current Nondestructive Evaluation". In: *Journal of Nondestructive Evaluation* 37.4 (2018), p. 68.

[11] LPS Barra et al. "Iterative Solution of BEM Equations by GMRES Algorithm". In: *Computers & Structures* 44.6 (1992), pp. 1249–1253.

[12] Mario Bebendorf. "Approximation of Boundary Element Matrices". In: *Numerische Mathematik* 86.4 (2000), pp. 565–589.

[13] Yves Beghein et al. "On a Low-Frequency and Refinement Stable PMCHWT Integral Equation Leveraging the Quasi-Helmholtz Projectors". In: *IEEE Transactions on Antennas and Propagation* 65.10 (2017), pp. 5365–5375.

[14] CP Bidinosti, EM Chapple, and ME Hayden. "The Sphere in a Uniform RF Field—Revisited". In: *Concepts in Magnetic Resonance Part B: Magnetic Resonance Engineering: An Educational Journal* 31.3 (2007), pp. 191–202.

[15] Ignace Bogaert et al. "Low Frequency Scaling of the Mixed MFIE for Scatterers with a Non-Simply Connected Surface". In: *2011 International Conference on Electromagnetics in Advanced Applications (ICEAA)*. IEEE. 2011, pp. 951–954.

[16] Marc Bonnet and Edouard Demaldent. "The Eddy Current Model as a Low-Frequency, High-Conductivity Asymptotic Form of the Maxwell Transmission Problem". In: *Computers & Mathematics with Applications* (2018).

[17] Yassine Boubendir and Catalin Turc. "Well-Conditioned Boundary Integral Equation Formulations for the Solution of High-Frequency Electromagnetic Scattering Problems". In: *Computers & Mathematics with Applications* 67.10 (2014), pp. 1772–1805.

[18] Nicola Bowler and JR Bowler. *Eddy-Current Nondestructive Evaluation*. Springer, 2019.

[19] Annalisa Buffa, Habib Ammari, and Jean-Claude Nédélec. "A Justification of Eddy Currents Model for the Maxwell Equations". In: *SIAM Journal on Applied Mathematics* 60.5 (2000), pp. 1805–1823.

[20] Annalisa Buffa and Snorre Christiansen. "A Dual Finite Element Complex on the Barycentric Refinement". In: *Mathematics of Computation* 76.260 (2007), pp. 1743–1769.

[21] M Burton and S Kashyap. "A Study of a Recent, Moment-Method Algorithm that is Accurate to Very Low Frequencies". In: *Applied Computational Electromagnetics Society Journal* 10 (1995), pp. 58–68.

[22] Yu Chang and Roger F Harrington. "A Surface Formulation for Characteristic Modes of Material Bodies". In: *IEEE Transactions on Antennas and Propagation* 25.6 (1977), pp. 789–795.

[23] Siyuan Y Chen et al. "Analysis of Low Frequency Scattering from Penetrable Scatterers". In: *IEEE Transactions on Geoscience and Remote Sensing* 39.4 (2001), pp. 726–735.

[24] Weng Cho Chew, Mei Song Tong, and Bin Hu. "Integral Equation Methods for Electromagnetic and Elastic Waves". In: *Synthesis Lectures on Computational Electromagnetics* 3.1 (2008), pp. 1–241.

[25] Weng Cho Chew et al. *Fast and Efficient Algorithms in Computational Electromagnetics*. Artech House, Inc., 2001.

[26] Tiffany L Chhim, Simon B Adrian, and Francesco P Andriulli. "On the Spectral Behavior and Normalization of a Resonance-Free and High-Frequency Stable Integral Equation". In: *2018 IEEE International Symposium on Antennas and Propagation & USNC/URSI National Radio Science Meeting*. IEEE. 2018, pp. 2447–2448.

[27] Tiffany L Chhim et al. "A Quasi-Helmholtz Projector Stabilized Full Wave Solver Encompassing the Eddy Current Regime". In: *2019 International Conference on Electromagnetics in Advanced Applications (ICEAA)*. IEEE. 2019, pp. 1236–1238.

[28] Tiffany L Chhim et al. "Eddy Current Modeling in Multiply Connected Regions via a Full-Wave Solver Based on the Quasi-Helmholtz Projectors". In: *IEEE Open Journal of Antennas and Propagation* 1 (2020), pp. 534–548.

[29] Snorre H Christiansen and Jean-Claude Nédélec. "A Preconditioner for the Electric Field Integral Equation Based on Calderon Formulas". In: *SIAM Journal on Numerical Analysis* 40.3 (2002), pp. 1100–1135.

[30] Ronald Coifman, Vladimir Rokhlin, and Stephen Wandzura. "The Fast Multipole Method for the Wave Equation: A Pedestrian Prescription". In: *IEEE Antennas and Propagation Magazine* 35.3 (1993), pp. 7–12.

[31] Harry Contopanagos et al. "Well-Conditioned Boundary Integral Equations for Three-Dimensional Electromagnetic Scattering". In: *IEEE Transactions on Antennas and Propagation* 50.12 (2002), pp. 1824–1830.

[32] Kristof Cools et al. "Nullspaces of MFIE and Calderón Preconditioned EFIE Operators Applied to Toroidal Surfaces". In: *IEEE Transactions on Antennas and Propagation* 57.10 (2009), pp. 3205–3215.

[33] Tie Jun Cui and Weng Cho Chew. "Accurate Model of Arbitrary Wire Antennas in Free Space, Above or Inside Ground". In: *IEEE Transactions on Antennas and Propagation* 48.4 (2000), pp. 482–493.

[34] Marion Darbas. "Generalized Combined Field Integral Equations for the Iterative Solution of the Three-Dimensional Maxwell Equations". In: *Applied Mathematics Letters* 19.8 (2006), pp. 834–839.

[35] Marion Darbas. “Préconditionneurs Analytiques de type Calderòn pour les Formulations Intégrales des Problèmes de Diffraction d’Ondes”. PhD thesis. Toulouse, INSA, 2004.

[36] Heinz K Dirks. “Quasi-Stationary Fields for Microelectronic Applications”. In: *Electrical Engineering (Archiv fur Elektrotechnik)* 79.2 (1996), pp. 145–155.

[37] Paweł Dłotko et al. “Fake Conductivity or Cohomology: Which to Use When Solving Eddy Current Problems with h-Formulations?” In: *IEEE Transactions on Magnetics* 55.6 (2019), pp. 1–4.

[38] Michael G Duffy. “Quadrature over a Pyramid or Cube of Integrands with a Singularity at a Vertex”. In: *SIAM Journal on Numerical Analysis* 19.6 (1982), pp. 1260–1262.

[39] Thomas F Eibert. “Iterative-Solver Convergence for Loop-Star and Loop-Tree Decompositions in Method-of-Moments Solutions of the Electric-Field Integral Equation”. In: *IEEE Antennas and Propagation Magazine* 46.3 (2004), pp. 80–85.

[40] Thomas F Eibert and Volkert Hansen. “On the Calculation of Potential Integrals for Linear Source Distributions on Triangular Domains”. In: *IEEE Transactions on Antennas and Propagation* 43.12 (1995), pp. 1499–1502.

[41] Javier García-Martín, Jaime Gómez-Gil, and Ernesto Vázquez-Sánchez. “Non-Destructive Techniques Based on Eddy Current Testing”. In: *Sensors* 11.3 (2011), pp. 2525–2565.

[42] Semyon Aranovich Gershgorin. “Über die Abgrenzung der Eigenwerte einer Matrix”. In: *Bulletin de l’Académie des Sciences de l’URSS. Classe des Sciences Mathématiques et na* 6 (1931), pp. 749–754.

[43] Walton C Gibson. *The Method of Moments in Electromagnetics*. CRC Press, 2014.

[44] Roberto D Graglia. “On the Numerical Integration of the Linear Shape Functions Times the 3-D Green’s Function or its Gradient on a Plane Triangle”. In: *IEEE Transactions on Antennas and Propagation* 41.10 (1993), pp. 1448–1455.

[45] Roberto D Graglia and Guido Lombardi. “Machine Precision Evaluation of Singular and Nearly Singular Potential Integrals by Use of Gauss Quadrature Formulas for Rational Functions”. In: *IEEE Transactions on Antennas and Propagation* 56.4 (2008), pp. 981–998.

[46] Leslie Greengard and Vladimir Rokhlin. “A Fast Algorithm for Particle Simulations”. In: *Journal of Computational Physics* 73.2 (1987), pp. 325–348.

[47] Wolfgang Hackbusch. *Iterative Solution of Large Sparse Systems of Equations*. Vol. 95. Springer, 1994.

[48] Roger F Harrington. *Field Computation by Moment Methods*. Wiley-IEEE Press, 1993.

[49] Harold V Henderson and Shayle R Searle. "On Deriving the Inverse of a Sum of Matrices". In: *Siam Review* 23.1 (1981), pp. 53–60.

[50] Magnus R Hestenes and Eduard Stiefel. "Methods of Conjugate Gradients for Solving Linear Systems". In: *Journal of Research of the National Bureau of Standards* 49.6 (1952), pp. 409–436.

[51] Ralf Hiptmair. "Boundary Element Methods for Eddy Current Computation". In: *Boundary Element Analysis*. Springer, 2007, pp. 213–248.

[52] George C Hsiao and Ralph E Kleinman. "Error Analysis in Numerical Solution of Acoustic Integral Equations". In: *International Journal for Numerical Methods in Engineering* 37.17 (1994), pp. 2921–2933.

[53] Seppo Järvenpää, Matti Taskinen, and Pasi Ylä-Oijala. "Singularity Extraction Technique for Integral Equation Methods with Higher Order Basis Functions on Plane Triangles and Tetrahedra". In: *International Journal for Numerical Methods in Engineering* 58.8 (2003), pp. 1149–1165.

[54] Jian-Ming Jin. *Theory and Computation of Electromagnetic Fields*. John Wiley & Sons, 2015.

[55] Joseph B Keller. "Geometrical Theory of Diffraction". In: *Josa* 52.2 (1962), pp. 116–130.

[56] EE Kriezis et al. "Eddy Currents: Theory and Applications". In: *Proceedings of the IEEE* 80.10 (1992), pp. 1559–1589.

[57] Francis Lazarus et al. "Computing a Canonical Polygonal Schema of an Orientable Triangulated Surface". In: *Proceedings of the Seventeenth Annual Symposium on Computational Geometry*. 2001, pp. 80–89.

[58] Jin-Fa Lee, Robert Lee, and Robert J Burkholder. "Loop Star Basis Functions and a Robust Preconditioner for EFIE Scattering Problems". In: *IEEE Transactions on Antennas and Propagation* 51.8 (2003), pp. 1855–1863.

[59] Oren E Livne and Achi Brandt. "Lean Algebraic Multigrid (LAMG): Fast Graph Laplacian Linear Solver". In: *SIAM Journal on Scientific Computing* 34.4 (2012), B499–B522.

[60] Cai-Cheng Lu and Weng Cho Chew. "A Multilevel Algorithm for Solving a Boundary Integral Equation of Wave Scattering". In: *Microwave and Optical Technology Letters* 7.10 (1994), pp. 466–470.

[61] Joseph R Mautz and Roger F Harrington. *H-Field, E-Field, and Combined Field Solutions for Bodies of Revolution*. Tech. rep. Syracuse University, New York, Department of Electrical and Computer Engineering, 1977.

[62] Adrien Merlini et al. "Magnetic and Combined Field Integral Equations Based on the Quasi-Helmholtz Projectors". In: *IEEE Transactions on Antennas and Propagation* (2020).

[63] Eric Michielssen and Amir Boag. "A Multilevel Matrix Decomposition Algorithm for Analyzing Scattering from Large Structures". In: *IEEE Transactions on Antennas and Propagation* 44.8 (1996), pp. 1086–1093.

[64] James R Nagel. "Induced Eddy Currents in Simple Conductive Geometries: Mathematical Formalism Describes the Excitation of Electrical Eddy Currents in a Time-Varying Magnetic Field". In: *IEEE Antennas and Propagation Magazine* 60.1 (2017), pp. 81–88.

[65] Artem Napov and Yvan Notay. "An Algebraic Multigrid Method with Guaranteed Convergence Rate". In: *SIAM Journal on Scientific Computing* 34.2 (2012), A1079–A1109.

[66] Jean-Claude Nédélec. *Acoustic and Electromagnetic Equations: Integral Representations for Harmonic Problems*. Springer Science & Business Media, 2001.

[67] Frank WJ Olver et al. *NIST Handbook of Mathematical Functions Hardback and CD-ROM*. Cambridge University Press, 2010.

[68] John Erick Ortiz Guzman et al. "On the Hierarchical Preconditioning of the PMCHWT Integral Equation on Simply and Multiply Connected Geometries". In: *IEEE Antennas and Wireless Propagation Letters* 16 (2016), pp. 1044–1047.

[69] Prabhakar H Pathak. "Techniques for High-Frequency Problems". In: *Antenna Handbook*. Springer, 1988, pp. 195–311.

[70] Joris Peeters, Ignace Bogaert, and Daniël De Zutter. "Calculation of MoM Interaction Integrals in Highly Conductive Media". In: *IEEE Transactions on Antennas and Propagation* 60.2 (2011), pp. 930–940.

[71] Andrew J Poggio and Edmund K Miller. *Integral Equation Solutions of Three-Dimensional Scattering Problems*. MB Assoc., 1970.

[72] Zhi Guo Qian and Weng Cho Chew. "A Quantitative Study on the Low Frequency Breakdown of EFIE". In: *Microwave and Optical Technology Letters* 50.5 (2008), pp. 1159–1162.

[73] Zhi Guo Qian and Weng Cho Chew. "Enhanced A-EFIE with Perturbation Method". In: *IEEE Transactions on Antennas and Propagation* 58.10 (2010), pp. 3256–3264.

[74] Zhi Guo Qian, Weng Cho Chew, and Roberto Suaya. "Generalized Impedance Boundary Condition for Conductor Modeling in Surface Integral Equation". In: *IEEE Transactions on Microwave Theory and Techniques* 55.11 (2007), pp. 2354–2364.

[75] Sadasiva M Rao, Donald R Wilton, and Allen W Glisson. "Electromagnetic Scattering by Surfaces of Arbitrary Shape". In: *IEEE Transactions on Antennas and Propagation* 30.3 (1982), pp. 409–418.

[76] Z Ren. "T-/spl omega/Formulation for Eddy-Current Problems in Multiply Connected Regions". In: *IEEE Transactions on Magnetics* 38.2 (2002), pp. 557–560.

[77] Juan M Rius et al. "Multilevel Matrix Decomposition Algorithm for Analysis of Electrically Large Electromagnetic Problems in 3-D". In: *Microwave and Optical Technology Letters* 22.3 (1999), pp. 177–182.

[78] Wolfgang M Rucker, Robert Hoschek, and Kurt R Richter. "Various BEM Formulations for Calculating Eddy Currents in Terms of Field Variables". In: *IEEE Transactions on Magnetics* 31.3 (1995), pp. 1336–1341.

[79] Youcef Saad and Martin H Schultz. "GMRES: A Generalized Minimal Residual Algorithm for Solving Nonsymmetric Linear Systems". In: *SIAM Journal on Scientific and Statistical Computing* 7.3 (1986), pp. 856–869.

[80] Jonathan Richard Shewchuk. *An Introduction to the Conjugate Gradient Method Without the Agonizing Pain*. 1994.

[81] Jiming Song, Cai-Cheng Lu, and Weng Cho Chew. "Multilevel Fast Multipole Algorithm for Electromagnetic Scattering by Large Complex Objects". In: *IEEE Transactions on Antennas and Propagation* 45.10 (1997), pp. 1488–1493.

[82] Jiming M Song and Weng Cho Chew. "Multilevel Fast-Multipole Algorithm for Solving Combined Field Integral Equations of Electromagnetic Scattering". In: *Microwave and Optical Technology Letters* 10.1 (1995), pp. 14–19.

[83] Peter Sonneveld. "CGS, a Fast Lanczos-Type Solver for Nonsymmetric Linear Systems". In: *SIAM Journal on Scientific and Statistical Computing* 10.1 (1989), pp. 36–52.

[84] Olaf Steinbach. *Numerical Approximation Methods for Elliptic Boundary Value Problems: Finite and Boundary Elements*. Springer Science & Business Media, 2007.

[85] Leonard L Tsai. "A Numerical Solution for the Near and Far Fields of an Annular Ring of Magnetic Current". In: *IEEE Transactions on Antennas and Propagation* 20.5 (1972), pp. 569–576.

[86] Andreas Tzoulis and Thomas F Eibert. "Review of Singular Potential Integrals for Method of Moments Solutions of Surface Integral Equations". In: *Advances in Radio Science* 2.B. 2 (2005), pp. 93–99.

[87] Giuseppe Vecchi. "Loop-Star Decomposition of Basis Functions in the Discretization of the EFIE". In: *IEEE Transactions on Antennas and Propagation* 47.2 (1999), pp. 339–346.

[88] Audrey Vigneron, Édouard Demaldent, and Marc Bonnet. "Surface Integral Equations for Electromagnetic Testing: the Low-Frequency and High-Contrast Case". In: *IEEE Transactions on Magnetics* 50.2 (2014), pp. 117–120.

[89] Francesca Vipiana and Donald R Wilton. "Numerical Evaluation via Singularity Cancellation Schemes of Near-Singular Integrals Involving the Gradient of Helmholtz-Type Potentials". In: *IEEE Transactions on Antennas and Propagation* 61.3 (2012), pp. 1255–1265.

[90] Karl F Warnick. *Numerical Analysis for Electromagnetic Integral Equations*. Artech House, 2008.

[91] Karl F Warnick and Weng Cho Chew. "On the Spectrum of the Electric Field Integral Equation and the Convergence of the Moment Method". In: *International Journal for Numerical Methods in Engineering* 51.1 (2001), pp. 31–56.

[92] Donald R Wilton and Allen W Glisson. "On Improving the Stability of the Electric Field Integral Equation at Low Frequencies". In: *1981 USNC/URSI Spring Meeting Digest*. Los Angeles, California, June 1981, p. 24.

[93] Donald R Wilton et al. "Evaluation of Static Potential Integrals on Triangular Domains". In: *IEEE Access* (2020).

[94] Te-Kao Wu and Leonard L Tsai. "Scattering from Arbitrarily-Shaped Lossy Dielectric Bodies of Revolution". In: *Radio Science* 12.5 (1977), pp. 709–718.

[95] Tian Xia et al. "An Integral Equation Modeling of Lossy Conductors with the Enhanced Augmented Electric Field Integral Equation". In: *IEEE Transactions on Antennas and Propagation* 65.8 (2017), pp. 4181–4190.

[96] Su Yan, Jian-Ming Jin, and Zaiping Nie. "EFIE Analysis of Low-Frequency Problems with Loop-Star Decomposition and Calderón Multiplicative Preconditioner". In: *IEEE Transactions on Antennas and Propagation* 58.3 (2009), pp. 857–867.

[97] Yunhua Zhang et al. "Magnetic Field Integral Equation at Very Low Frequencies". In: *IEEE Transactions on Antennas and Propagation* 51.8 (2003), pp. 1864–1871.

[98] Jun-Sheng Zhao and Weng Cho Chew. "Integral Equation Solution of Maxwell's Equations from Zero Frequency to Microwave Frequencies". In: *IEEE Transactions on Antennas and Propagation* 48.10 (2000), pp. 1635–1645.

[99] Jun-Sheng Zhao et al. "Cancellations of Surface Loop Basis Functions". In: *IEEE Antennas and Propagation Society International Symposium (IEEE Cat. No. 02CH37313)*. Vol. 1. IEEE. 2002, pp. 58–61.

[100] Kezhong Zhao, Marinos N Vouvakis, and Jin-Fa Lee. "The Adaptive Cross Approximation Algorithm for Accelerated Method of Moments Computations of EMC Problems". In: *IEEE Transactions on Electromagnetic Compatibility* 47.4 (2005), pp. 763–773.

[101] Dalian Zheng. "Three-Dimensional Eddy Current Analysis by the Boundary Element Method". In: *IEEE Transactions on Magnetics* 33.2 (1997), pp. 1354–1357.

[102] Jianfang Zhu and Dan Jiao. "A Rigorous Solution to the Low-Frequency Breakdown in Full-Wave Finite-Element-Based Analysis of General Problems Involving Inhomogeneous Lossless/Lossy Dielectrics and Nonideal Conductors". In: *IEEE Transactions on Microwave Theory and Techniques* 59.12 (2011), pp. 3294–3306.